Chapter 5: Synthesis and tribological behaviour of vacuum hot press sintered Ni_3Al-Ag-Cu-*h*BN and Ni_3Al-WS_2-Cu-*h*BN composites at elevated temperatures

This chapter starts with the results on the characterisation of Cu-*h*BN hybrid material, ball-milled powders, and microstructure and properties (physical and mechanical) evaluation of Ni_3Al-based composites containing different combination of solid lubricants, i.e., (a) Ni_3Al-10wt.% Ag, Ni_3Al-10wt.% Cu-*h*BN, Ni_3Al-5wt.% Ag-5wt.% Cu-*h*BN composites, and (b) Ni_3Al-10wt.% WS_2, Ni_3Al-10wt.% Cu-*h*BN, Ni_3Al-5wt.% WS_2-5wt.% Cu-*h*BN synthesised via vacuum hot press sintering. This is followed by the presentation of results on the friction and wear behaviour of the above composites conducted at RT, 200 °C, 400 °C, 600 °C, and 800 °C under a constant applied load of 10 N, sliding speed of 0.2 m/s and sliding duration of 360 m against a stationary silicon nitride ball (Si_3N_4, Dia.: 6 mm) and characterization of worn surface of composites as well as the counterpart ball. The results have been discussed based on the features seen on the worn surfaces of Ni_3Al-based composites and the counterface Si_3N_4 slid to develop an understanding of the tribological performance of composites. A comparative assessment of the friction and wear behaviour of Ni_3Al, Ni_3Al-10wt.% Ag, Ni_3Al-10wt.% WS_2, Ni_3Al-10wt.% Cu-*h*BN, Ni_3Al-5wt.% Ag-5wt.% Cu-*h*BN and Ni_3Al-5wt.% WS_2-5wt.% Cu-*h*BN composites are also presented at the end of the chapter.

5.1 Results and discussions: Synthesis and Tribological behaviour Ni_3Al-Ag/Ni_3Al-Cu-*h*BN/Ni_3Al-Ag-Cu-*h*BN composites

5.1.1 Characterization of *h*-BNNSs and Cu-*h*BN powders

The morphological features of *h*-BNNSs were examined by microscopic images. As depicted in Figs. 5.1(a and b), the lateral dimension of *h*-BNNSs ranged from 40 to 250

nm. A high-resolution TEM image (Fig. 5.1c) clearly illustrates the lamellar structure of *h*-BNNSs. The spherical to ellipsoidal darker features made of copper oxide are evenly distributed (Figs. 5.1 d-f) on the surface of *h*-BNNSs. The ultrasound-assisted exfoliation introduced several structural defects and oxide sites on the surface of *h*-BNNSs, which are believed to function as anchoring sites for the growth of copper oxide during chemical processing. The size of copper oxide nanoparticles in Cu-*h*BN varies from 3 to 15 *nm*. Moreover, the uniform distribution of Cu along with B and N, as shown in Fig. 5.1, explicitly revealed the uniform distribution of copper oxide nanoparticles on the surface of *h*-BNNSs.

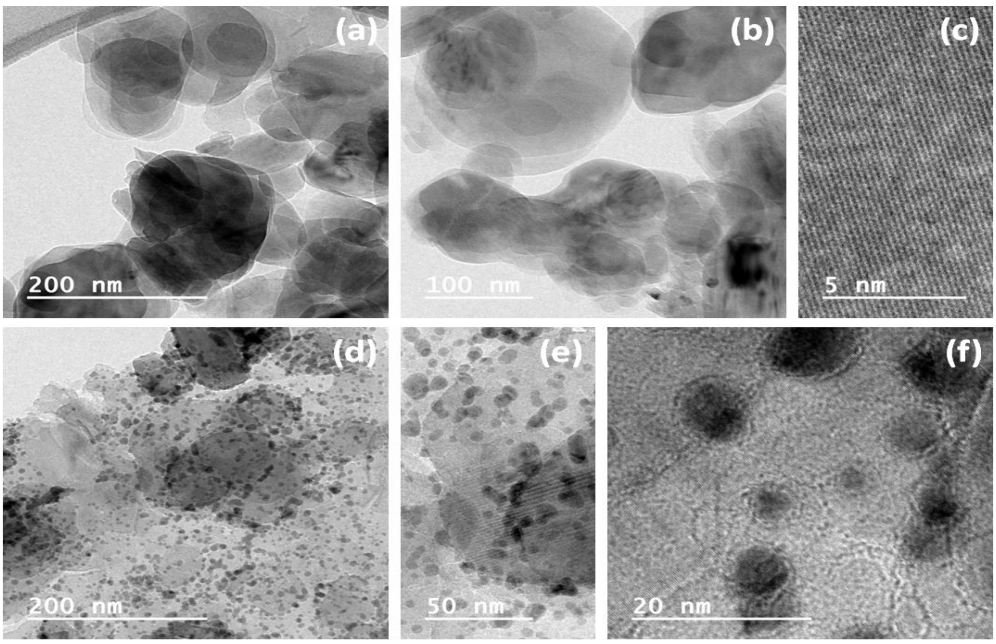

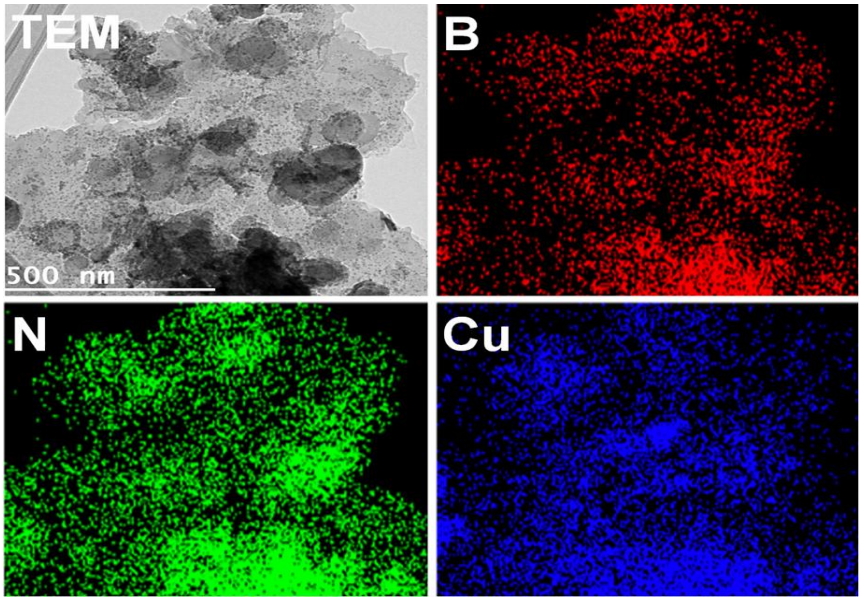

Fig. 5.1: TEM images of (a-c) *h*-BNNSs and (d-f) Cu-*h*BN at different magnifications along with corresponding area elemental (Boron, Nitrogen, and Copper) distribution.

The crystalline phases of constituent materials in Cu-*h*BN are probed by gathering their XRD patterns. The diffraction peaks in the XRD pattern of Cu-*h*BN (Fig. 5.2) at 2θ of 26.7°, 41.7°, 44.1°, 50.1°, 55.1° and 75.9° corresponding to (002), (100), (101), (102), (004), and (110) planes, respectively as per JCPDS card No. 34-0421, revealed the hexagonal crystalline structure of *h*BN in Cu-*h*BN [140]. A *d*-spacing between thick atomic lamellae of *h*BN is estimated as 0.33 *nm*, corresponding to the (002) plane at 2θ of 26.7°. The Van der Waals interaction holds *h*BN atomic lamellae together along the basal plane and provides low resistance to shear, making it a potential material for tribological applications. The emergence of diffraction peaks corresponding to (100), (111), (020), (-113) and (220) planes in the XRD pattern of Cu-*h*BN revealed the monoclinic structure of CuO (JCPDS card No. 5-661). The diffraction peaks for the face-centric cubic structure of Cu_2O attributed to (110) and (111) crystalline planes (JCPDS card No. 5-667) revealed the preparation of Cu_2O nanoparticles as well in Cu-*h*BN. Moreover, the diffraction peak at 2θ

of 16.5° corresponding to (020) crystalline plane also confirmed the presence of Cu $(OH)_2$ in Cu-*h*BN [141].

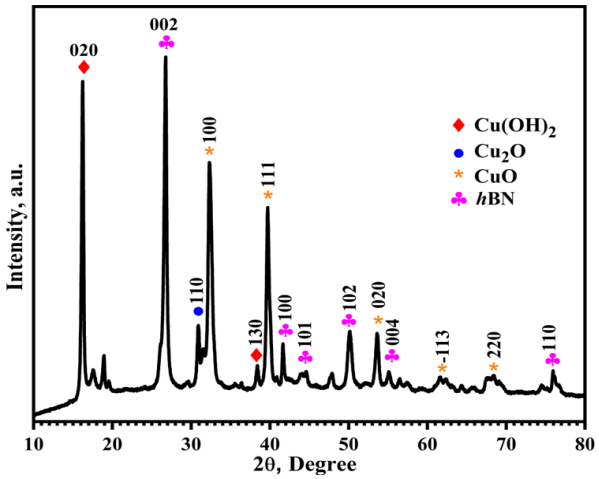

Fig. 5.2: XRD pattern of Cu-*h*BN along with assignment of diffraction features.

The chemical features on the surface of Cu-*h*BN were probed by XPS analysis. The spectral peaks observed in the XPS survey spectrum of Cu-*h*BN attributed to Cu 2p, O 1s, N 1s, C 1s, and B 1s (Fig. 5.3) revealed Cu, O, N, C and B as constituent elements. The structural skeleton of *h*BN in Cu-*h*BN is composed of B and N, whereas Cu and O primarily contributed to CuO/Cu_2O nanoparticles thoroughly grafted on the surface of *h*BN. The adventitious carbon accumulated during the preparation of Cu-*h*BN and environmental exposure contributed to the C in Cu-*h*-BN. Moreover, deconvoluted peaks of C 1s (inset of Fig. 5.3) at 284.6, 285.9, and 288.2 eV ascribed to C-C/C-H, C-O and COO-based linkages confirmed the presence of adventitious carbon. XPS is a highly sensitive surface analysis technique that reveals the oxidation state of Cu in its oxides and probes the chemical composition of Cu-*h*BN. As shown in the inset of Fig. 5.3, the Cu 2p peak is made of two doublets beside two shake-up satellite peaks, revealing binary oxides. The deconvoluted peaks at lower binding energies, i.e., 932.6 and 952.5 eV, representing Cu $2p_{3/2}$ and Cu $2p_{1/2}$, respectively, revealed the Cu^+-based Cu_2O. Furthermore, two comparatively intense peaks at higher binding energies of 935.0 and 954.8 eV are assigned to Cu $2p_{3/2}$ and Cu

$2p_{1/2}$ of Cu^{2+}-based CuO [142]. XPS-based surface analysis revealed CuO as the major oxide, constituting 57%. Moreover, the presence of two shake-up satellite peaks at 944.1 and 962.6 eV suggests the presence of an unfilled Cu 3d9 shell, confirming the Cu^{2+} phase in the form of CuO [143].

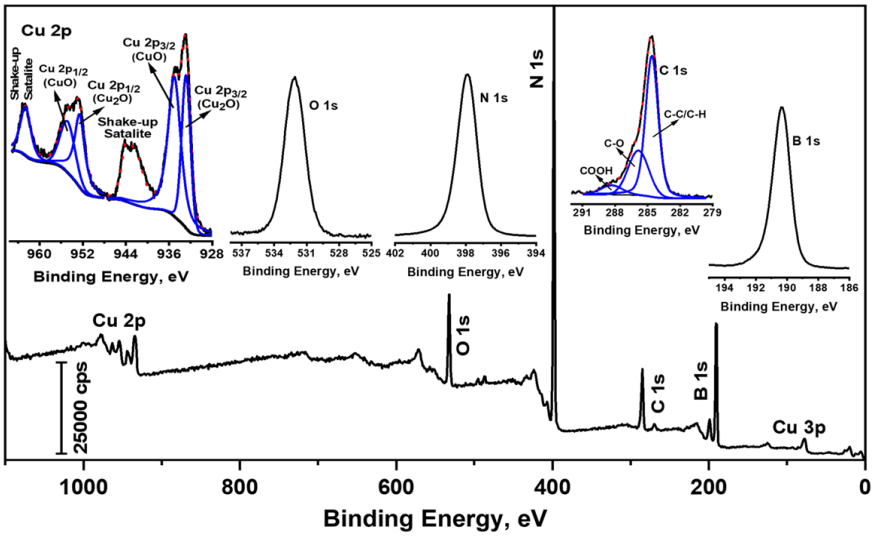

Fig. 5.3: Wide scan spectrum of Cu-*h*BN along with high-resolution B 1s, C 1s, N 1s, O 1s, and Cu 2p XPS spectra. The high-resolution Cu 2p spectrum is deconvoluted to reveal different oxidation states of Cu in their oxides.

5.1.2 Characterisation of ball-milled powders and composites

Table 5.1 presents the designation of powders along with their composition, density and hardness. Figure 5.4 presents the FESEM micrographs and corresponding elemental maps of ball-milled powders which confirmed the presence of respective constituent elements in each powder. XRD patterns of ball-milled powders as well as Ni_3Al and composites are illustrated in Fig. 5.5. The formation of Ni_3Al intermetallic compound has been confirmed by the XRD patterns of the milled powders shown in Fig. 5.5(a). XRD patterns further revealed the presence of Ag (ICSD Ref. No. 01-087-0597), CuO (ICSD Ref. No. 01-089-5898), *h*BN (ICSD Ref. No. 01-085-1068), Mo (ICSD Ref. No. 01-089-5156) and Ni_3Al (ICSD Ref. No. 03-065-430). The diffraction patterns of sintered NI and composites (NI-

10Ag, NI-10BN and NI-10AgBN) depicted in Fig. 5.5(b) revealed the presence of intense peaks corresponding to Ni_3Al apart from those pertaining to Mo, CuO, Ag and *h*BN, confirming that no oxidation or disintegration occurred during the vacuum hot press sintering process.

Table 5.1: Sample designation, composition, density (real and relative), and microhardness.

Sample designation	Composition	Actual Density (g/cm^3)	Relative Density (%)	Microhardness ($HV_{0.2}$)
NI	100 wt.% Ni_3Al	8.372	99.46	355 ± 5
NI-10Ag	90 wt.% Ni_3Al-10wt.% Ag	8.328	96.67	313 ± 6
NI-10BN	90 wt.% Ni_3Al-10wt.% Cu-*h*BN	6.990	89.89	335 ± 5
NI-10AgBN	90 wt.% Ni_3Al-5wt.% Ag- 5wt.% Cu-*h*BN	7.734	94.31	325 ± 7

The FESEM micrographs illustrated in Fig. 5.6 show the microstructure and elemental mapping of the Ni_3Al (NI) and the composites NI-10Ag, NI-10BN, and NI-10AgBN. Figure 5.6(a) shows the microstructure of Ni_3Al, the formation of which has been confirmed by the XRD analysis given in Figs. 5.5(a and b). The microstructure of composite specimens, as shown in Figs. 5.6(b to d) revealed a compact microstructure with a homogeneous dispersion of constituent materials (marked by arrows) such as Ag in NI-10Ag (Fig. 5.6b), Cu-*h*BN in NI-10BN (Fig. 5.6c), and both Ag and Cu-*h*BN in NI-10AgBN (Fig. 5.6d). The presence of constituents has been confirmed by the elemental mapping of NI-10Ag, NI-10BN, and NI-10AgBN, as depicted in Fig. 5.6. The addition of Ag and Cu-*h*BN resulted in a decrease in the hardness of Ni_3Al from 355 ± 5 HV to 313 ± 6 HV and 335 ± 5 HV, respectively. However, the addition of both Ag and Cu-*h*BN to Ni_3Al led to a hardness value of 325 ±7 HV. A reduction in the hardness may be ascribed to the soft nature of Ag and *h*BN.

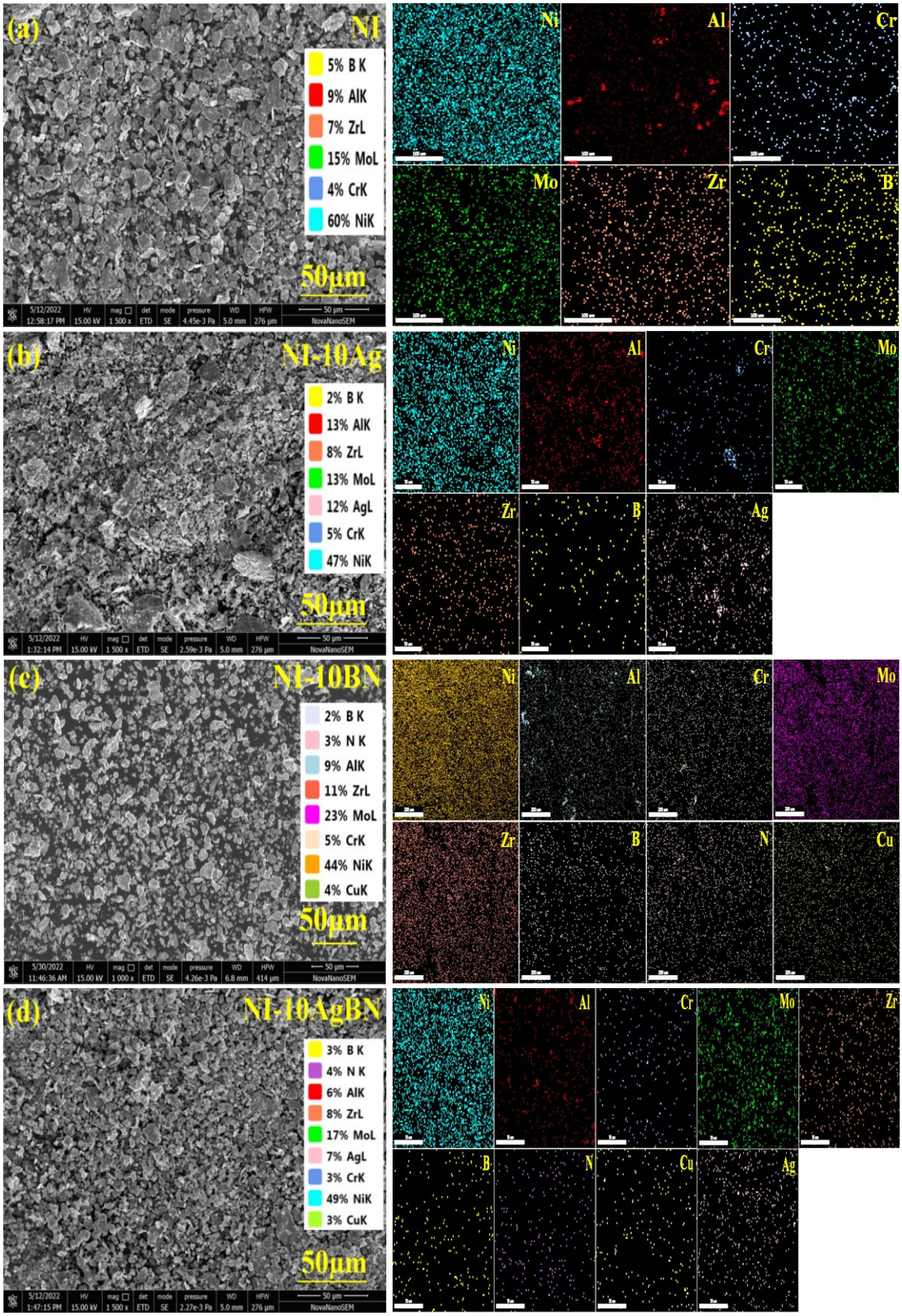

Fig. 5.4: FESEM images and corresponding elemental maps of ball-milled powders: (a) NI, (b) NI-10Ag, (c) NI-10BN, and (d) NI-10AgBN.

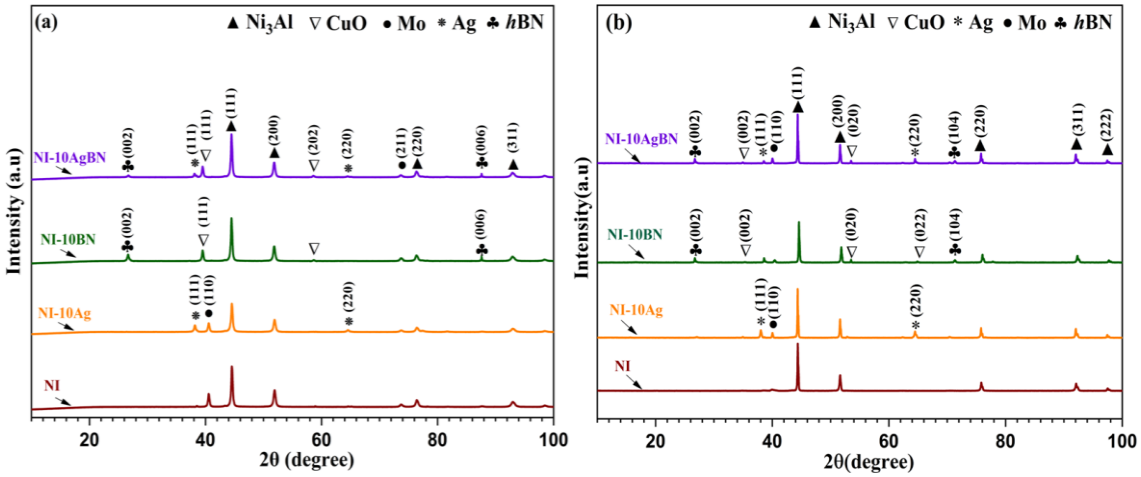

Fig. 5.5: XRD patterns of (a) ball-milled powders and (b) vacuum hot press sintered composite.

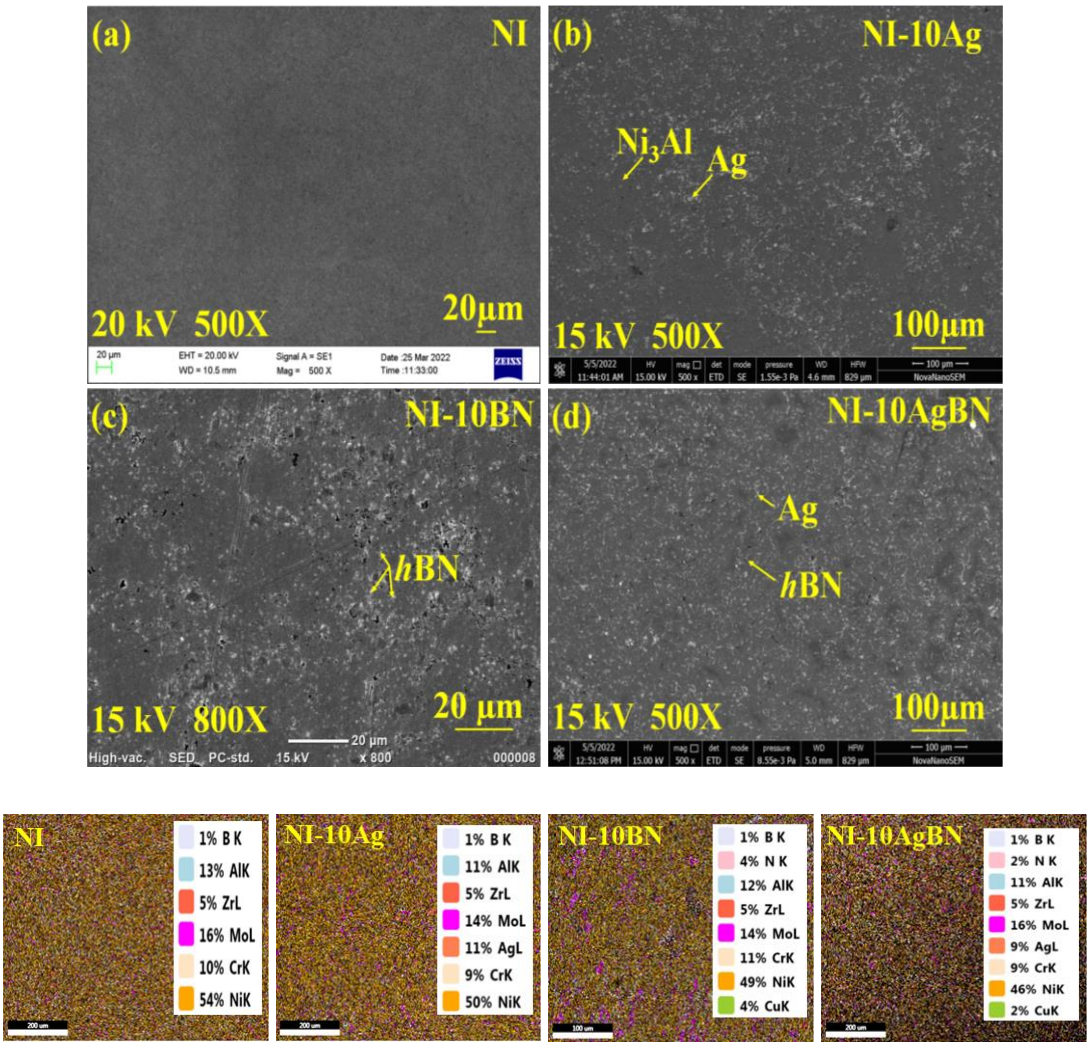

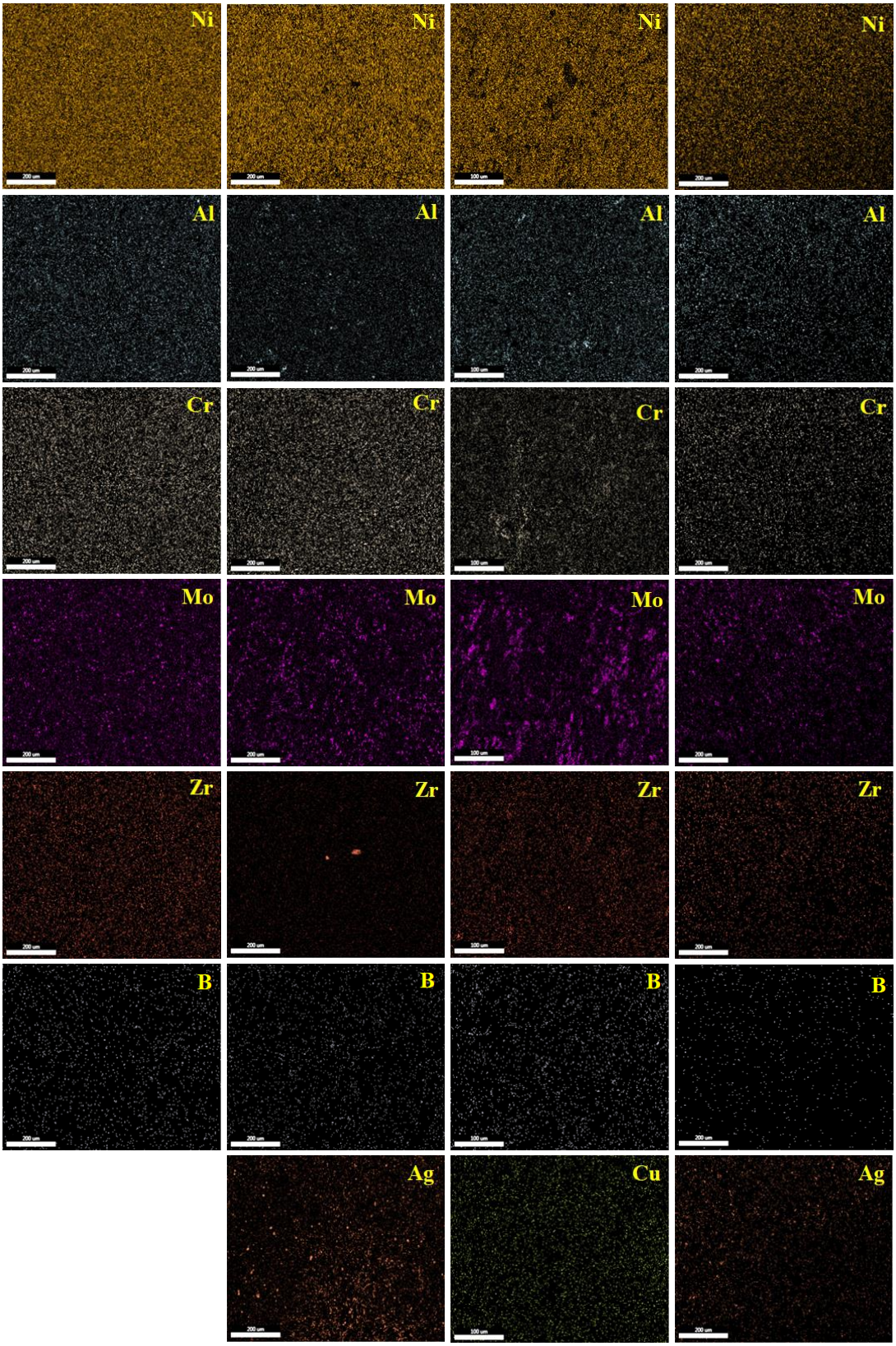
Ni
Ni
Ni
Ni
Al
Al
Al
Al
Cr
Cr
Cr
Cr
Mo
Mo
Mo
Mo
Zr
Zr
Zr
Zr
B
B
B
B
Ag
Cu
Ag

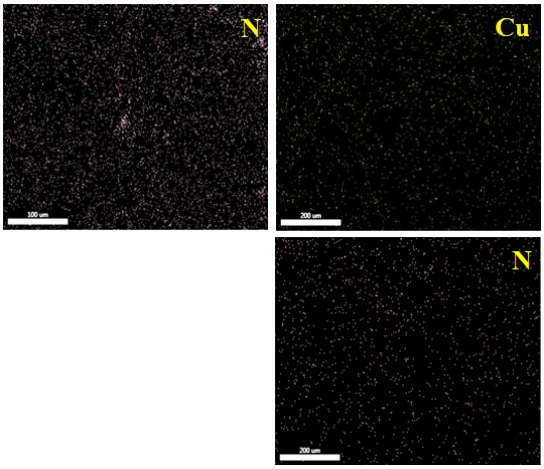

Fig. 5.6: FESEM micrographs showing the microstructure of (a) NI, (b) NI-10Ag, (c) NI-10BN and (d) NI-10AgBN and corresponding EDS elemental mapping.

5.1.3 Tribological behaviour Ni_3Al-Ag/ Ni_3Al-Cu-*h*BN/ Ni_3Al-Ag-Cu-*h*BN composites

5.1.3.1 Dry sliding friction

5.1.3.1.1 Variation of coefficient of friction with time

Figures 5.7(a-e) shows the friction profiles over time for NI, NI-10Ag, NI-10BN, and NI-10AgBN composite specimens under fixed sliding speed (0.2 m/s) and constant normal load (10 N) at different temperatures (RT, 200 °C, 400 °C, 600 °C and 800 °C). The NI has a consistently higher coefficient of friction than the others at all test temperatures. At RT (Fig. 5.7a), the coefficient of friction (CoF) for NI stabilises after 400 s and maintains a constant value throughout the entire duration of the test with marginal fluctuations in the amplitude, while the CoF for the composites stabilises after 900 s (NI-10Ag), 800 s (NI-10BN), and 1000 s (NI-10AgBN), respectively, with minor fluctuations. At 200 °C (Fig. 5.7b), the CoF of NI, NI-10Ag, NI-10BN and NI-10AgBN stabilises after 1400 s, 1000 s, 1200 s and 900 s, respectively. At 400 °C (Fig. 5.7c), the CoF for NI-10AgBN appears to be stable right from the beginning to the completion of the test without evidence of any run-in period, whereas the CoF for NI, NI-10BN, and NI-10Ag stabilises after 400 s, 600

s, and 800 s, respectively. However, the fluctuations in amplitude are relatively large at 400 °C compared to those at RT.

At 600 °C (Fig. 5.7d), the CoF for NI and NI-10Ag remains steady for the entire duration while the CoF of NI-10BN and NI-10AgBN stabilises after 1400 s. At 800 °C (Fig. 5.7e), the CoF for NI, NI-10Ag, NI-10BN, and NI-10AgBN remains steady for the entire duration, with the occurrence of relatively larger fluctuations in amplitude in NI-10Ag and NI-10AgBN than NI and NI-10BN. It can also be observed that NI-10AgBN has the lowest CoF compared to NI-10Ag, NI-10BN, and NI at all the temperatures (RT, 200 °C, 400 °C, 600 °C and 800 °C).

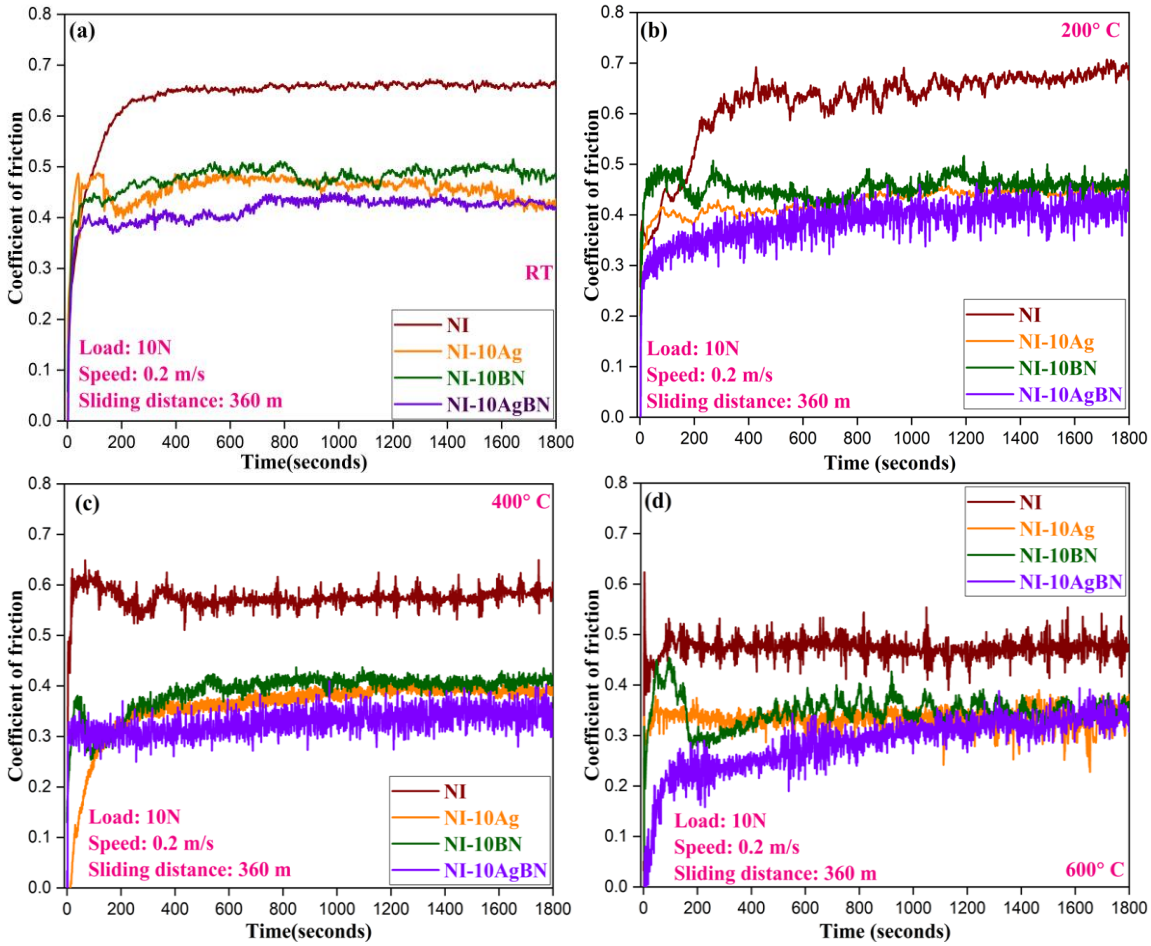

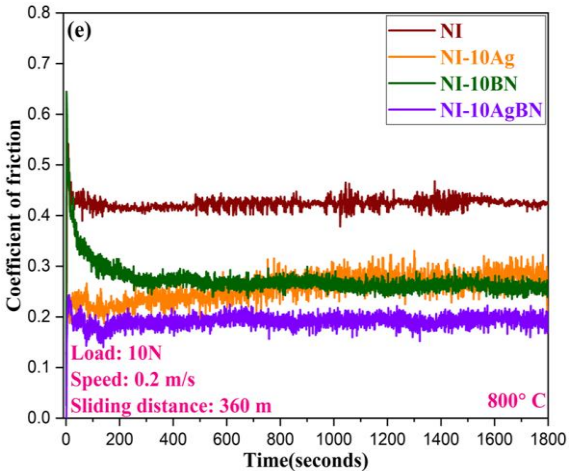

Fig. 5.7: Fluctuation in coefficient of friction with time for Ni_3Al (NI) and composites, NI-10Ag, NI-10BN, and NI-10AgBN at (a) RT, (b) 200 °C, (c) 400 °C, (d) 600 °C and (e) 800 °C.

5.1.3.1.2 Variation of coefficient of friction with temperature

The change in the average CoF with test temperature for NI, NI-10Ag, NI-10BN and NI-10AgBN composites (Fig. 5.8) reveals a decreasing pattern of CoF with increasing temperature for all the materials. It can also be observed that the incorporation of Ag or Cu-*h*BN into Ni_3Al results in a reduction in the average CoF at all temperatures (RT, 200 °C, 400 °C, 600 °C and 800 °C). It is worth noting that the inclusion of a combination of Ag and Cu-*h*BN results in a further decrease in average CoF, pointing towards the presence of a synergetic effect between the two lubricious materials. The NI-10AgBN composite containing equal amount (5 wt.% each) of Ag and Cu-*h*BN has displayed the lowest CoF at all the test temperatures, whereas NI (base Ni_3Al) has shown the highest, as seen from Fig. 5.8. The CoF of NI-10AgBN and NI-10Ag has been observed to decrease from 0.41 to 0.19 and from 0.45 to 0.26, respectively, while the CoF of NI and NI-10BN is found to reduce from 0.65 to 0.42 and from 0.48 to 0.28, respectively, with the increase of temperature from RT to 800 °C.

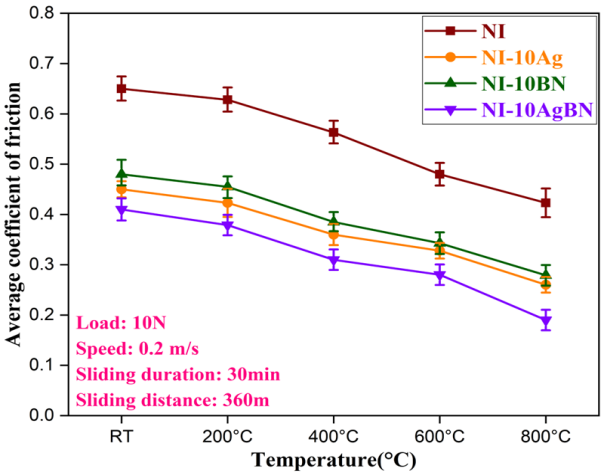

Fig. 5.8: Variation of average coefficient of friction with temperature for NI and its composites, i.e., NI-10Ag, NI-10BN, and NI-10AgBN.

5.1.3.2 Dry sliding wear

5.1.3.2.1 Variation of wear rate with temperature

Figure 5.9 displays the wear rate as a function of temperature for NI, NI-10Ag, NI-10BN, and NI-10AgBN. All samples have been observed to exhibit a similar trend of variation in wear rate with increasing temperatures, i.e., the wear rate increases as the temperature is raised from RT to 400 °C, followed by a decrease beyond that for 600 °C and 800 °C. However, both the increase and decrease in wear rate with temperature are quite significant for NI and NI-10Ag, whereas the same is minor for NI-10BN, and NI-10AgBN, as evident from Fig. 5.9. The wear rate of NI, NI-10Ag, NI-10BN, and NI-10AgBN increased from 3.52 to 5.95 x 10^{-5} mm^3/Nm, 2.96 to 6.66 x 10^{-5} mm^3/Nm, 2.285 to 3.1 x 10^{-5} mm^3/Nm, and 2.185 to 2.95 x 10^{-5} mm^3/Nm, respectively, with increasing temperature from RT to 400 °C. It may also be noticed that the NI-10Ag composite has a higher wear rate compared to NI at 200 °C and 400 °C but a lower rate at RT, 600 °C, and 800 °C. The NI-10BN and NI-10AgBN composites have shown a lower wear rate than NI and NI-10Ag at all temperatures. However, the addition of Ag and Cu-*h*BN in NI-10AgBN has proven to be

efficacious in minimising wear, as it has exhibited the lowest wear rate among all the composites at different temperatures.

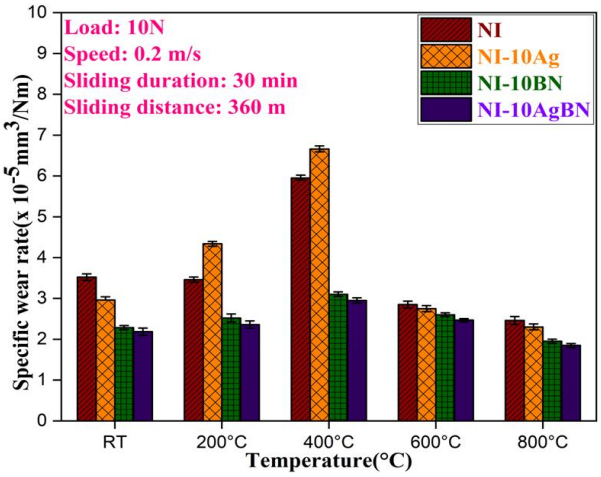

Fig. 5.9: Variation of wear rate with temperature for NI and composites, NI-10Ag, NI-10BN and NI-10AgBN.

5.1.4 Morphology of worn surfaces

5.1.4.1 Field emission scanning electron microscopy of worn composites and counterface ball

Figures 5.10 (a-f) and 5.11 (a-f) depict the worn surface micrographs of Ni_3Al and Si_3N_4 balls after sliding against each other at RT, 200 °C, 400 °C, 600 °C, and 800 °C. The worn scar of NI at RT (Fig. 5.10a) shows evidence of patches of a transfer layer and loose wear debris, while at 200 °C (Fig. 5.10b), it exhibits adhered debris and ploughing. At 400 °C (Fig. 5.10c), it exhibits adhered debris, grooves, and some delamination. At 600 °C (Fig. 5.10d), the worn scar of NI exposes a compact tribo-layer and signs of delamination at a few locations, while at 800 °C (Fig. 5.10e), it has a compact and uniformly distributed tribo-layer, mostly composed of nickel (Ni) and molybdenum (Mo) oxides, as indicated by the elemental maps depicted in Fig. 5.10(f), covering a major portion of the worn area with no noticeable grooves. The formation of a uniform and compact tribo-layer at 600 °C and 800 °C (Figs. 5.10d and e) may have contributed towards lowering the CoF and the rate of

wear compared to RT, 200 °C and 400 °C (Figs. 5.10a to c). The worn track of the Si_3N_4 ball reveals the material transfer from the NI at all the temperatures (Figs. 5.11 a, b, c, d and e), confirmed by EDS analyses and illustrated in Fig. 5.11(f) at 800 °C. One may observe that the transfer layer is smoother and more compact at higher temperatures (600 °C and 800 °C) in comparison to room temperature, 200 °C and 400 °C, as seen from a comparison of Figs. 5.11(a, b and c) and (d and e).

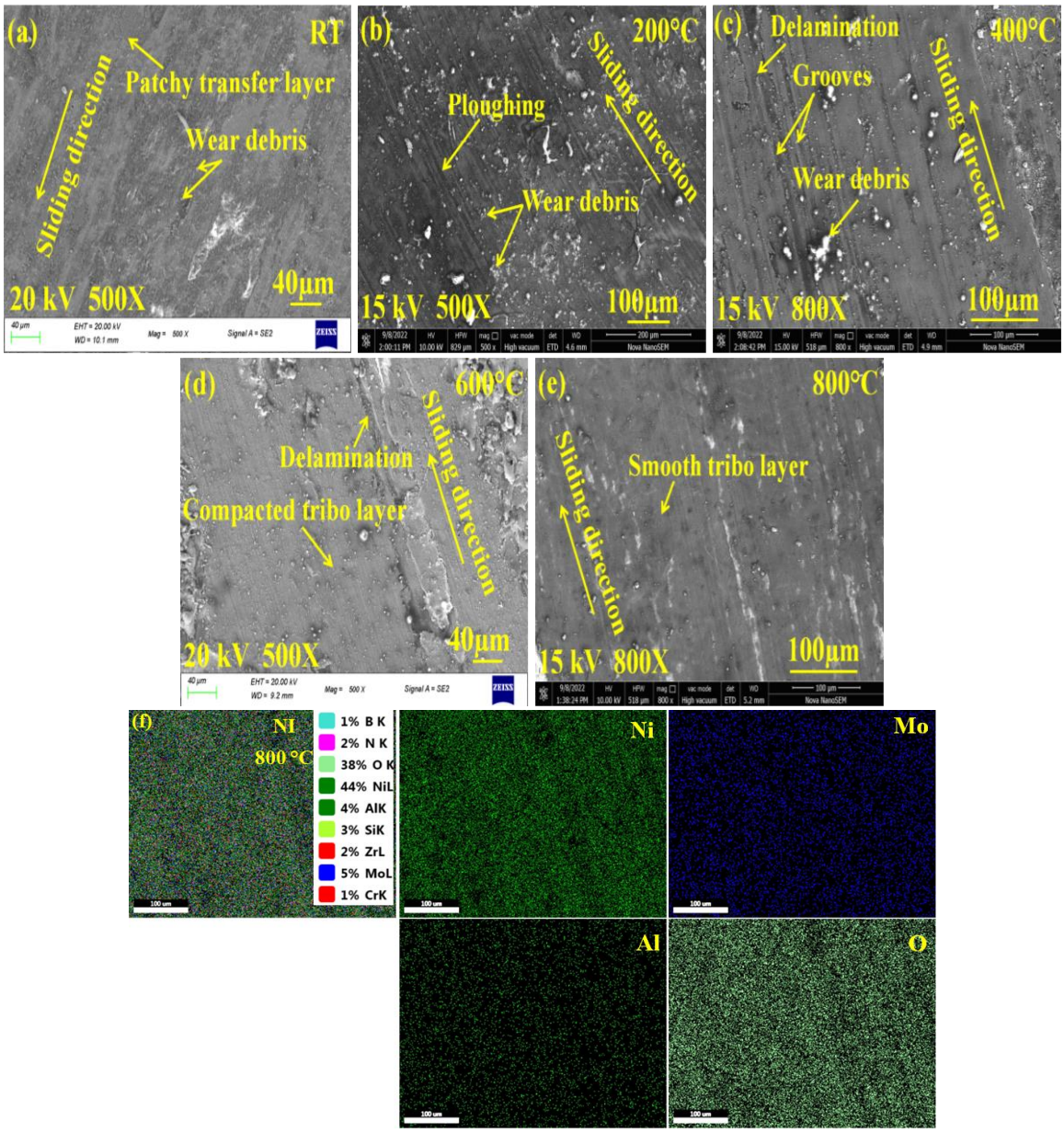

Fig. 5.10: FESEM images of the worn surface of NI composite at (a) RT (b) 200 °C (c) 400 °C (d) 600 °C (e) 800 °C and (f) elemental mapping of worn surface NI at 800 °C.

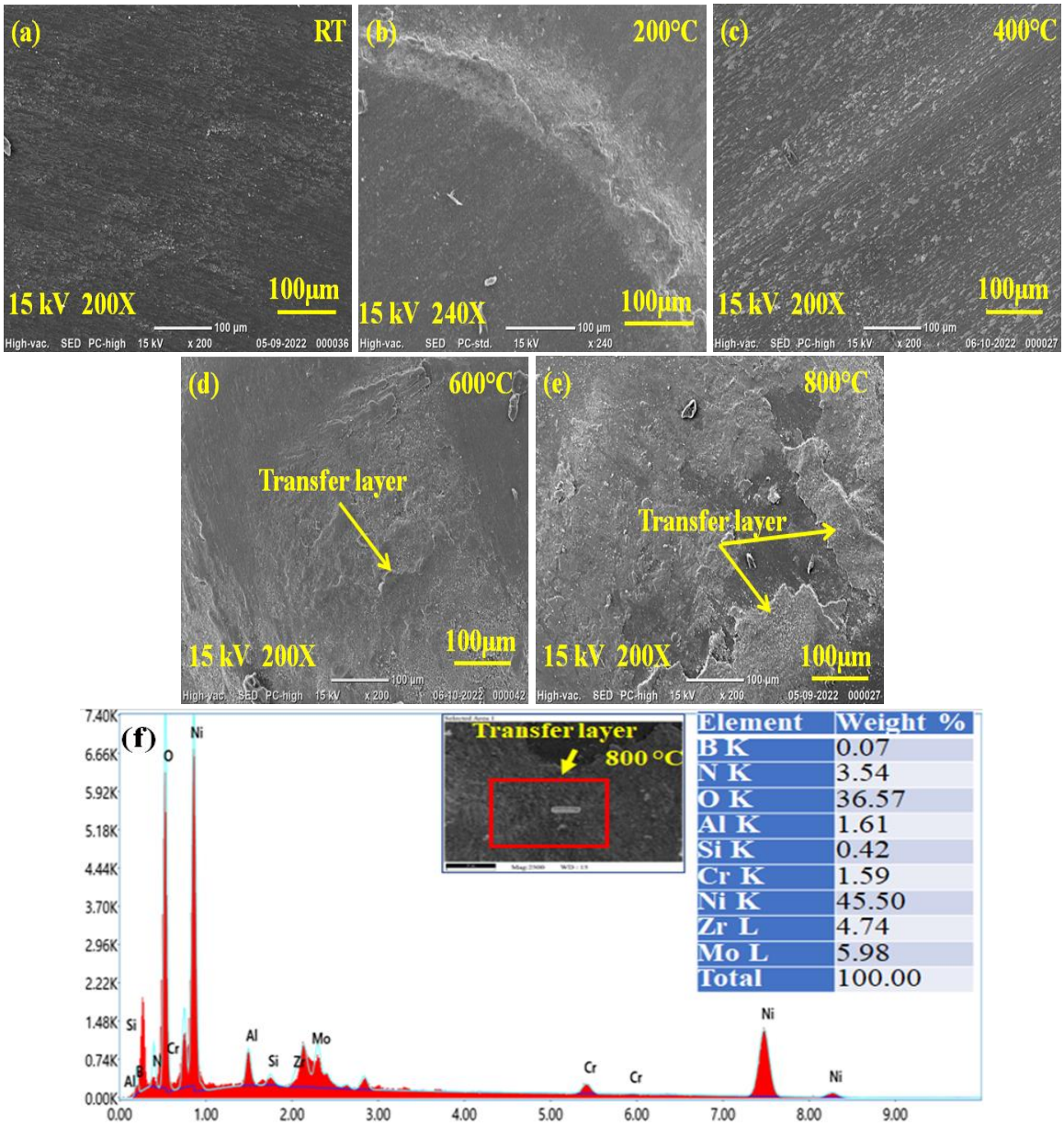

Fig. 5.11: FESEM images of the worn surface of counterface Si_3N_4 ball: (a) RT, (b) 200 °C, (c) 200 °C, (d) 600 °C, (e) 800 °C, and (f) EDS analysis of the ball at 800 °C.

The morphologies of the surfaces of NI-10Ag composite and Si_3N_4 balls worn at different temperatures are presented in Figs. 5.12(a-f) and 5.13(a-f). At room temperature (Fig. 5.12a), the worn track is characterised by loose wear particles, ploughing marks, and a tribo-layer over the wear track, while at 200 °C (Fig. 5.12b), it shows the presence of wear debris and patchy transfer layer. At 400 °C (Fig. 5.12c), a compacted layer of wear debris is evident besides ploughing, whereas at 600 °C and 800 °C (Figs. 5.12d and e), the worn

track has a glazed layer as well as a compacted tribo-layer containing silver (Ag), as validated by elemental maps of worn NI-10Ag at 800 °C depicted in Fig. 5.12(f). The presence of higher wt.% of Ag and O in the tribo-layer at 800 °C may have resulted in a reduced coefficient of friction and wear rate compared to 400 °C. At RT, 200 °C, 400 °C, 600 °C and 800 °C, there is clear evidence of the transfer of NI-10Ag composite material to the Si_3N_4 ball, as illustrated in Figs. 5.13(a-e), forming a firmly bound and continuous protective transfer layer on the worn area of the Si_3N_4 ball at elevated temperatures (600 °C and 800 °C), as depicted in Figs. 5.13(d and e). The transfer of material has been confirmed by the EDS examination of the worn surface of the Si_3N_4 ball at 800 °C (Fig. 5.13f), and the existence of Ag in the transfer layer on the Si_3N_4 ball may also have contributed to the improved tribological properties by facilitating smooth shearing at the contact interface.

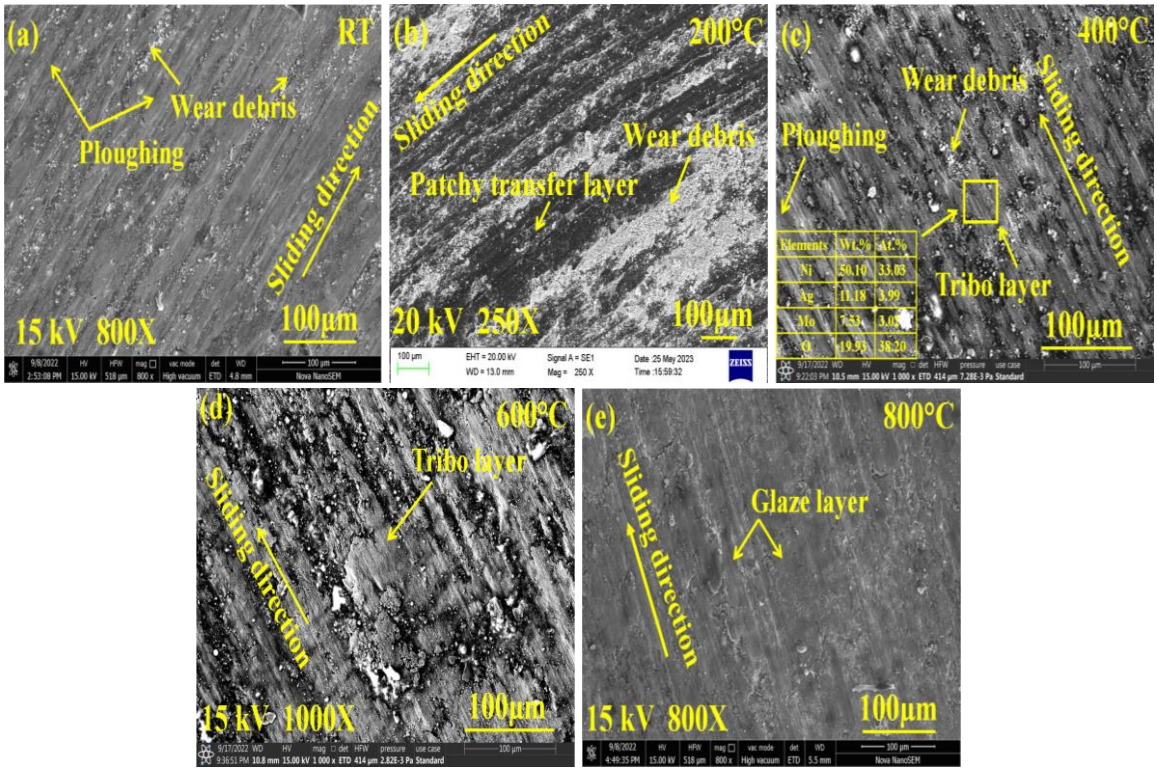

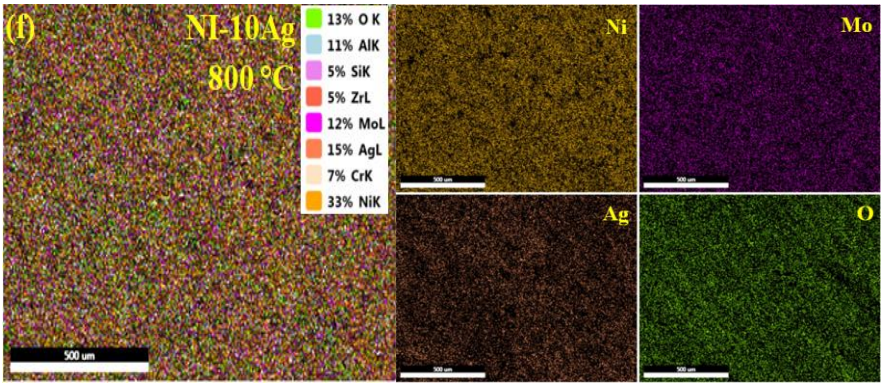

Fig. 5.12: FESEM images of the worn surface of NI-10Ag composite at (a) RT (b) 200 °C (c) 400 °C (d) 600 °C (e) 800 °C and (f) elemental mapping of worn NI-10Ag at 800 °C.

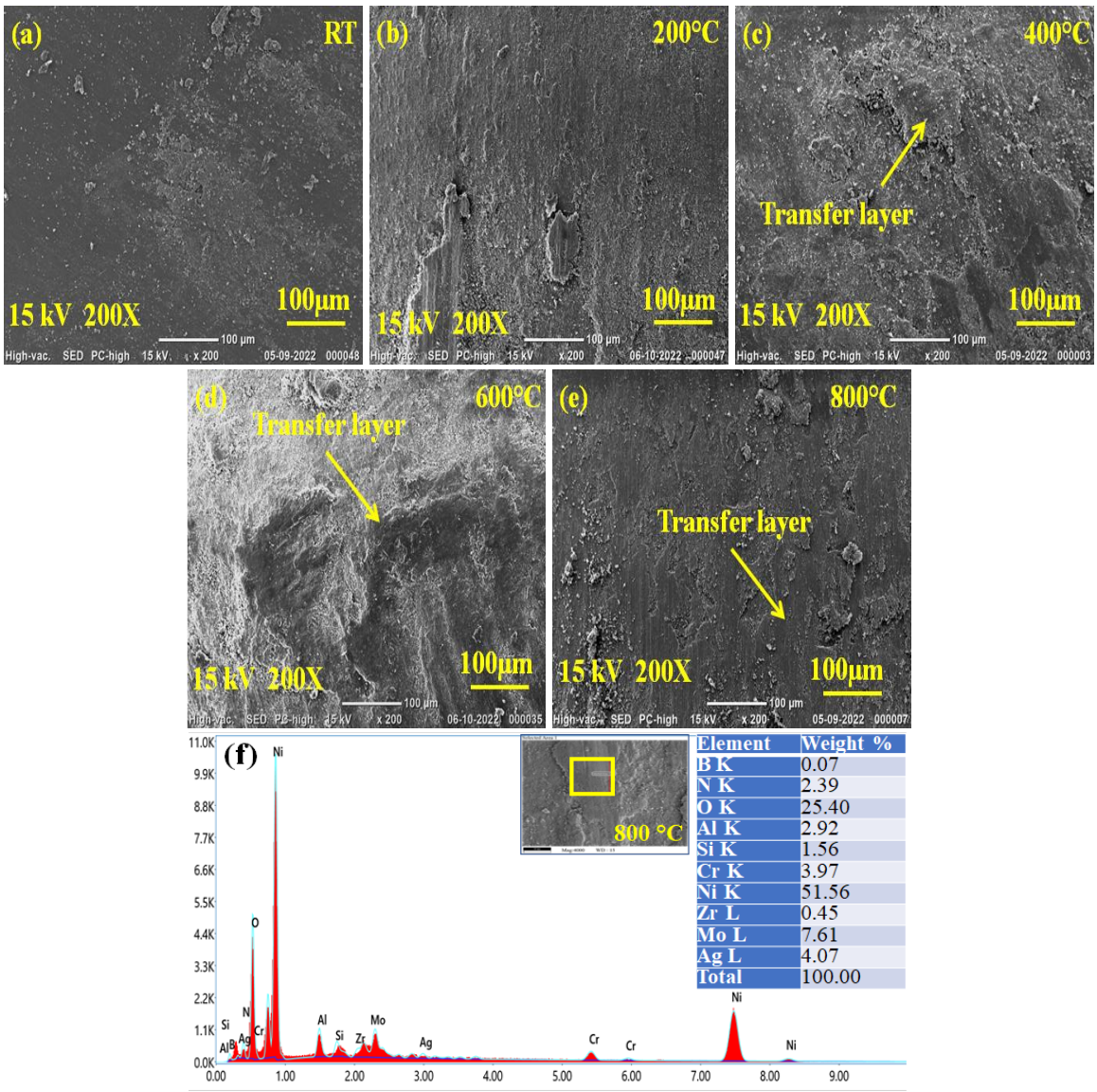

Fig. 5.13: FESEM images of the worn surface of counterface Si_3N_4 ball: (a) RT, (b) 200 °C, (c) 200 °C, (d) 600 °C, (e) 800 °C, and (f) EDS analysis of the ball at 800 °C.

The micrographs shown in Figs. 5.14(a-f) and 5.15(a-f) illustrate the worn surfaces of NI-10BN composite and its counterpart (Si_3N_4 balls) at various temperatures ranging from room temperature (RT) to 800 °C. The worn surface at room temperature (Fig. 5.14a) exhibits the existence of a transfer layer that seems to have delaminated at several sites. In contrast, at 200 °C (Fig. 5.14b) and 400 °C (Fig. 5.14c), the worn scar exposes the presence of a continuous tribo-layer with delamination at a few locations, along with some wear debris. However, the worn surface possesses a relatively thick and compact tribo-layer, which appears to be cracked at a few places at 600 °C (Fig. 5.14d). At 800 °C (Fig. 5.14e), the tribo-layer appears to be quite smooth, well-compacted, and covers a larger area of wear track without any sign of abrasion and ploughing. The elemental mapping (Fig. 5.14f) of the contact area of the NI-10BN composite at 800 °C (Fig. 5.14e) confirms the presence of Ni, Mo, O, Cu, B, and N. One may also observe the presence of a transfer layer of wear debris on the surface of Si_3N_4 ball (Figs. 5.15a to e) with varying degree of area coverage and level of compaction. The EDS spectrum (Fig. 5.15f) of the transfer layer marked by the arrow on Fig. 5.15(e) confirms the transfer of material from NI-10BN composite to the counterpart Si_3N_4 ball.

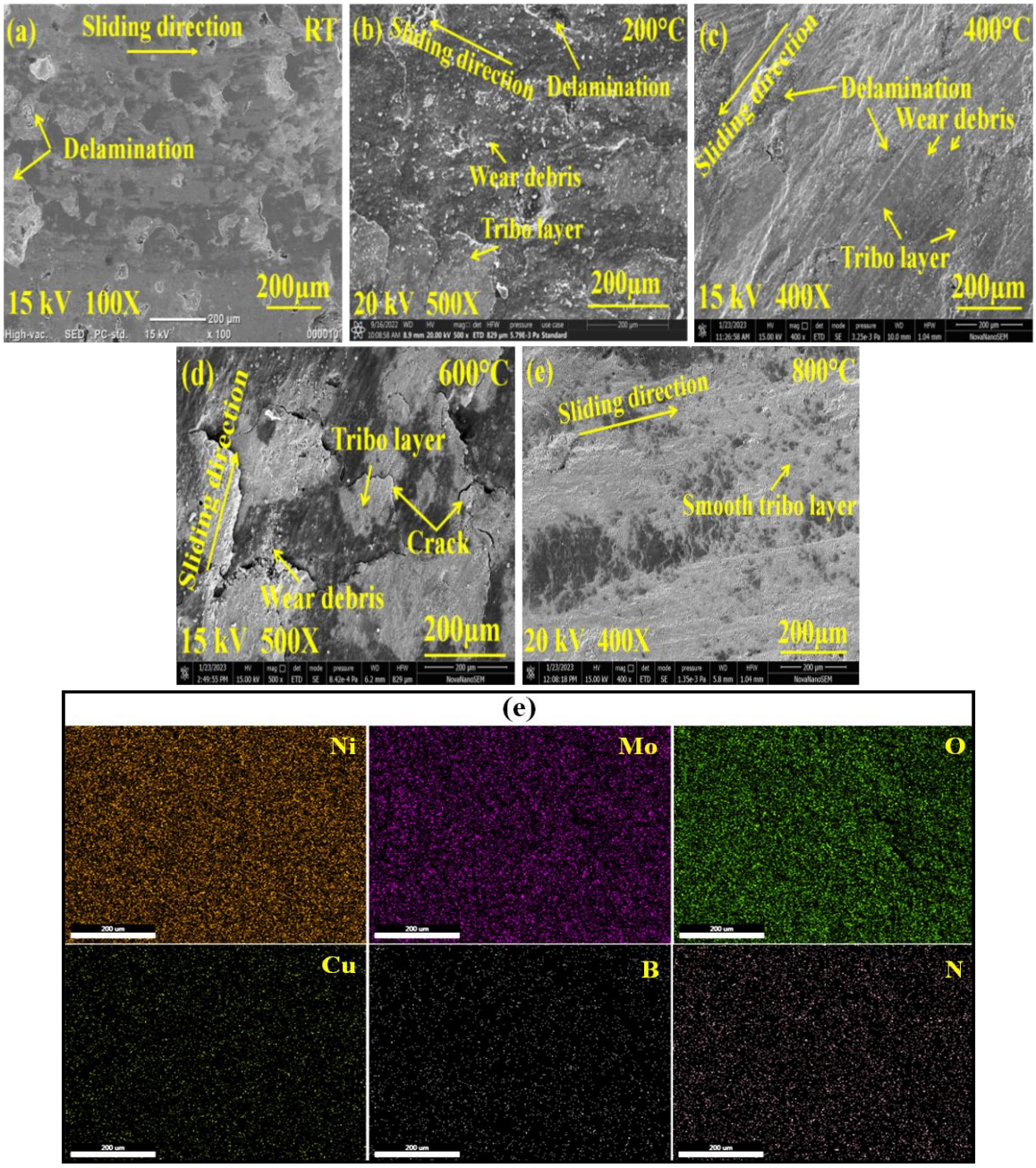

Fig. 5.14: FESEM images of the worn surface of NI-10BN composite at (a) RT (b) 200 °C (c) 400 °C (d) 600 °C (e) 800 °C and (f) elemental mapping of worn NI-10BN at 800 °C.

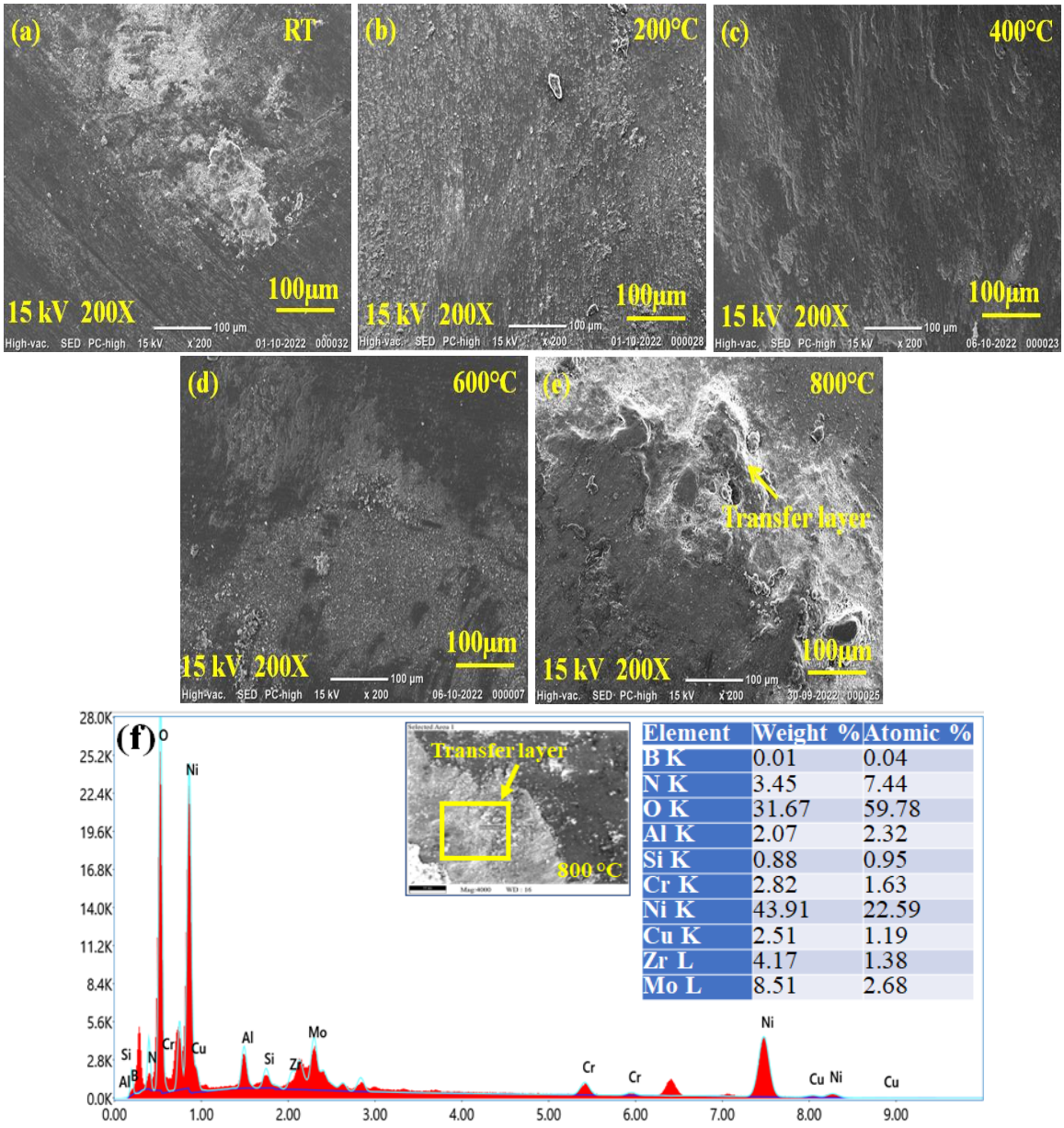

Fig. 5.15: FESEM images of the worn surface of counterface Si_3N_4 ball: (a) RT, (b) 200 °C, (c) 400 °C, (d) 600 °C, (e) 800 °C, and (f) EDS analysis of the ball at 800 °C.

The FESEM micrographs in Figs. 5.16(a-f) and 5.17(a-f) illustrate the morphology of the worn surfaces of the NI-10AgBN composite and Si_3N_4 ball after the tribological tests at various temperatures (RT, 200 °C, 400 °C, 600 °C and 800 °C). At room temperature (RT), the worn surface of NI-10AgBN (Fig. 5.16a) exhibits sliding marks, loose wear debris, and a patchy transfer layer. On the other hand, at 200 °C and 400 °C, the worn surface of NI-10AgBN exhibits some ploughing marks, wear particles, and a tribo-layer, as illustrated in

Figs. 5.16(b and c). The worn surface at 600 °C (Fig. 5.16d) displays the existence of wear debris and a smooth tribo-layer whereas at 800°C (Fig. 5.16e) it reveals the presence of a smooth and compact tribo-layer with a glaze layer primarily composed of Ni, Mo, Ag, O, Cu, B, and N elements, as illustrated by the elemental maps of the worn NI-10AgBN surface (Fig. 5.16f). The transfer of material from the NI-10AgBN composite to the Si_3N_4 ball has been confirmed through the elemental mapping (Fig. 5.17f) of the worn scar of the Si_3N_4 ball at 800 °C (Fig. 5.17e), which indicates the presence of elements such as Ni, Mo, Ag, O, Cu, B, and N in a transfer layer with a varying degree of coverage area and level of compaction, as depicted in Figs. 5.17(a-e). It may also be observed that Ni, Mo, Ag, Cu, B, N, and O elements cover most of the contact area of the NI-10AgBN composite and the counterpart Si_3N_4 ball.

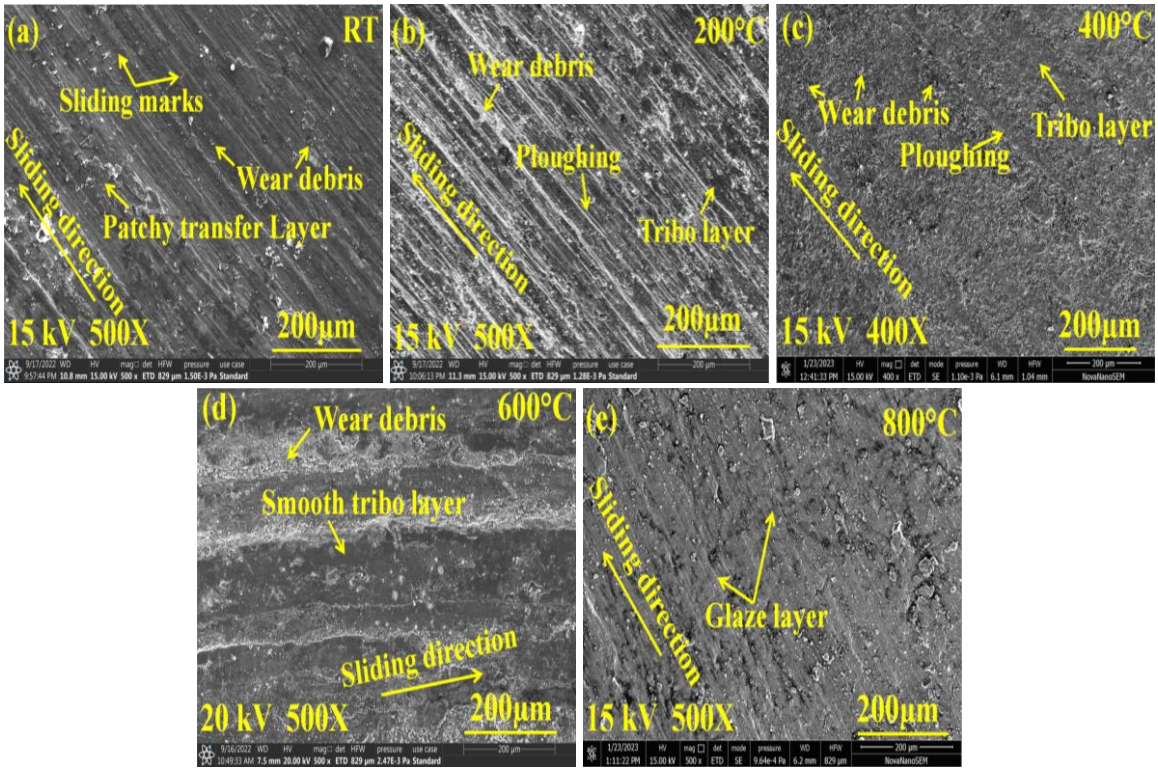

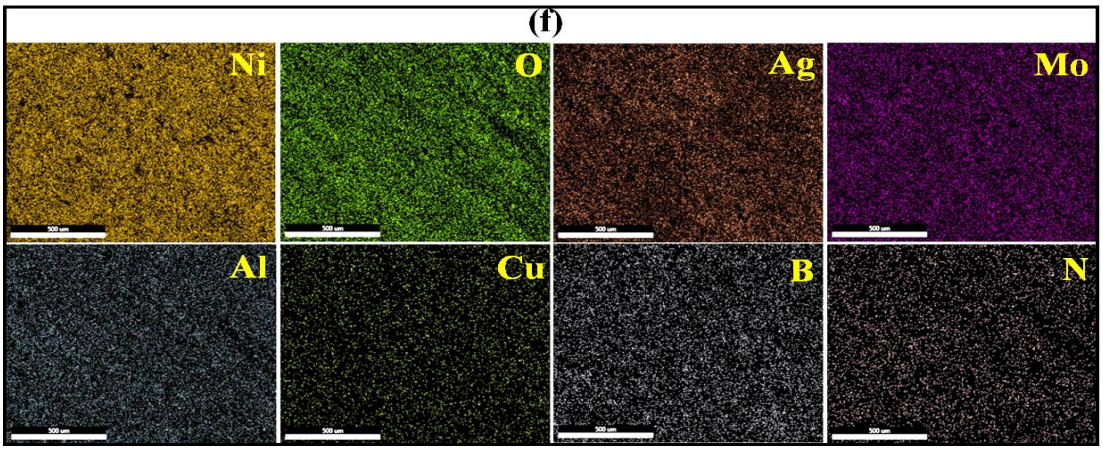

Fig. 5.16: FESEM images of the worn surface of NI-10AgBN composite at (a) RT (b) 200 °C (c) 400 °C (d) 600 °C (e) 800 °C and (f) elemental mapping of worn NI-10BN at 800 °C.

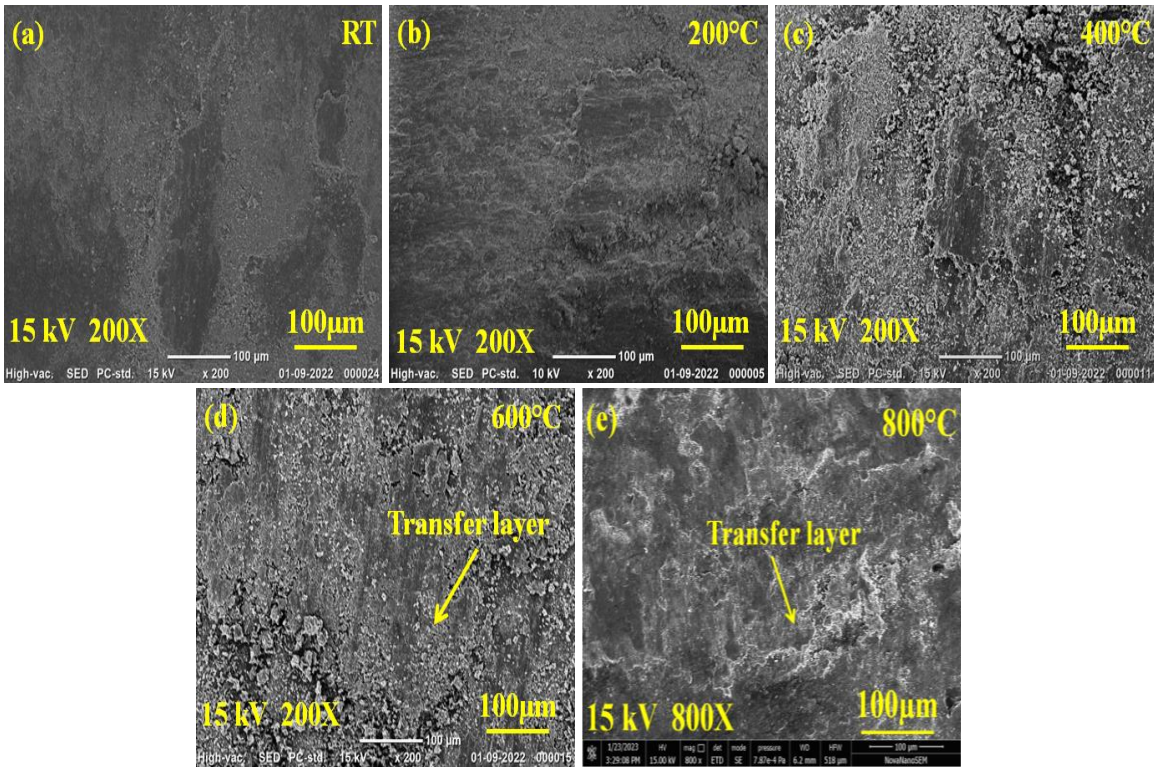

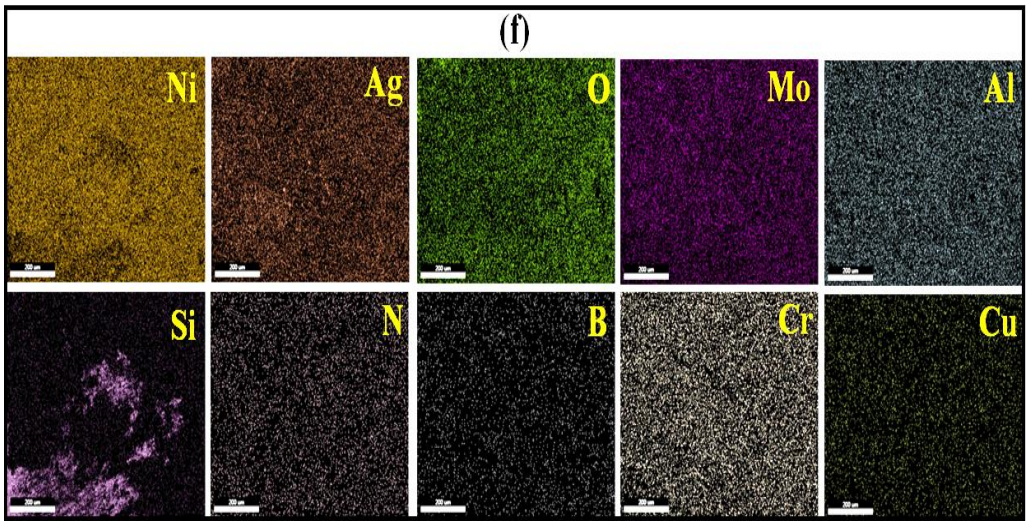

Fig. 5.17: FESEM images of the worn surface of counterface Si_3N_4 ball: (a) RT, (b) 200 °C, (c) 200 °C, (d) 600 °C, (e) 800 °C, and (f) elemental mapping of worn ball at 800 °C.

5.1.4.2 X-ray diffraction analysis of worn composites

Figures 5.18(a–d) show the XRD patterns of the worn surfaces of NI, NI-10Ag, NI-10BN, and NI-10AgBN at different temperatures. The XRD pattern of NI (Fig. 5.18a) indicates the presence of diffraction peaks of Ni_3Al (ICSD Ref. No. 03-065-0430) at RT, whereas additional peaks of $NiMoO_4$ (ICSD Ref. No. 00-045-142) and MoO_3 (ICSD Ref. No. 00-021-0569) are seen at 200 °C. However, at 400 °C and 600 °C, peak corresponding to NiO (ICSD Ref. No. 01-089-7130) also appears along with $NiMoO_4$ and MoO_3, while at 800 °C, peaks belonging to NiO and $NiMoO_4$ are observed with no signature of MoO_3. Figure 5.18(b) demonstrates the XRD patterns of NI-10Ag, revealing the existence of Ni_3Al and Ag (ICSD Ref. No. 01-087-0598) at RT, whereas peaks of $NiMoO_4$ and MoO_3 could be observed at 200 °C and that of NiO at 400 °C. However, the peaks corresponding to $Ag_2Mo_2O_7$ (ICSD Ref. No. 00-021-1339) and Ag_2MoO_4 (ICSD Ref. No. 00-008-473) have been observed at 600 °C and 800 °C, in addition to the diffraction peaks for NiO, Ag, MoO_3, and $NiMoO_4$ at 600 °C and NiO, Ag, and $NiMoO_4$ at 800 °C. XRD patterns of NI-10BN depicted in Fig. 5.18(c) demonstrate the presence of Ni_3Al at RT, whereas at 200 °C peaks corresponding to CuO (ICSD Ref. No. 01-078-0428), MoO_3, $NiMoO_4$, and *h*BN (ICSD

Ref. No. 01-073-2095) are also observed. However, at 400 and 600 °C, new diffraction peaks of NiO are observed along with *h*BN, $NiMoO_4$, CuO, and MoO_3, and at 800 °C, diffraction peaks belonging to NiO, *h*BN, CuO, and $NiMoO_4$ are detected. The X-ray diffraction pattern of worn NI-10AgBN composite illustrated in Fig. 5.18(d) establishes the presence of diffraction peaks belonging to Ni_3Al at room temperature (RT) and 200 °C, and that of Ag and *h*BN from RT to 800 °C, Ag_2MoO_4 and $Ag_2Mo_2O_7$ peaks from 600 °C to 800 °C, CuO peaks from 400 °C to 800 °C, MoO_3 peaks from 200 °C to 600 °C, and $NiMoO_4$ peaks from 200 °C to 800 °C.

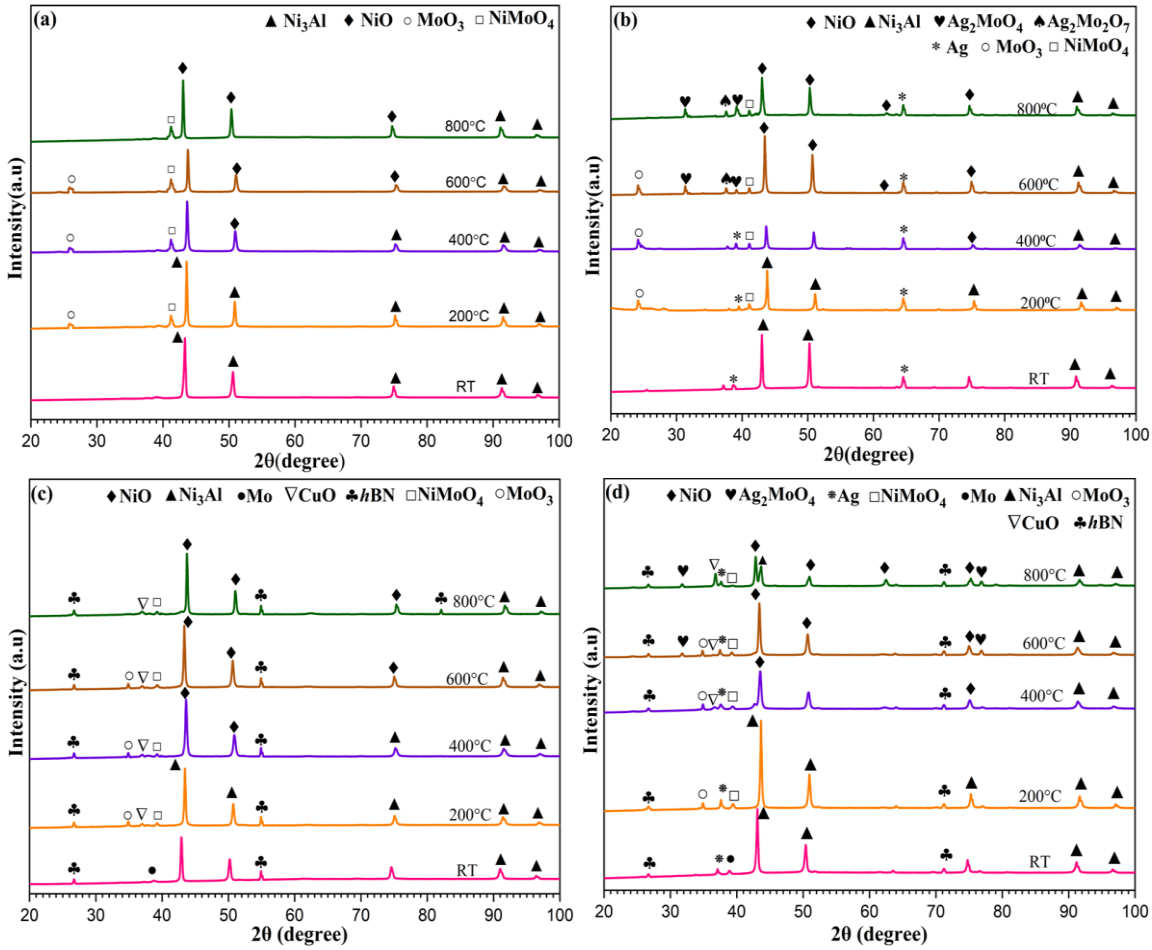

Fig. 5.18: XRD patterns of worn specimens (a) NI, (b) NI-10Ag, (c) NI-10BN, and (d) NI-10AgBN at different temperatures.

5.1.4.3 Raman spectroscopy of worn composites

Figures 5.19(a-d) show the Raman spectra of worn specimens of NI, NI-10Ag, NI-10BN, and NI-10AgBN after tribo-tests at RT, 200 °C, 400 °C, 600 °C, and 800 °C, respectively. The spectra of the worn NI given in Fig. 5.19(a) show the presence of $NiMoO_4$ from 200 °C to 800 °C, while new peaks belonging to NiO and MoO_3 appear along with $NiMoO_4$ at 400 °C, 600 °C, and 800 °C, respectively. The spectra of the worn scar of NI-10Ag composite (Fig. 5.19b) reveal the presence of $NiMoO_4$ peaks from 200 °C to 800 °C and those corresponding to Ag_2MoO_4, NiO, and MoO_3 at 400 °C, 600 °C, and 800 °C. However, additional peaks of $Ag_2Mo_2O_7$ are seen at 600 °C and 800 °C, as evident from Fig. 5.19(b). The spectra for NI-10BN composite reveal the peaks attributable to *h*BN from RT to 800 °C, and CuO and $NiMoO_4$ from 200 °C to 800 °C, while NiO and MoO_3 are observed at 400 °C, 600 °C, and 800 °C (Fig. 5.19c). The worn surface of NI-10AgBN composite exhibits peaks pertaining to *h*BN from RT to 800 °C, CuO and $NiMoO_4$ from 200 °C to 800 °C, and Ag_2MoO_4, NiO, and MoO_3 from 400 °C to 800 °C apart from $Ag_2Mo_2O_7$ at 600 °C and 800 °C, as illustrated in Fig. 5.19(d). Previous studies have indicated that tribo-chemical reactions occurring on the worn surface result in the formation of Ag_2MoO_4 at temperatures exceeding 400 °C and have reported that *h*BN, Ag_2MoO_4, $Ag_2Mo_2O_7$, MoO_3, NiO, CuO, and $NiMoO_4$ offer effective lubrication at elevated temperatures by forming an easy-to-shear film at the interface [25,64,144–146].

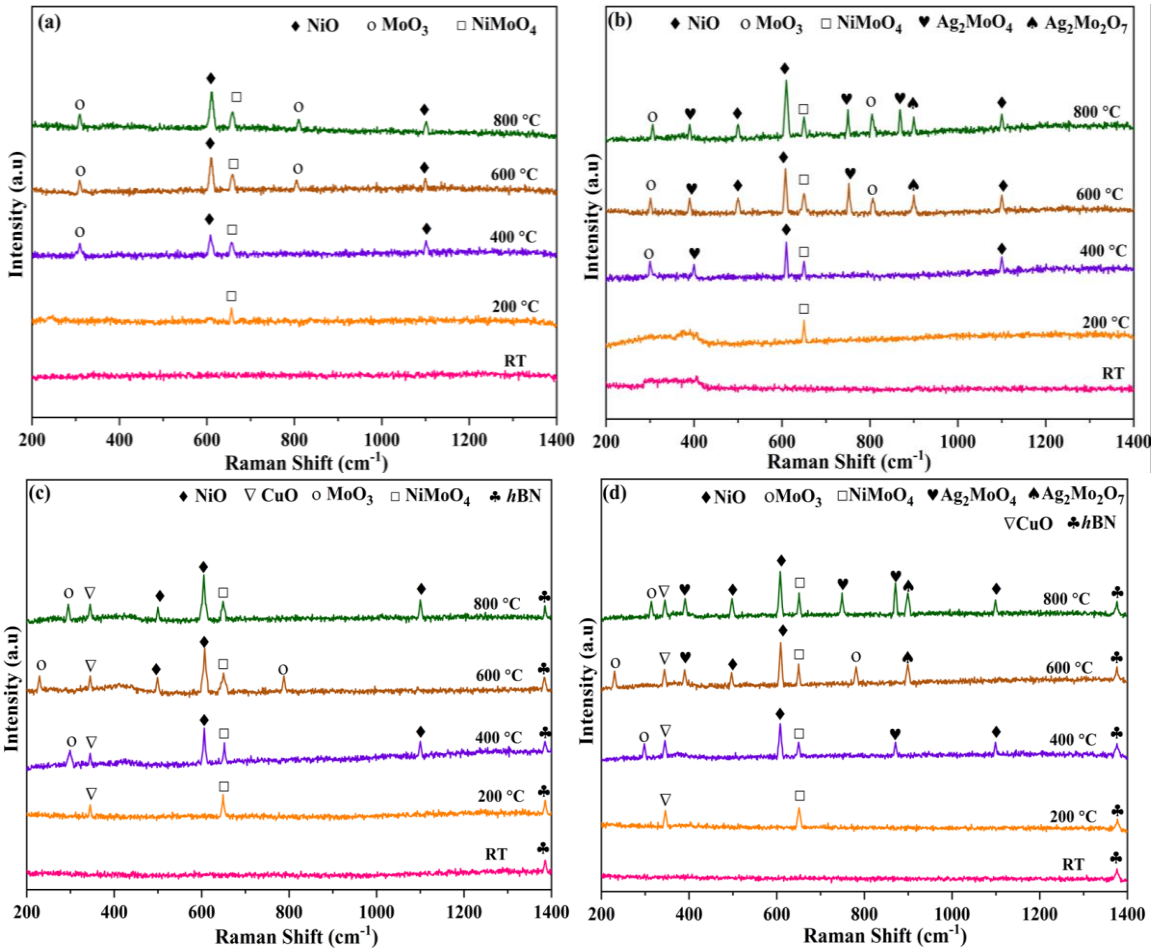

Fig. 5.19: Raman spectra of worn specimens of (a) NI, (b) NI-10Ag, (c) NI-10BN, and (d) NI-10AgBN at various temperatures.

5.1.4.4 Examination of subsurface

FESEM-backscattered (BSE) images of the cross-section of the worn specimens of NI, NI-10Ag, NI-10BN and NI-10AgBN at 800 °C, illustrated in Fig. 5.20, show the presence of a tribo-layer along with the respective EDS analysis. The EDS analysis of tribo-layer (Fig. 5.20a) observed on the worn surface of NI confirms the presence of oxides of Ni and Mo, which is consistent with the results of XRD (Fig. 5.18a) and Raman spectroscopy (Fig. 5.19a). The EDS analysis of the tribo-layer formed on the worn NI-10Ag (Fig. 5.20b) reveals a predominant presence of elements including O, Ni, Ag and Mo. These EDS findings are in consonance with the results of XRD (Fig. 5.18b) and Raman spectroscopy (Fig. 5.19b), suggesting an increased formation of Ag_2MoO_4, $Ag_2Mo_2O_7$, NiO, MoO_3 and

$NiMoO_4$ on the worn surface of NI-10Ag with the increase of temperature. The EDS analysis (Fig. 5.20d) of the tribo-layer seen on NI-10BN at 800 °C (Fig. 5.20c) reveals the presence N, O, Mo, Cu, Ni, Zr, B, Al, Cr and Si which is consistent with the XRD (Fig. 5.18c) and Raman spectroscopy (Fig. 5.19c) confirming the presence of *h*BN and NiO, CuO, MoO_3 and $NiMoO_4$. The EDS analysis of glaze layer (Fig. 5.20f) observed on the worn surface of NI-10AgBN (Fig. 5.20e) also confirms the presence of *h*BN and oxides of Ni, Ag, Mo and Cu in the glaze layer which is also commensurate with the results of XRD (Fig. 5.18d) and Raman spectroscopy (Fig. 5.19d). The average thickness of the glaze layer formed on worn surface of NI-10AgBN at 800 °C (Fig. 5.20e) is observed to be larger (25.19 μm) in comparison to the layers observed on NI-10BN (15.72 μm), NI-10Ag (11.25 μm) and NI (5.61 μm).

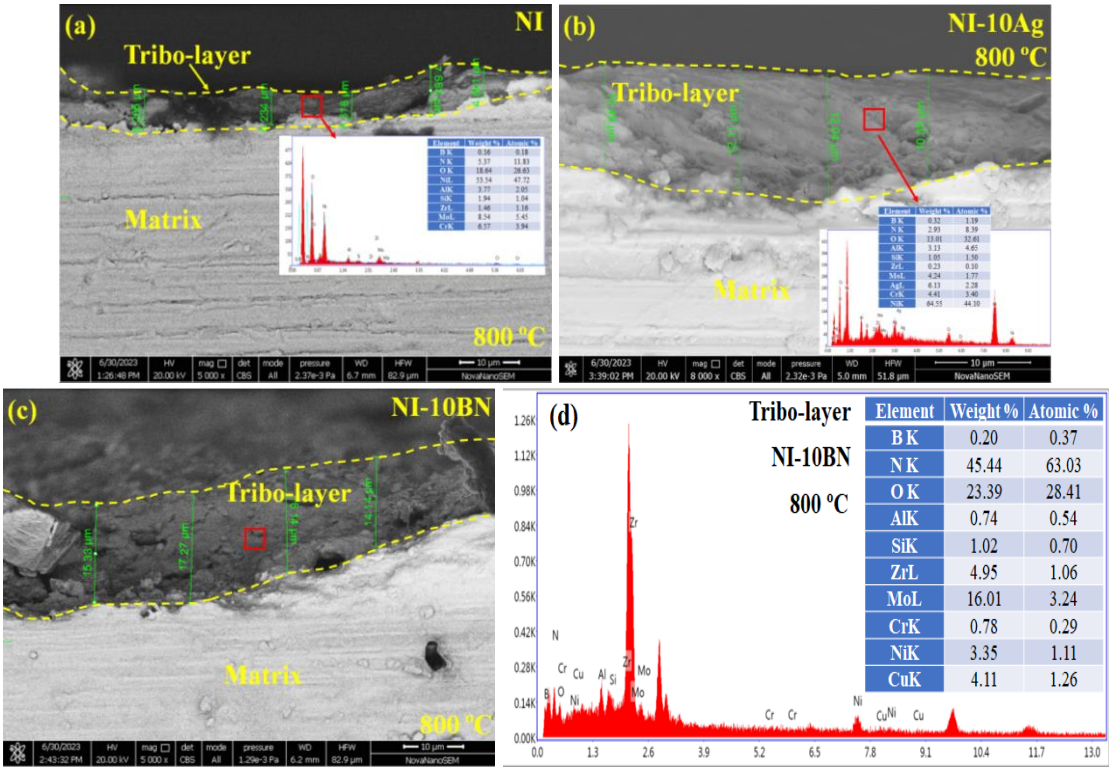

Element	Weight %	Atomic %
B K	0.20	0.37
N K	45.44	63.03
O K	23.39	28.41
AlK	0.74	0.54
SiK	1.02	0.70
ZrL	4.95	1.06
MoL	16.01	3.24
CrK	0.78	0.29
NiK	3.35	1.11
CuK	4.11	1.26

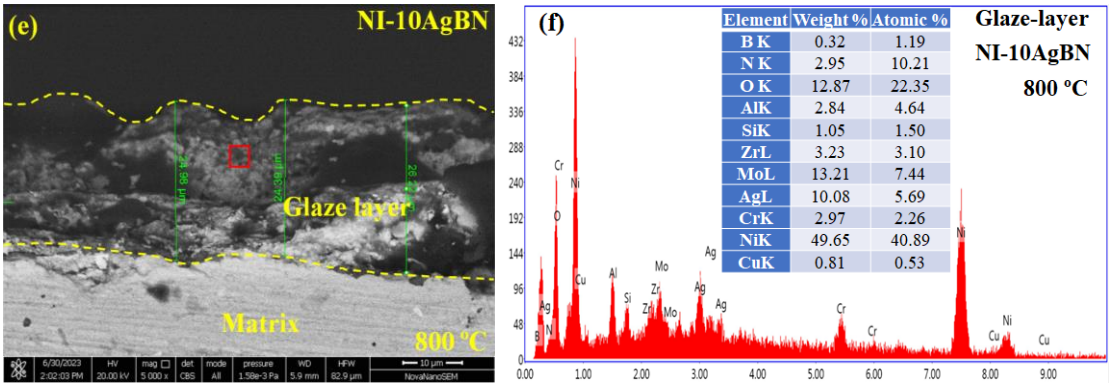

Fig. 5.20: FESEM micrographs (backscattered mode) and EDS analysis of cross-section of worn track at 800 °C corresponding to (a) NI, (b) NI-10Ag, (c and d) NI-10BN, and (e and f) NI-10AgBN composites.

5.2 Discussions: Friction and Wear behaviour of Ni_3Al-Ag/Ni_3Al-Cu-*h*BN/Ni_3Al-Ag-Cu-*h*BN composites

The addition of Ag, Cu-*h*BN or a combination of both in Ni_3Al results in a decrease in hardness, as seen from Table 5.1, primarily because of the inherent softness of Ag and *h*BN, indicating that the incorporation of soft phases reduces the brittleness of Ni_3Al and improves the ductility**.** However, the reduction in hardness is relatively more in the composite containing only Ag, i.e. Ni_3Al-Ag than Ni_3Al-Cu-*h*BN or Ni_3Al-Ag-(Cu-*h*BN). The coefficient of friction (CoF) has been observed to fluctuate initially for NI as well as the composites (Fig. 5.7). These fluctuations might be caused by the initial surface roughness of the mating bodies. As the sliding progresses, the asperities get evened out and the surfaces become smoother, leading to attainment of better conformity with each other and consequent stabilisation of coefficient of friction (CoF), as suggested earlier by Tyagi et al. [147]. The NI-10Ag and NI-10AgBN show comparatively larger fluctuations than NI and NI-10BN, which may be due to their comparatively reduced hardness, allowing the harder asperities of the Si_3N_4 ball to penetrate and cause abrasion.

The observed trend of CoF and wear rate as a function of temperature for NI, NI-10Ag, NI-10BN, and NI-10AgBN (Figs. 5.8 and 5.9) are collectively attributed to several factors,

which include the existence of loose particles resulting from wear, the transfer layer characteristics (patchy or continuous, loosely attached or well-compacted), the extent of area coverage of the transfer layer, and the presence of lubricious species on the worn surfaces of mating bodies. The presence of loose wear particles results in abrasion whereas a loosely bound, patchy and discontinuous transfer layer offers an opportunity for direct contact between mating materials, leading to a higher coefficient of friction and material loss. However, a well-compacted and continuous transfer layer prevents direct contact between tribo-pair and results in a decrease in both friction and wear.

The presence of grooves, loose wear debris, ploughing, delamination at some locations and a discontinuous transfer layer of wear debris on the surface of Ni_3Al worn at RT, 200 °C and 400 °C (Figs. 5.10 a to c) may have caused a higher coefficient of friction (Fig. 5.8) and wear rate (Fig. 5.9). However, a marked decrease in coefficient of friction and wear rate beyond 400 °C i.e., at 600 °C and 800 °C may be attributed to the formation of a well-compacted and continuous tribo-layer containing oxides of Ni and Mo such as NiO, $NiMoO_4$, and MoO_3, on the worn surfaces of the NI (Figs. 5.10d and e) and the Si_3N_4 ball (Figs. 5.11d and e), which are reported to have lubricating property [131,148]. The elemental mapping, EDS analysis, XRD and Raman spectra of Ni_3Al (Figs. 5.10(f), 5.11(f), 5.18(a), 5.19(a) and 5.20(a)) have confirmed the presence of these oxides. The presence of a compacted and continuous layer on the contact region acts as a protective barrier and hinders direct contact between mating materials, whereas the lubricious oxides provide easy shearing capability at the contact interface, both of which are beneficial in reducing friction and wear.

The reduction in the CoF observed in NI-10Ag composite from room temperature (RT) to 400 °C may be ascribed to the lubricating potential of Ag as it gets diffused to the worn region to establish easy-to-shear junctions at the sliding interface [149,150]. The EDS

analyses of the tribo-layer have demonstrated the presence of Ag, as depicted in Fig. 5.12(c). However, the reduction in CoF and wear rate beyond 400 °C may be attributed to the formation of a glazed layer and compacted tribo-layer at 600 °C and 800 °C, as seen from Figs. 5.12(d and e), consisting of lubricious oxides such as Ag_2MoO_4, $Ag_2Mo_2O_7$, NiO, $NiMoO_4$, and MoO_3, as evidenced by XRD (Fig. 5.18b) and Raman spectra (Fig. 5.19b). The presence of loose wear particles, grooves and a discontinuous transfer layer on the worn NI-10Ag and the counterpart Si_3N_4 ball surfaces, as illustrated in Figs. 5.12(c) and 5.13(c), which in turn may have allowed direct contact between the counterpart ball and composite disc, leading to a comparatively higher material loss from the NI-10Ag composite and hence the considerable increase in the wear rate up to 400 °C (Fig. 5.9). The wear rate reduction beyond 400 °C can be explained by the development of a well-compacted and continuous transfer layer on the contact area of NI-10Ag and the counter Si_3N_4 ball, inhibiting the mating materials from establishing direct contact. Elemental mapping and EDS analysis, as illustrated in Figs. 5.12(f), 5.13(f), and 5.20(b) indicate that oxides of Ag, Ni, and Mo have formed over the worn area of NI-10Ag and its counterpart, Si_3N_4 ball. The presence of an oxide-based transfer layer having lubricious properties over the worn tracks of composite and counterface, as depicted in Figs. 5.12(e) and 5.13(e) assist in lowering the coefficient of friction and wear rate by avoiding direct contact between the composite and its counterpart, which furnishes easy-to-shear interface junctions. It has been reported that silver molybdate (Ag_2MoO_4 and $Ag_2Mo_2O_7$) is a solid lubricant at high temperatures [25,60,137,151] that develops over 500 °C, and its formation is evident at higher temperatures (600 and 800 °C), as illustrated in Figs. 5.18(b) and 5.19(b). At RT-800 °C, the coefficient of friction of the NI-10Ag composite is consistently lower in comparison to NI (Fig. 5.8) despite having a lower hardness than Ni_3Al. This suggests that Ag functions as a lubricant within the temperature range of RT to 400 °C, while its

molybdates serve this purpose at temperatures beyond 500 °C. However, at 200 °C and 400 °C, the wear rate of Ni_3Al-10Ag is relatively higher than that of Ni_3Al (Fig. 5.9), which indicates that at relatively lower temperatures, the hardness of the material outweighs the lubricating capability of Ag, which fails to develop a tribo-layer on the contact surface and results in direct interaction of the composite and the counter Si_3N_4 ball, leading to greater material loss. However, at 600 °C and 800 °C, a tribo-layer with an average layer thickness of 11.25 μm formed on the worn region of NI-10Ag (Figs. 5.12d-e and 5.20b) and the transfer layer formed on the worn scar of counter Si_3N_4 (Figs. 5.13d and e) ball might have inhibited the direct contact, resulting in a lower wear rate than NI.

The existence of wear particles, delamination, and a scattered transfer layer at 400 °C over the worn surface of NI-10BN (Figs. 5.14b and c) and Si_3N_4 ball (Figs. 5.15b and c) suggest the chance of coming into direct contact with mating materials, leading to comparatively more significant material loss, which may explain the increasing trend of wear rate with increasing temperature from RT to 400 °C (Fig. 5.9). Nonetheless, a reduction in CoF and wear rate at temperature of 600 °C and above is ascribed to the generation of a smooth, compact, and continuous tribo-layer on the contact area of NI-10BN composite (Figs. 5.14d and e) and well-compacted transfer layer on counterpart Si_3N_4 ball (Figs. 5.15d and e) comprising lubricious materials, such as *h*BN, NiO, CuO, $NiMoO_4$, and MoO_3, as verified by the elemental mapping and EDS analyses (Figs. 5.14f and 5.15f), XRD (Fig. 5.18c), and Raman spectra (Fig. 5.19c). The EDS analysis (Fig. 5.20d) of the tribo-layer seen on NI-10BN at 800 °C (Fig. 5.20c) reveals the presence N, O, Mo, Cu, Ni, Zr, B, Al, Cr and Si which is consistent with the XRD (Fig. 5.18c) and Raman spectroscopy (Fig. 5.19c) confirming the presence of *h*BN and NiO, CuO, MoO_3 and $NiMoO_4$. The lower wear rate exhibited by NI-10BN may be attributed to the presence of Cu-modified *h*BN nanosheets (Cu-*h*BN) as well as the relatively higher hardness of NI-10BN compared to NI-10Ag. The

average thickness of the glaze layer formed on the worn surface of NI-10AgBN at 800 °C (Fig. 5.20e) is observed to be larger (25.19 μm) in comparison to the layers observed on NI-10BN (15.72 μm), NI-10Ag (11.25 μm) and NI (5.61 μm).

A decrease in the coefficient of friction of NI-10AgBN composite with temperature (Fig. 5.8) may be attributed to the presence of silver (Ag) in the worn region of NI-10AgBN at room temperature, 200 °C and 400 °C (Figs. 5.16a to c). Silver has been previously reported to offer lubrication from room temperature (RT) to 450 °C [25]. The existence of loose wear debris, ploughing, a discontinuous tribo-layer on the worn region of NI-10AgBN, and a discontinuous transfer layer on the worn scar of the counterpart Si_3N_4 ball, as illustrated in Figs. 5.16(b and c) and 5.17(b and c), may have allowed direct contact between the NI-10AgBN composite and the counterface Si_3N_4 ball, leading to an increase in material loss from room temperature (RT) to 400 °C (Fig. 5.9). However, the reduction in CoF and wear rate beyond 400 °C may be attributed to the formation of a glaze as well as a compacted tribo-layer on the worn region of NI-10AgBN at 800 °C (Figs. 5.16e and 5.20e), comprising *h*BN and lubricious oxides such as $Ag_2Mo_2O_7$, Ag_2MoO_4, $NiMoO_4$, NiO, CuO, and MoO_3, as evidenced by XRD and Raman spectra (Figs. 5.18d and 5.19d). Elemental maps of the contact region on NI-10AgBN (Fig. 5.16f) and its counterpart Si_3N_4 ball (Fig. 5.17f) along with EDS analysis (Fig. 5.20f) of the glaze layer formed on NI-10AgBN (Fig. 5.20e) at 800 °C have also revealed the presence of various elements such as Ni, Ag, Mo, O, Cu, B, and N, indicating the presence of *h*BN and the formation of Ag, Ni, Cu, and Mo-based oxides having inherent lubricious properties. It has been reported that Ag_2MoO_4 and $Ag_2Mo_2O_7$ possess superior lubrication properties at elevated temperatures, ascribed to their layered structure composed of Ag_2O and MoO_3 lamellae with a silver layer [136,139]. The combination of solid lubricants (Ag and Cu-*h*BN) appears to be effective in attaining a

lower coefficient of friction and wear rate over the entire temperature range used in the present investigation, as evident from Figs. 5.8 and 5.9.

The examination of the transfer layer formed on the worn tracks of the counterface Si_3N_4 ball after tribo-tests conducted at different temperatures provides valuable insights into the wear mechanism and the formation of an oxide layer on the worn surface, as demonstrated in Figs. 5.11(d and e), 5.13(d and e), 5.15(d and e), and 5.17(d and e). It has been observed that an increase in temperature from RT to 800 °C leads to an increased presence of transferred components on the counterface, as confirmed by the EDS analysis (Figs. 5.11f, 5.13f and 5.15f) and Elemental mapping (Fig. 5.17f) of worn Si_3N_4 balls at 800 °C. The presence of a transfer layer at elevated temperatures indicates the occurrence of adhesive wear in conjunction with oxidative and abrasive wear. The EDS analysis (Fig. 5.15f) of the transfer layer formed on the worn surface of Si_3N_4 at 800 °C (Fig. 5.15e) against NI-10BN composite reveals that the layer is composed of various elements such as Ni, Mo, O, Cu, B, and N, indicating the presence of *h*BN and the formation of Ni, Cu, and Mo-based oxides. These components are same as those found on the worn surface of NI-10BN composite, as confirmed by EDS-mapping (Figs. 5.14f and 5.20d), XRD (Fig. 5.18c), Raman spectroscopy (Fig. 5.19c). Similarly, the elemental maps of the transferred layer formed on the worn surface of Si_3N_4 at 800 °C (Fig. 5.17f) against NI-10AgBN composite also reveal the presence of Ni, Ag, Mo, O, Cu, B, and N elements, suggesting the existence of *h*BN and the formation of Ag, Ni, Cu, and Mo-based oxides. These elemental components correspond to those found on the worn surface of the NI-10AgBN composite, as evidenced by EDS-mapping (Figs. 5.16f and 5.20f), XRD (Fig. 5.18d), Raman spectroscopy (Fig. 5.19d). The presence of transfer layers of different thicknesses and containing different amounts of lubricious species on the worn surfaces of NI and

composites may explain their relative effectiveness in providing adequate lubrication at elevated temperatures.

In summary, the current study on the tribological performance of Ni_3Al-based composites incorporating the solid lubricants Ag and Cu-*h*BN either individually or in combination indicates that the addition of these lubricants is effective in decreasing both the coefficient of friction and the wear rate across a temperature range from room temperature to 800 °C. Ni_3Al has shown the highest coefficient of friction and wear rate, except for 200 °C and 400 °C, whereas Ni_3Al-10Ag has exhibited the highest wear rate. The coefficient of friction and wear rate for Ni_3Al-10Ag and Ni_3Al-10Cu-*h*BN have been observed to lie between Ni_3Al and Ni_3Al-5Ag-5Cu-*h*BN, with Ni_3Al-10Ag exhibiting marginally lower values. The Ni_3Al-5Ag-5Cu-*h*BN has been found to exhibit the lowest coefficient of friction and wear rate, which reveals that the addition of a combination of Ag and Cu-*h*BN is effective in reducing both the CoF and the wear rate from room temperature (RT) to 800 °C by aiding each other's lubricating capabilities.

5.3 Results and discussions: Synthesis and Tribological behaviour of Ni_3Al-WS_2/Ni_3Al-Cu-*h*BN/Ni_3Al-WS_2-Cu-*h*BN composites

5.3.1 Characterisation of Cu-doped *h*BN nanosheets

Figure 5.21 shows the TEM micrographs of Cu-doped *h*BN nanosheets (Cu-*h*BN). The *h*BN nanosheets are explicitly seen in low-resolution TEM images (Fig. 5.21a). The surface of *h*BN nanosheets exhibits a regular distribution of spherical to ellipsoidal darker features composed of copper oxide, as shown in Figs. 5.21(a-c). The ultrasound-assisted exfoliation has led to various structural defects and oxide sites on the surface of *h*BN nanosheets. These defects are thought to have acted as anchor regions for the growth of copper oxide during the chemical processing stage. In Cu-*h*BN, the size of copper oxide nanoparticles has been found to vary between 5 to 15 *nm* (Figs. 5.21b and c). Furthermore, a uniform distribution of Cu, O, B and N elements in Cu-*h*BN (Fig. 5.21d) has demonstrated the homogeneous dispersal of copper oxide nanoparticles on the surface of *h*BN nanosheets.

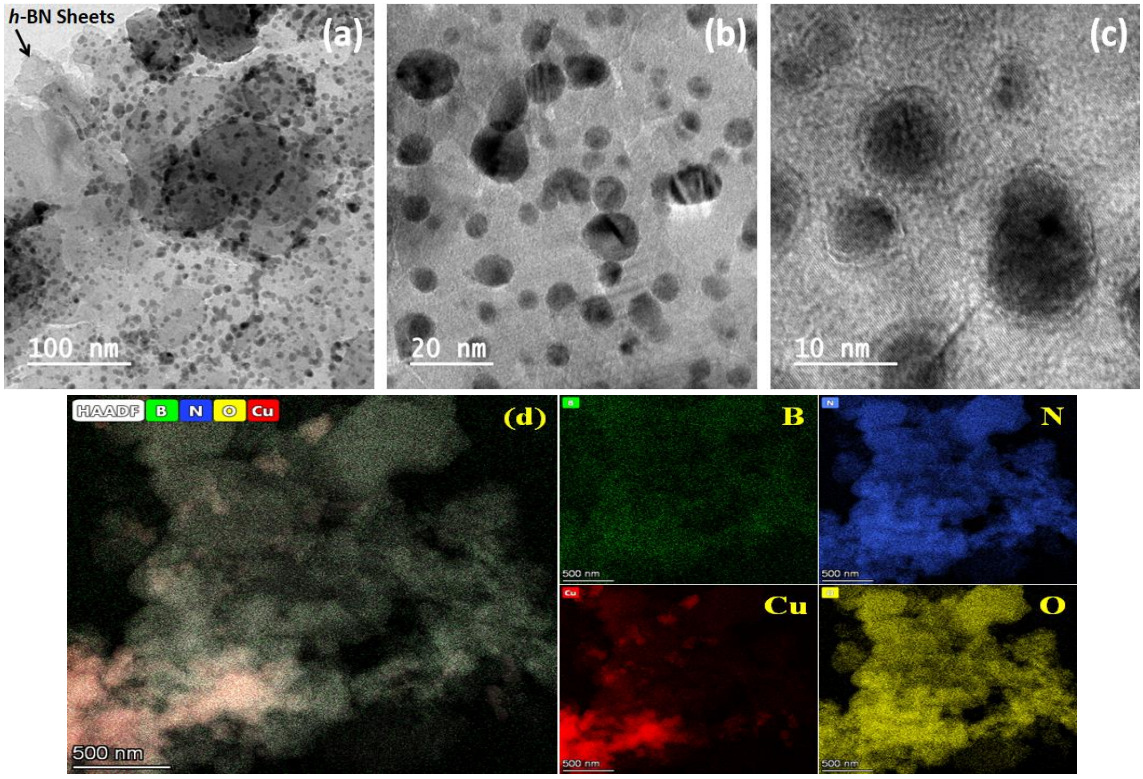

Fig. 5.21: TEM images of (a-c) Cu-*h*BN at different magnifications and (d) area elemental mapping of Cu-*h*BN.

Figures 5.22 and 5.23 show the XRD and XPS spectra of copper-doped *h*BN (Cu-*h*BN) powders. XRD and X-ray photoelectron spectroscopy (XPS) have been performed to study the chemical properties of the elements present, namely B, N, Cu and O in Cu-doped *h*BN powders. The X-ray diffraction pattern of Cu-*h*BN powders (Fig. 5.22) shows intense peaks corresponding to *h*BN (ICSD Ref. 01-073-2095), CuO (ICSD Ref. 01-089-2531), and Cu_2O (ICSD Ref. 00-035-1091), respectively. The existence of $Cu(OH)_2$ in Cu-*h*BN was validated by the diffraction peak at 2θ of 16.5°. Fig. 5.23(a) shows the full XPS spectra of the Cu-*h*BN powder, whereas the detailed spectra corresponding to B 1s, N 1s, C 1s, Cu 2P and O 1s are shown in Figs. 5.23(b-f), respectively. The XPS spectra of the B 1s and N 1s in Figs. 5.23(b and c) exhibit peaks at 190.45 eV and 397.9 eV, respectively, indicating the presence of *h*BN. The appearance of a peak at 284.6 eV for carbon in Fig. 5.23(d) may be due to the carbon grid used during processing to prepare the sample for XPS. The Cu 2p peak, as shown in Fig. 5.23(e), comprises two doublets and two shake-up satellite peaks, suggesting binary oxides. The Cu $2p_{3/2}$ and Cu $2p_{1/2}$ peaks at 933.03 and 952.9 eV, respectively, indicate Cu^{+}-based Cu_2O, while the more intense peaks at higher binding energies (935.0 and 954.8 eV correspond to Cu $2p_{3/2}$ and Cu $2p_{1/2}$) are attributed to Cu^{2+}-based CuO [142]. CuO was identified as the predominant oxide, comprising 57%, using XPS-based surface analysis. Additionally, the existence of two shake-up satellite peaks at 942.36 and 962.6 eV indicates the presence of an incomplete Cu 3d9 shell, verifying the Cu^{2+} phase as CuO [143].

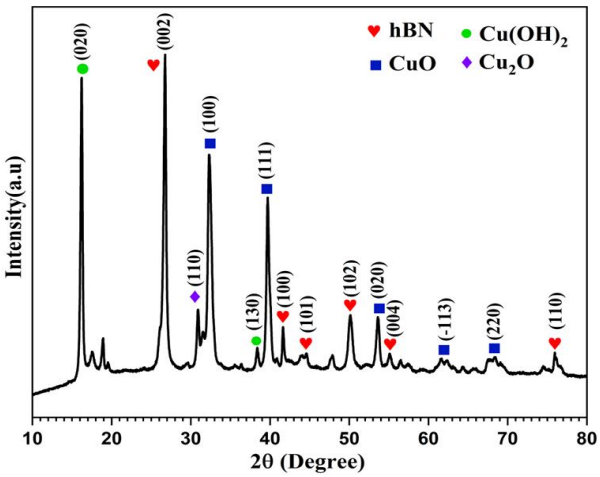

Fig. 5.22: XRD pattern of Cu doped *h*BN nanosheets.

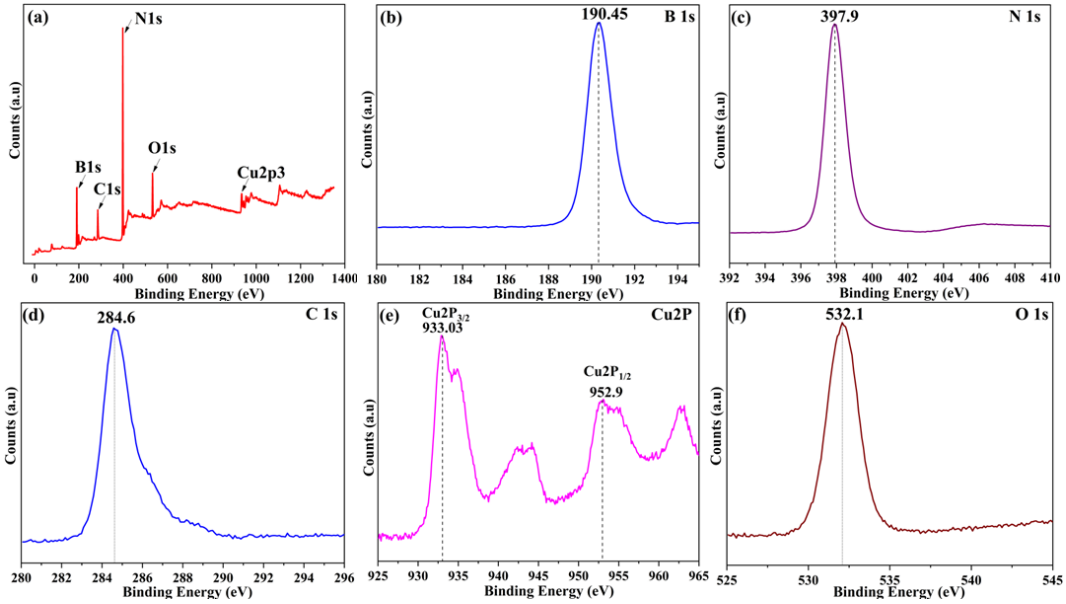

Fig. 5.23: XPS spectra of Cu-doped *h*BN powders showing full scan survey (a) and corresponding de-convoluted peaks in the high-resolution spectra for (b) B 1s, (c) N 1s (d) C 1s (e) Cu 2P and (f) O 1s.

5.3.2 Characterisation of Ni_3Al-based composites

Table 5.2 presents the sample notation, composition, actual density, relative density and hardness of composites. Fig. 5.24 depicts FESEM micrographs of mechanically alloyed powders along with elemental mapping of NAWB. The elemental maps (Fig. 5.24e) of NAWB powder has confirmed the presence of constituent elements. XRD patterns of

mechanically alloyed powders as well as the composites, i.e., NA, NAW, NAB and NAWB are illustrated in Fig. 5.25. The formation of Ni_3Al intermetallic compound has been confirmed by the XRD patterns of the mechanically alloyed powders shown in Fig. 5.25(a). Further, the XRD patterns also revealed the presence of WS_2 (ICSD Ref. 00-008-0237), CuO (ICSD Ref. 01-089-5898), *h*BN (ICSD Ref. 01-085-1068), Mo (ICSD Ref. 01-089-5156) and Ni_3Al (ICSD Ref. 03-065-430) in mechanically alloyed powders as depicted in Fig. 5.25(a). The diffraction patterns of sintered composites presented in Fig. 5.25(b) also exhibit intense peaks corresponding to Ni_3Al, Mo, CuO, WS_2 and *h*BN in their diffraction patterns, establishing that no oxidation or disintegration occurred during the process of vacuum hot press sintering.

Table 5.2: Sample notation, composition, density and micro-hardness.

Sample Notation	Composite	Actual density (g/cm^3)	Relative density (%)	Microhardness ($HV_{0.2}$)
NA	100wt.% Ni_3Al	8.372	99.46	355 ± 5
NAW	90wt.% Ni_3Al-10wt.% WS_2	8.105	97.42	365 ± 6
NAB	90wt.% Ni_3Al-10wt.% Cu-*h*BN	6.990	89.89	335 ± 5
NAWB	90wt.% Ni_3Al-5wt.% WS_2-5wt.% Cu-*h*BN	7.734	94.31	358 ± 4

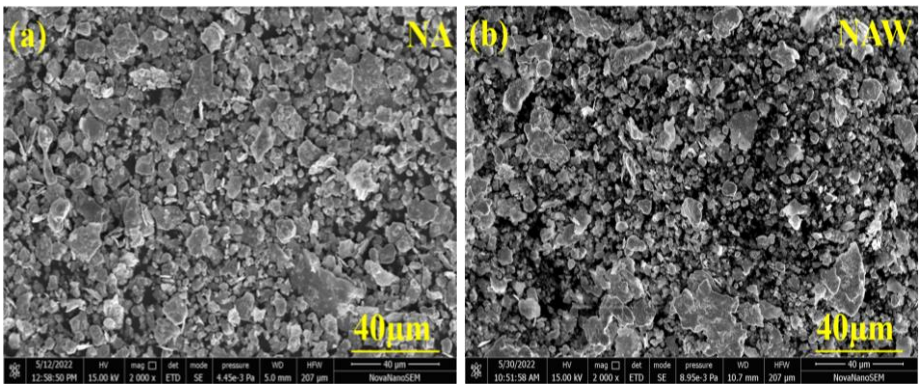

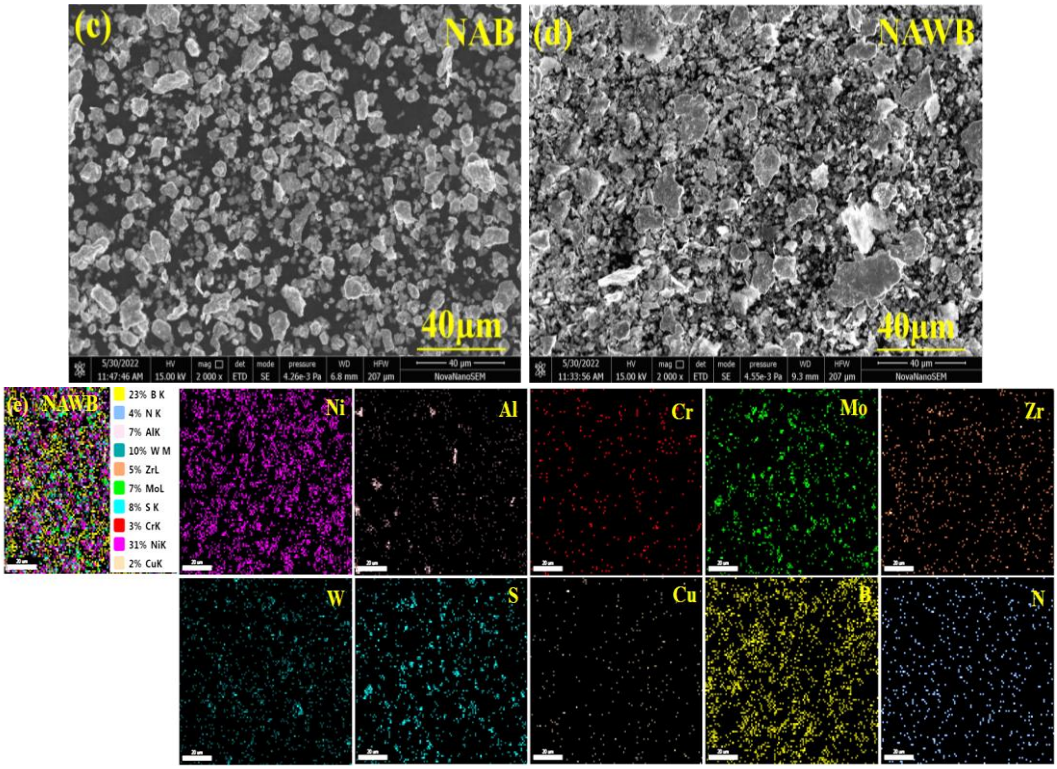

Fig. 5.24: Microscopic images of mechanically alloyed powders: (a) NA, (b) NAW, (c) NAB, and (d) NAWB and (e) elemental mapping of NAWB.

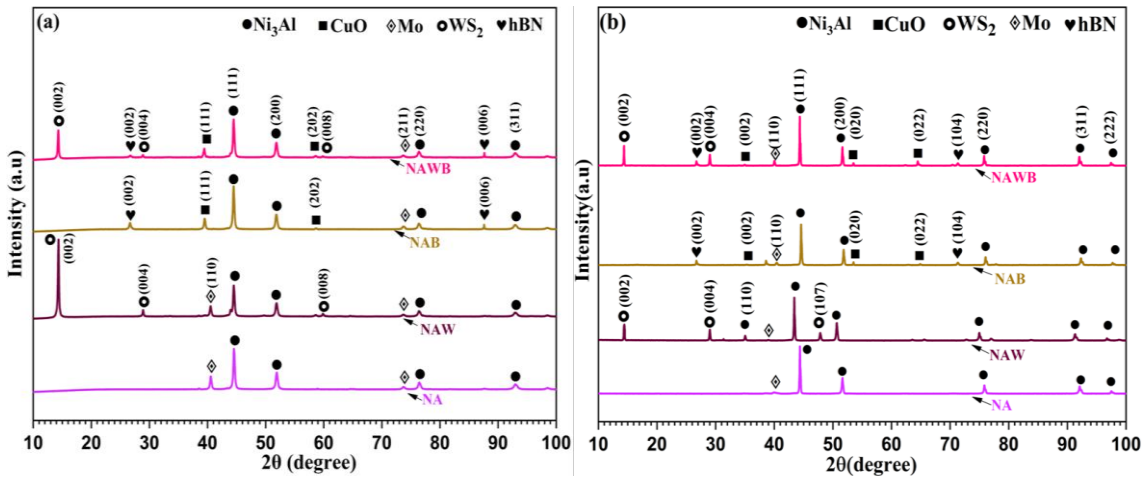

Fig. 5.25: HR-XRD patterns for NA, NAW, NAB, and NAWB (a) mechanically alloyed powders and (b) sintered composite.

Figure 5.26 illustrates the FESEM micrographs of the NA, NAW, NAB and NAWB composites, along with the elemental mapping of NAWB. Figure 5.26(a) shows the microstructure of NA, and the formation of Ni_3Al has been confirmed by the XRD analysis (Fig. 5.25b). Figs. 5.26(b-d) show that the composites have a compact microstructure, in

which the constituent elements (i.e., WS_2 in NAW (Fig. 5.26b), Cu-*h*BN in NAB (Fig. 5.26c), and both WS_2 and Cu-*h*BN in NAWB (Fig. 5.26d) are almost uniformly distributed, as shown by the arrows in the corresponding micrographs. The presence of constituents has been confirmed by the elemental mapping of NAWB composite, as depicted in Fig. 5.26(e). The incorporation of WS_2 enhances the micro-hardness of Ni_3Al from 355 ± 5 HV to 365 ± 6 HV, while Cu-*h*BN reduces it to 335 ± 5 HV. However, incorporating both WS_2 and Cu-*h*BN leads to an increase in the hardness of Ni_3Al to 358 ± 4 HV.

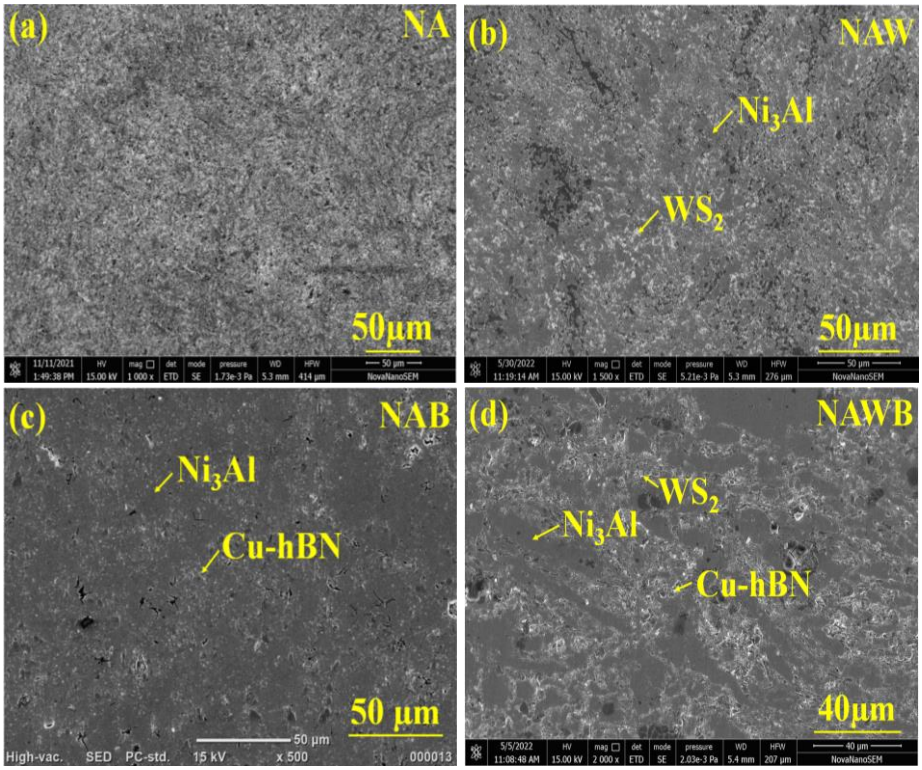

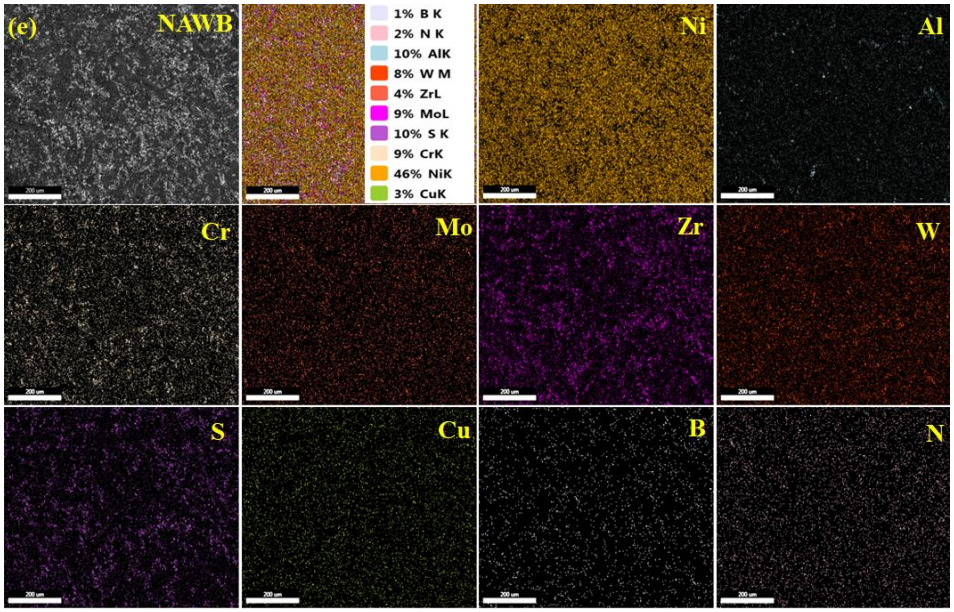

Fig. 5.26: FESEM micrographs showing the microstructure of (a) NA, (b) NAW, (c) NAB and (d) NAWB and (e) elemental mapping of NAWB composite.

5.3.3 Tribological behaviour of Ni_3Al-WS_2/Ni_3Al-Cu-*h*BN/Ni_3Al-WS_2-Cu-*h*BN

The time-dependent friction profiles for NA, NAW, NAB, and NAWB composites under a constant normal load (10 N) and fixed sliding speed (0.2 m/s) at RT, 200 °C, 400 °C, 600 °C and 800 °C are shown in Figs. 5.27(a-e). NA exhibits a consistently higher coefficient of friction (CoF) than other composites at all temperatures. At RT (Fig. 5.27a), the CoF for NA reaches a stable value after 1000 s and stays constant throughout the entire duration of the test thereafter, while the CoF for the NAW, NAB, and NAWB stabilises after 300 s, 200 s, and 400 s, respectively, with minor fluctuations in amplitude. At 200 °C (Fig. 5.27b), the coefficient of friction for NA appears to stabilise after 1300 s, whereas for the NAW, NAB, and NAWB, stabilisation seems to occur after an initial run-in duration of 800 s, 1400 s and 1500 s, respectively. The CoF for NA, NAW, and NAWB remains stable throughout the test without any discernible run-in period at 400 °C (Fig. 5.27c), while the CoF for NAB stabilises after 700 s with relatively larger fluctuations in amplitude as compared to RT. At 600 °C (Fig. 5.27d), the CoF for NA and NAW composites is steady for the entire duration, whereas the CoF for NAB and NAWB stabilises after 1600 s, whereas at 800 °C (Fig.

5.27e), the CoF for NA, NAW, and NAWB composites is steady for the entire duration, whereas the CoF for NAB stabilises after 1000 s. Both NAW and NAB have been observed to show a relatively larger fluctuation in amplitude than NA and NAWB.

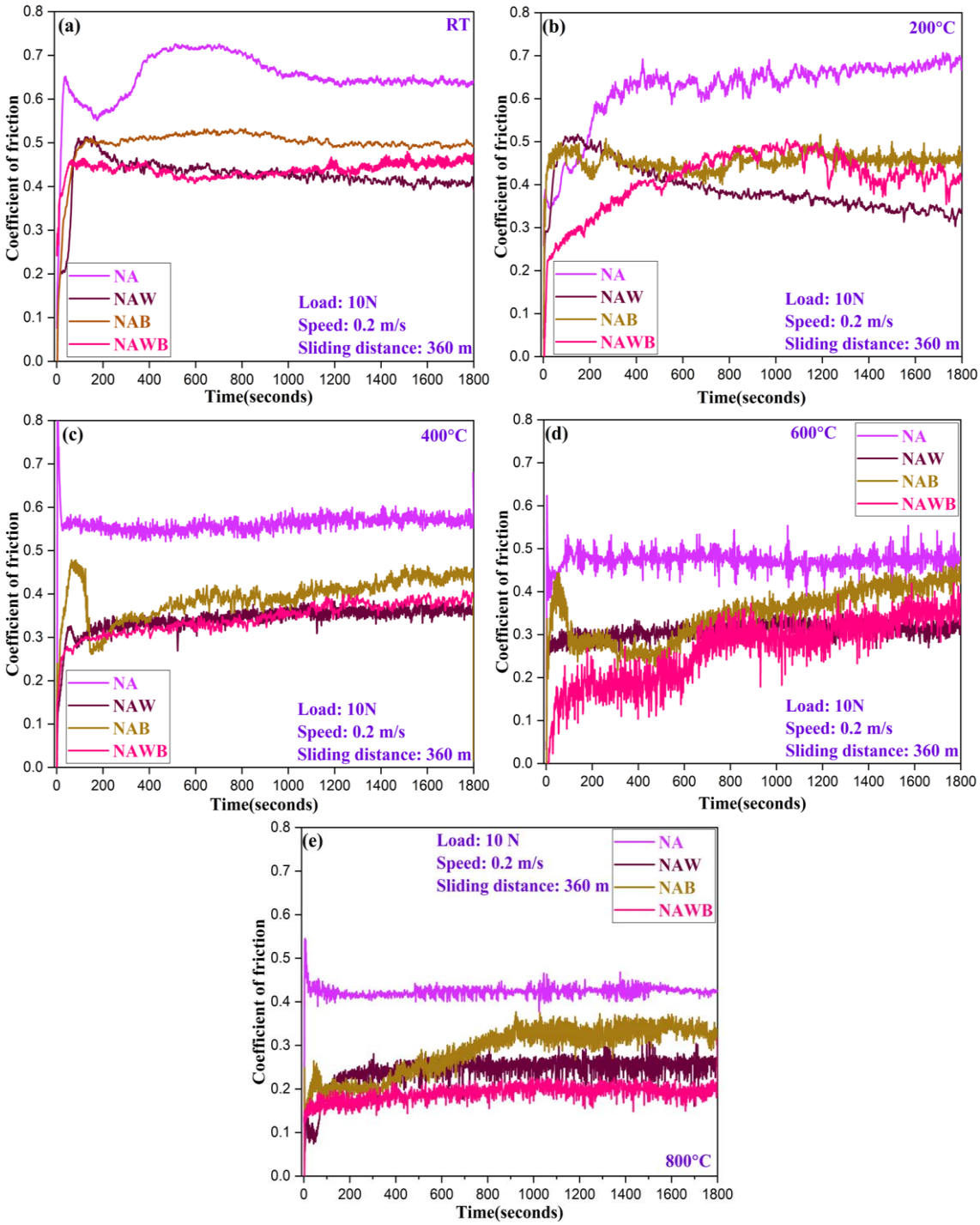

Fig. 5.27: Time-dependent friction profiles for NA, NAW, NAB, and NAWB at (a) RT, (b) 200 °C, (c) 400 °C, (d) 600 °C, and (e) 800 °C.

The variation of the average coefficient of friction with temperature for NA, NAW, NAB, and NAWB composites presented in Fig. 5.28 shows a continuous decrease in CoF with increasing temperature for all the materials. The CoF for NA and NAW has been found to decrease from 0.65 to 0.42 and 0.42 to 0.24, respectively, with increasing temperature from RT to 800 °C. Similarly, the CoF for NAB and NAWB has been found to reduce from 0.48 to 0.28 and 0.44 to 0.18, respectively, as the temperature changes from RT to 800 °C. One may also observe a significant reduction in the average CoF by adding either WS_2 or Cu-*h*BN and their combination in Ni_3Al at all temperatures. However, the incorporation of WS_2 appears to have a greater effect in reducing the CoF than the addition of Cu-*h*BN, as seen in Fig. 5.28. NAWB composite containing equal amounts of WS_2 and Cu-*h*BN has shown the lowest CoF at temperatures above 400°C, indicating the existence of a synergistic effect between the two lubricating materials, whereas it has shown a marginally higher CoF in comparison to NAW at temperatures below 400°C.

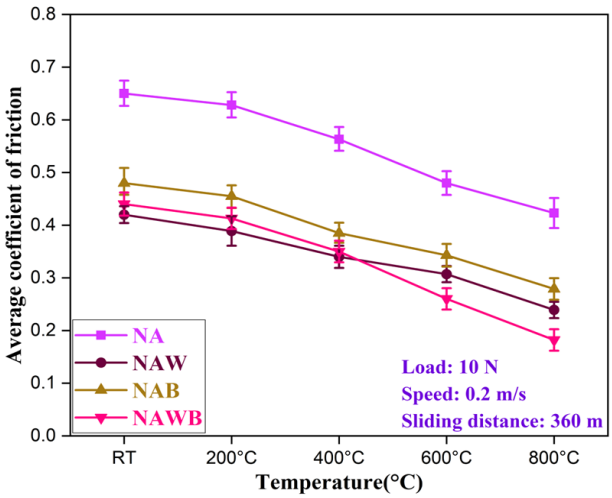

Fig. 5.28: Temperature-dependent graphical plots of coefficient of friction for NA, NAW, NAB, and NAWB.

Figure 5.29 shows the variation of wear rate with temperature for NA, NAW, NAB, and NAWB. All specimens exhibit a similar trend of variation in wear rate with increasing temperature, i.e., the wear rate increases as the temperature is raised from RT to 400 °C

which is followed by a decrease at 600 °C and 800 °C. The wear rates of NA, NAW, NAB, and NAWB have been observed to increase from 3.52 to 5.95 x 10^{-5} mm^3/Nm, 1.58 to 2.52 x 10^{-5} mm^3/Nm, 2.285 to 3.1 x 10^{-5} mm^3/Nm, and 2.12 to 2.61 x 10^{-5} mm^3/Nm, respectively, as the temperature is increased from RT to 400 °C, followed by a decrease to 2.46 x 10^{-5} mm^3/Nm, 1.06 x 10^{-5} mm^3/Nm, 1.95 x 10^{-5} mm^3/Nm, and 0.875 x 10^{-5} mm^3/Nm, respectively, beyond 400 °C. One may also notice that NAW and NAWB composites have relatively lower wear rates in comparison to NA and NAB at all temperatures. The addition of WS_2 and Cu-*h*BN into Ni_3Al has been found to be effective in reducing wear beyond 400 °C in comparison to NAW, as depicted in Fig. 5.29.

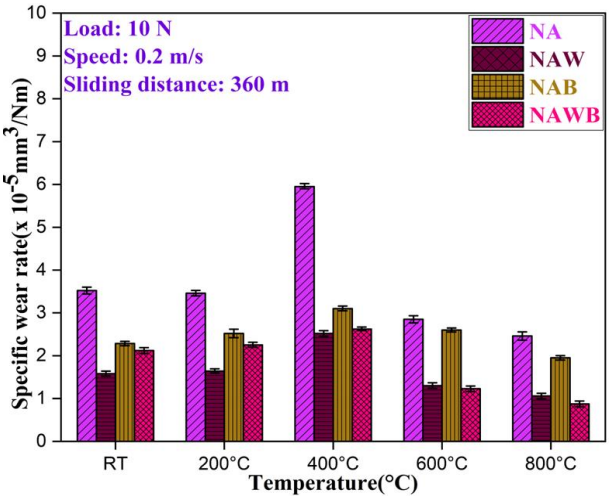

Fig. 5.29: Temperature-dependent wear plots for NA, NAW, NAB, and NAWB.

5.3.4 Analysis of Worn Surfaces

Figures 5.30(a-g) and 5.31(a-f) present microscopic images of worn tracks developed on NA and Si_3N_4 balls resulting from tribo-tests from RT to 800 °C. The worn track of NA at RT (Fig. 5.30a) shows evidence of dispersed wear debris and patches of a transfer film, while at 200 °C (Fig. 5.30b), it exhibits the presence of wear debris and ploughing. At 400 °C (Fig. 5.30c), it exhibits the existence of wear debris, ploughing, and some delamination. The worn scar of NA at 600 °C (Fig. 5.30d) reveals a compact tribo-film and wear debris at some regions, whereas at 800 °C (Fig. 5.30f), it exhibits a flat and smooth morphology

of the worn surface. The smooth tribo-film at 600 °C and 800 °C primarily comprises Ni and Mo oxides, which extend over a significant area of the worn surface, based on the EDS analysis and elemental maps presented in Figs. 5.30(e and g). The formation of a compact and continuous tribo-film at 600 °C and 800 °C (Figs. 5.30d and f) may have supported reducing friction and wear compared to RT, 200 °C and 400 °C (Figs. 5.30a to c). The EDS of the worn scar at 800 °C (Fig. 5.31f) confirms that tribo-film was transferred to the Si_3N_4 ball, as seen in the SEM-EDS analysis of the worn track of the corresponding Si_3N_4 ball (Fig. 5.31e). It is noticeable that the transferred tribo-film appears smoother and more compact at 600 °C (Fig. 5.31d) and 800 °C (Fig. 5.31e) compared to RT, 200 °C and 400 °C (Figs. 5.31a to c).

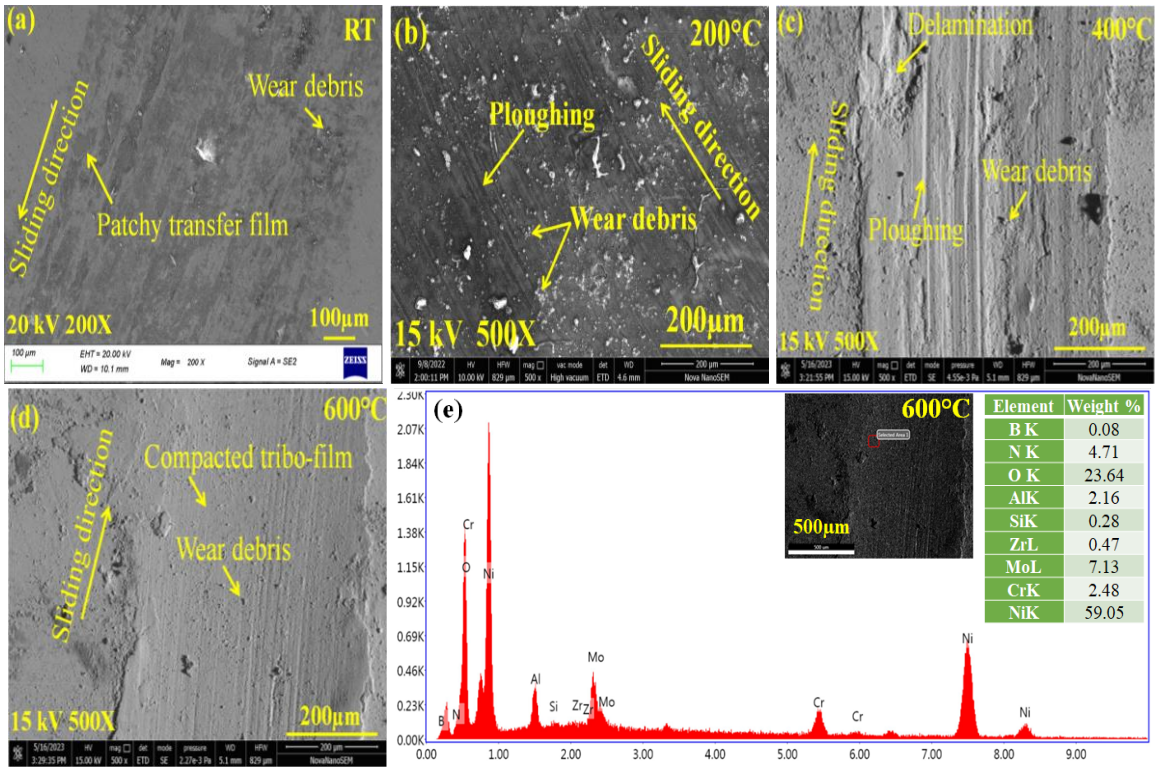

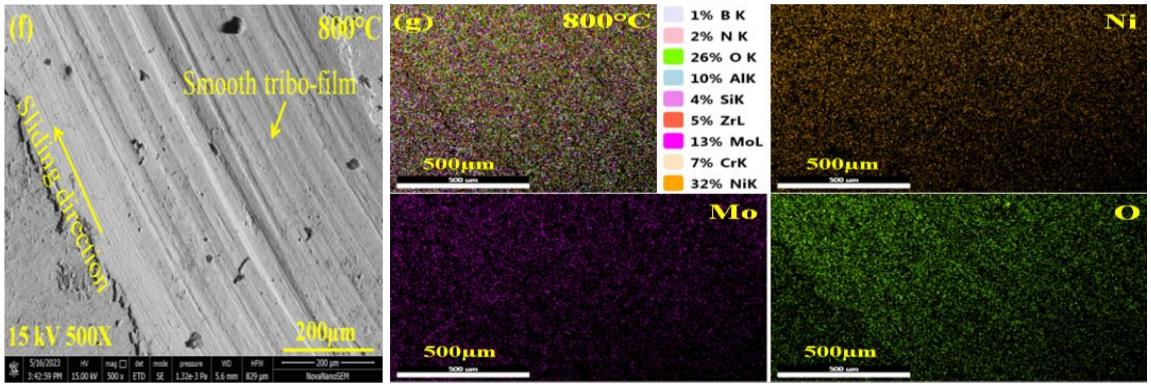

Fig. 5.30: FESEM images of the worn surface of NA: (a) RT, (b) 200 °C, (c) 400 °C, (d) 600 °C, (f) 800 °C, and (e and g) EDS and elemental mapping of worn surface of NA at 600 °C and 800 °C.

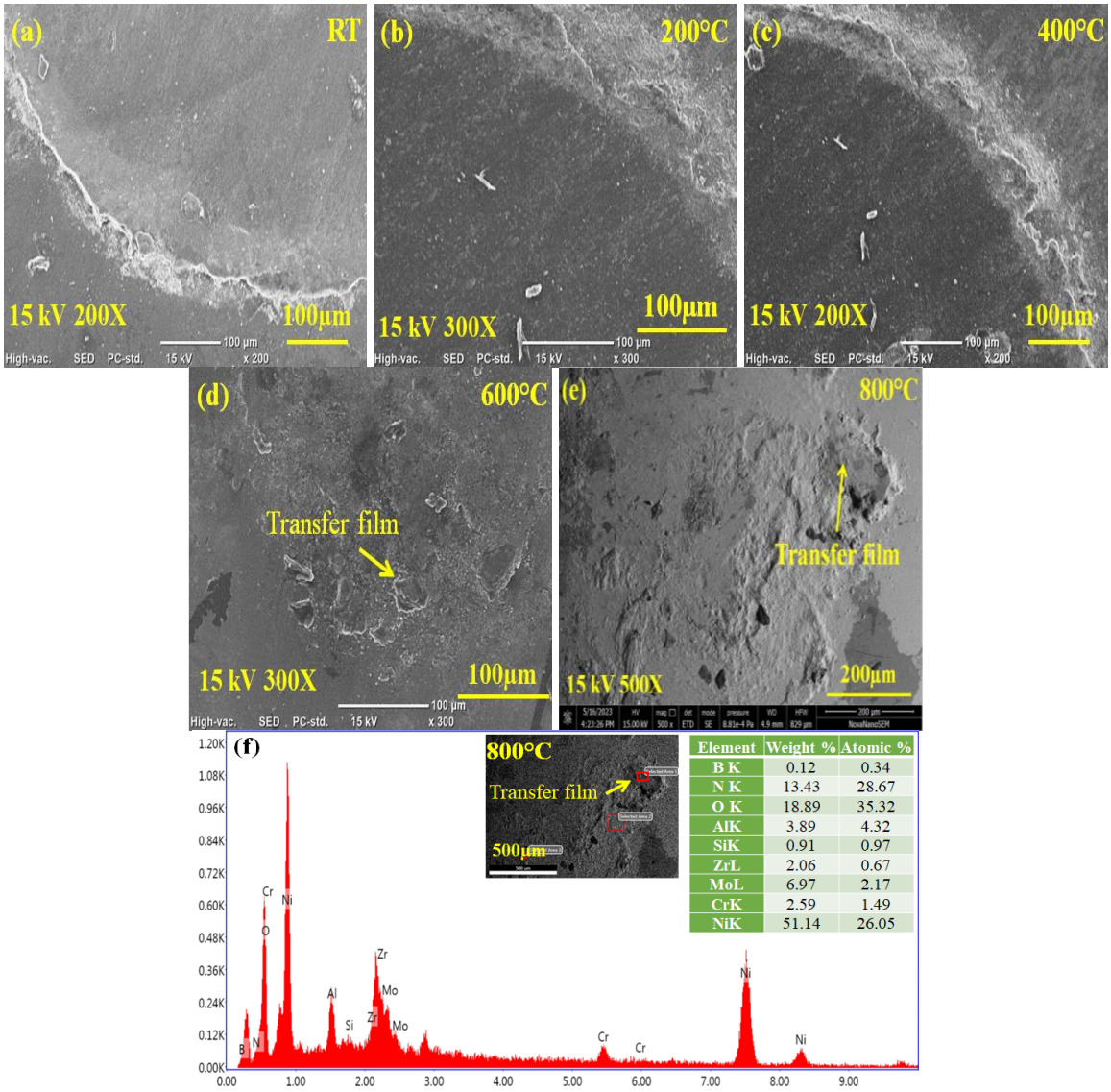

Fig. 5.31: FESEM images of the worn surface of counterface Si_3N_4 ball: (a) RT, (b) 200 °C, (c) 400 °C, (d) 600 °C, (e) 800 °C, and (f) EDS analysis of transfer film on the ball at 800 °C.

The FESEM micrographs depicted in Figs. 5.32(a-g) and 5.33(a-f) showcase the worn track of the NAW composite and the opposing Si_3N_4 balls at various temperatures ranging from RT to 800 °C. At room temperature (Fig. 5.32a), the worn track displays evidence of a patchy transfer film and a significant amount of dispersed wear debris, whereas at 200 °C (Fig. 5.32b), the worn track displays wear marks and some delamination. At 400 °C (Fig. 5.32c), the worn track exhibits the existence of delaminated regions and microcracks. The worn surface at 600 °C (Fig. 5.32d) displays a uniform and compacted tribo-film with minimal wear debris and no grooves or ploughing, indicating oxidation as the primary wear mechanism, whereas at 800 °C (Fig. 5.32e), the worn area exposes a continuous and compacted tribo-film. The EDS analysis of a spectrum (Figs. 5.32f and g) marked on the worn region of the composite at 600 °C and 800 °C (Figs. 5.32d and e) has confirmed the existence of oxides. The EDS analysis of a selected spectrum on the counter Si_3N_4 ball at 800 °C, as marked in Fig. 5.33(f), has confirmed that material from the NAW composite has been transferred to the counter Si_3N_4 ball (Figs. 5.33a to e). The transferred material has formed a tribo-film over the worn scar of the ball, but the area covered and the level of compaction of the tribo-film are different at lower and moderate temperatures compared to elevated temperatures.

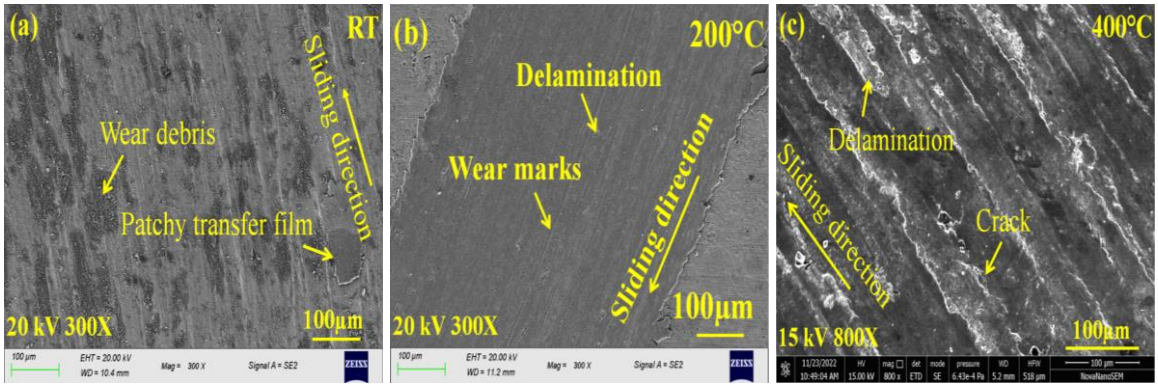

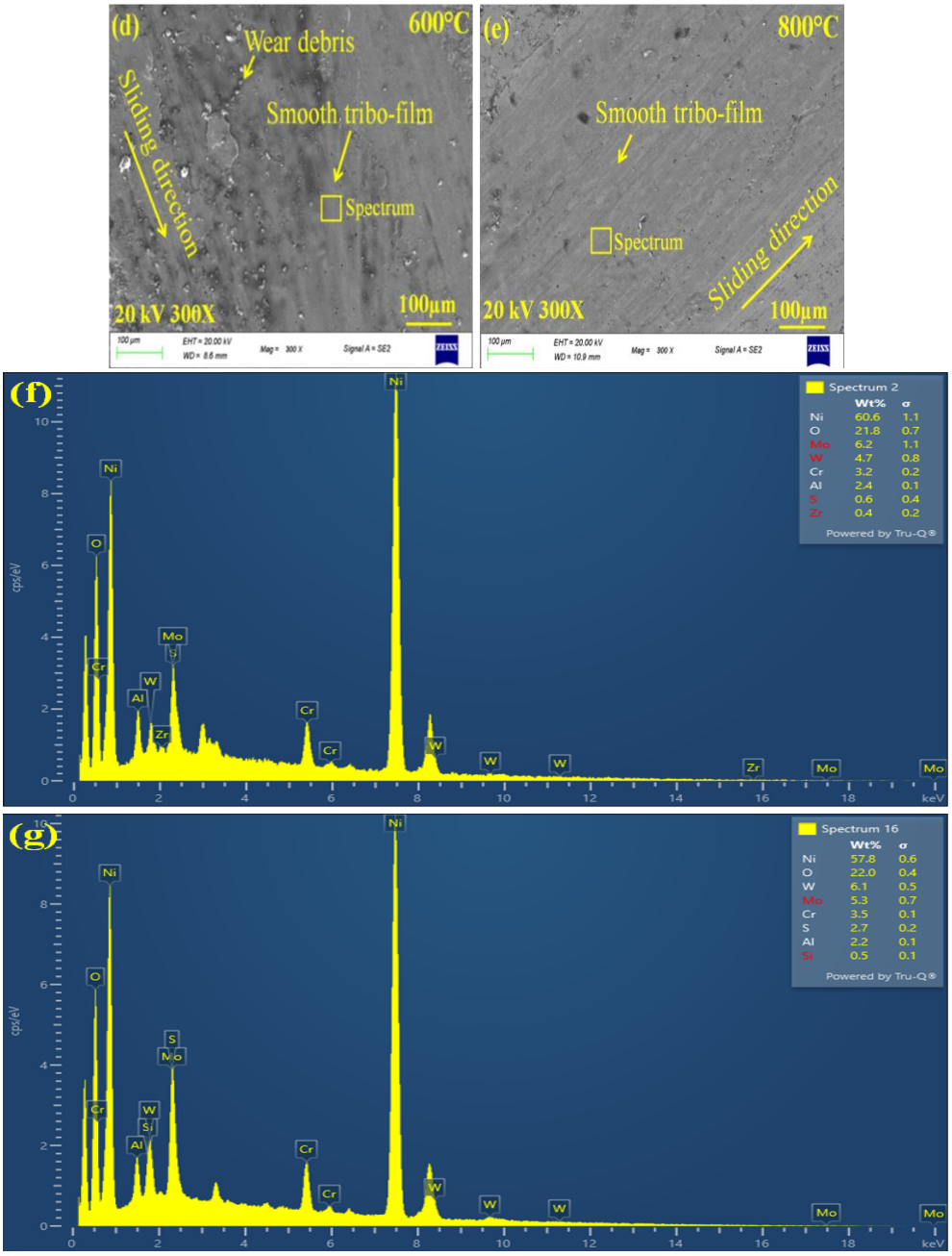

Fig. 5.32: FESEM images of the worn surface of NAW: (a) RT, (b) 200 °C, (c) 400 °C, (d) 600 °C, (e) 800 °C, and (f and g) EDS analysis of worn surface of NAW at 600 °C and 800 °C.

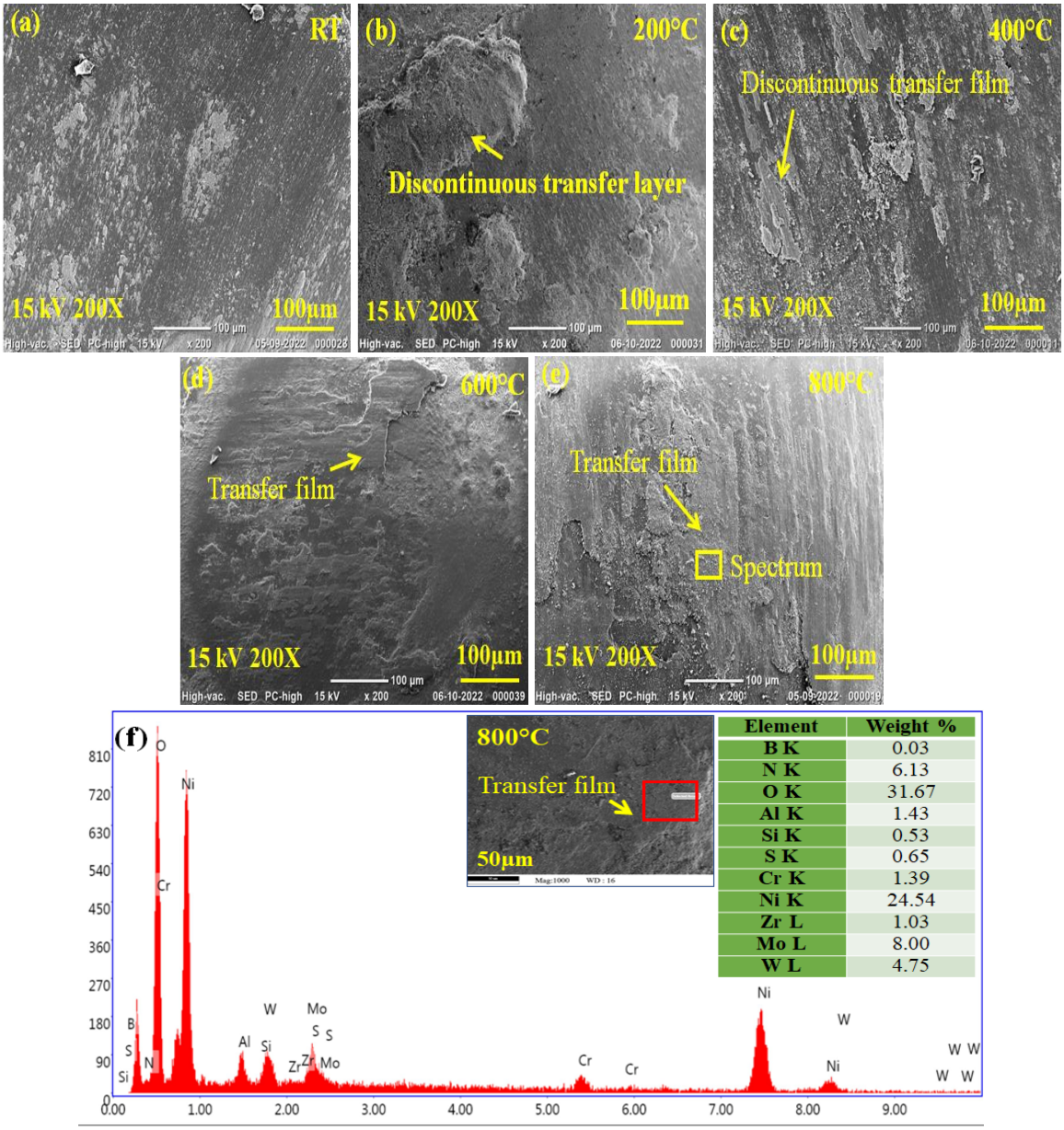

Fig. 5.33: FESEM images of the worn surface of counterface Si_3N_4 ball: (a) RT, (b) 200 °C, (c) 400 °C, (d) 600 °C, (e) 800 °C, and (f) EDS analysis of transfer film on the ball at 800 °C.

The FESEM micrographs (Figs. 5.34a-e and 5.35a-e) and EDS analysis (Figs. 5.34f-h and 5.35f) illustrate the morphology and elemental distribution of worn NAB composite and Si_3N_4 ball surfaces at different temperatures. The wear scar at RT and 200 °C (Figs. 5.34a and b) exposes a scattered transfer film and wear debris, while at 400 °C (Fig. 5.34c), the worn area exhibits the existence of wear debris, delaminated regions, cracks, and

compacted tribo-film. At 600 °C (Fig. 5.34d), the worn surface exhibits a compact tribo-film and wear debris. At 800 °C (Fig. 5.34e), the tribo-film seems to be smooth, compact, and consistent and covers a wider area of wear without any trace of abrasion or ploughing, suggesting an oxidative wear mechanism. EDS examination (Figs. 5.34f and g) and elemental mapping (Fig. 5.34h) of the worn region of NAB composite at 600 °C and 800 °C (Figs. 5.34d and e) reveal the abundance of characteristic elements, namely Ni, O, Mo, Cu, B, N, Al, Cr, Si and Zr, whereas the EDS scan (Fig. 5.35f) of the transfer film indicated by the arrow in Fig. 5.35(e) confirms that the material has been transferred from the NAB composite to the counter Si_3N_4 ball, forming a tribo-film on the counter Si_3N_4 ball surface with a varying degree of area coverage and level of compaction as evident from Figs. 5.35(a, b, c, d and e).

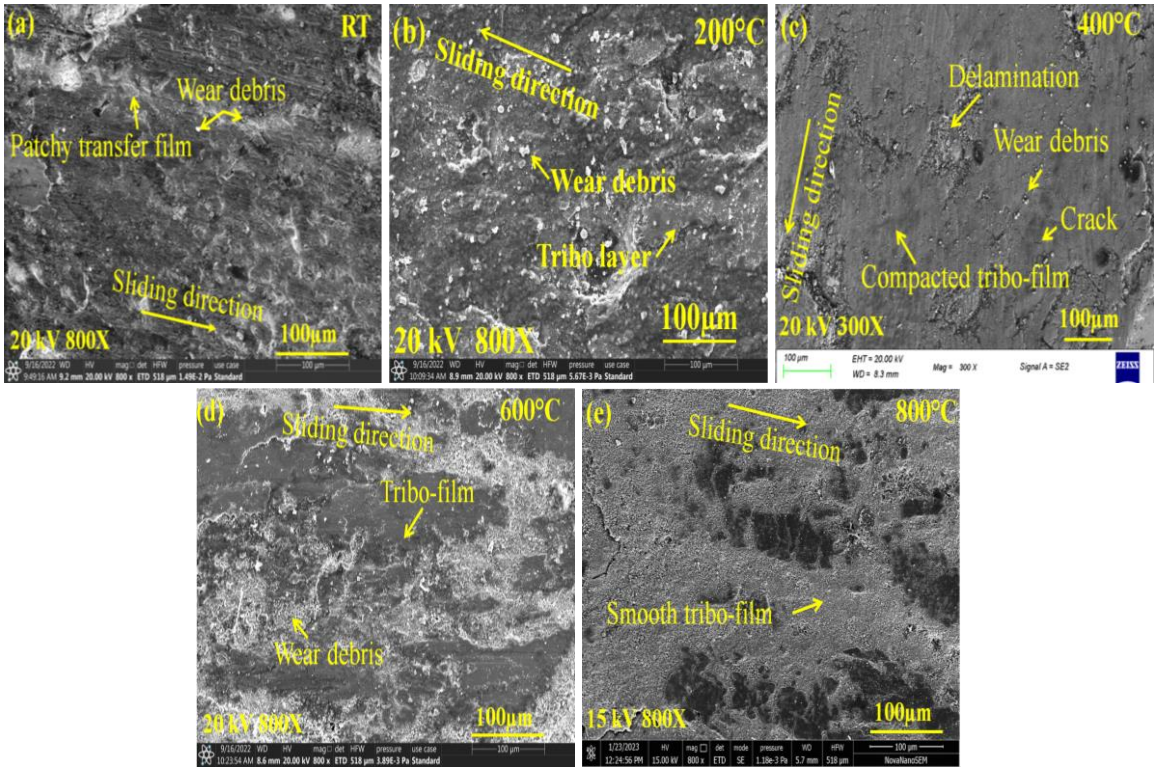

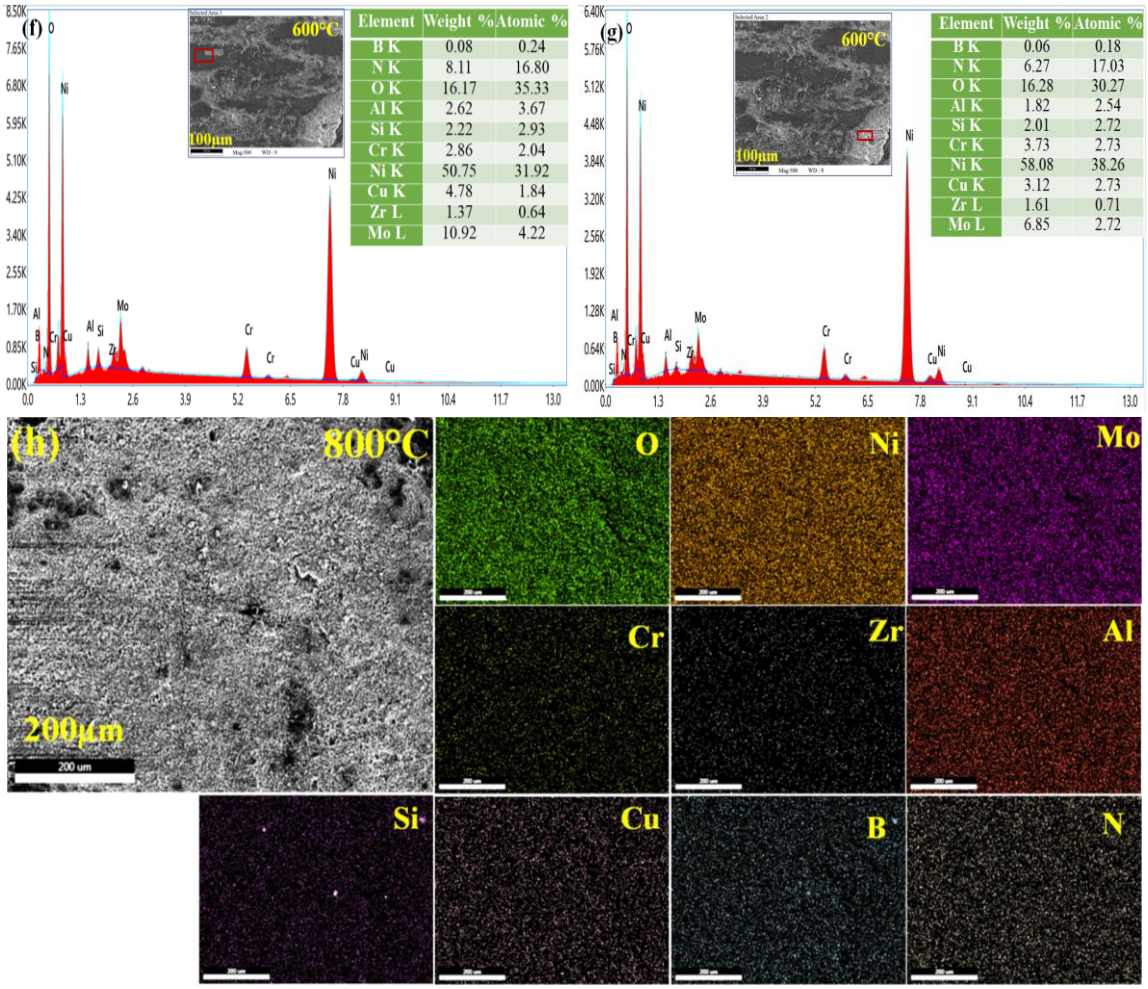

Fig. 5.34: FESEM images of the worn scar of NAB composite at (a) RT, (b) 200 °C, (c) 400 °C, (d) 600 °C, (e) 800 °C, and (f, g and h) EDS and elemental maps of worn track at 600 °C and 800 °C.

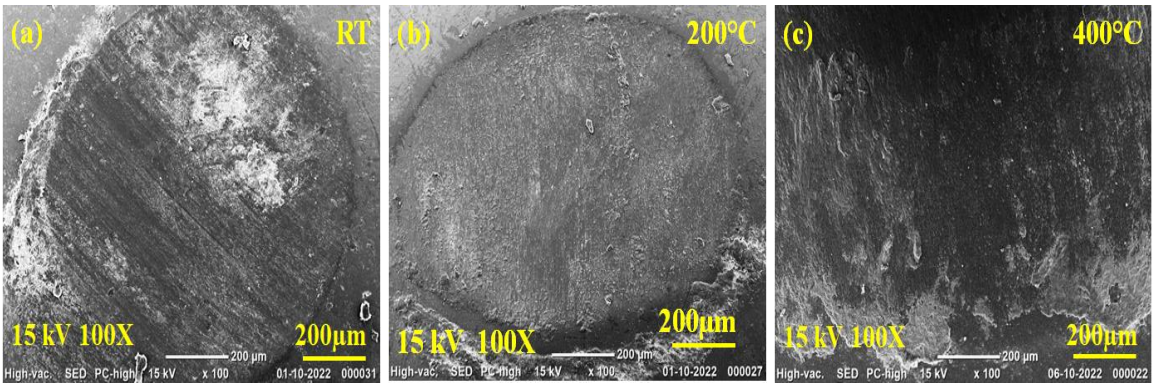

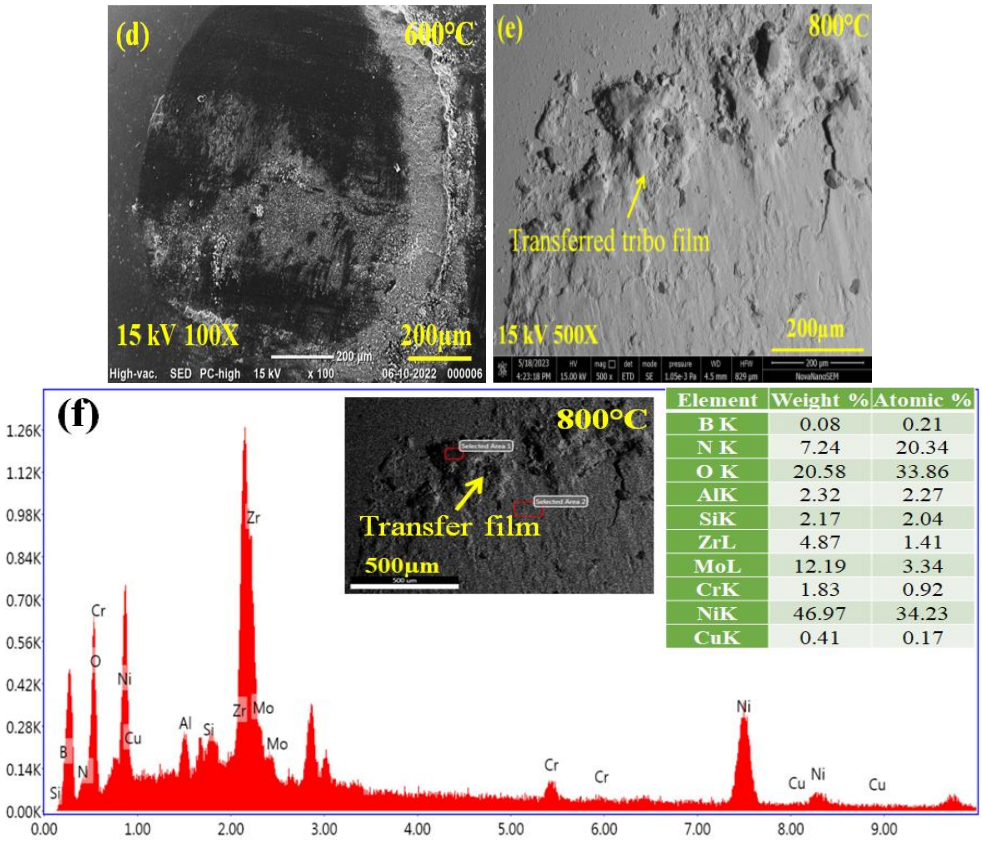

Fig. 5.35: FESEM images of the worn scar of Si_3N_4 ball at (a) RT, (b) 200 °C, (c) 400 °C, (d) 600 °C, (e) 800 °C, and (f) EDS analysis of transfer film on worn Si_3N_4 ball (counterface) at 800 °C.

The FESEM micrographs and EDS spectra of worn NAWB composite and Si_3N_4 ball surfaces at room temperature (RT), 200 °C, 400 °C, 600 °C, and 800 °C are illustrated in Figs. 5.36(a-g) and 5.37(a-f), respectively. The worn surface of the NAWB composite shows sliding marks, wear particles, delamination, and patchy transfer film at RT (Fig. 5.36a), whereas at 200 °C (Fig. 5.36b) and 400 °C (Fig. 5.36c), it displays wear particles, ploughing, delamination, and compact tribo-film. The contact surface at 600 °C (Fig. 5.36d) reveals the existence of wear debris and a smooth tribo-film, while at 800 °C (Fig. 5.36e), the worn surface displays a compact and continuous glaze layer along with a smooth tribo-film comprising elements such as O, Ni, Mo, W, S, Cu, B, and N, as supported by the EDS examination of worn scar at 600 °C (Fig. 5.36f) and elemental maps of the worn scar at 800

°C (Fig. 5.36g). Elemental mapping (Fig. 5.37f) of the worn scar of counterface Si_3N_4 ball at 800 °C (Fig. 5.37e) confirms the transfer of NAWB composite material to the counterface Si_3N_4 ball, with elements such as O, Ni, Si, Mo, W, S, Cu, B, and N present in a transfer film of varying coverage and compaction, as depicted in Figs. 5.37(a-e). It is also worth noting that the worn surface of the NAWB composite and Si_3N_4 ball is predominantly covered by elements like O, Ni, Mo, W, S, Cu, B, and N.

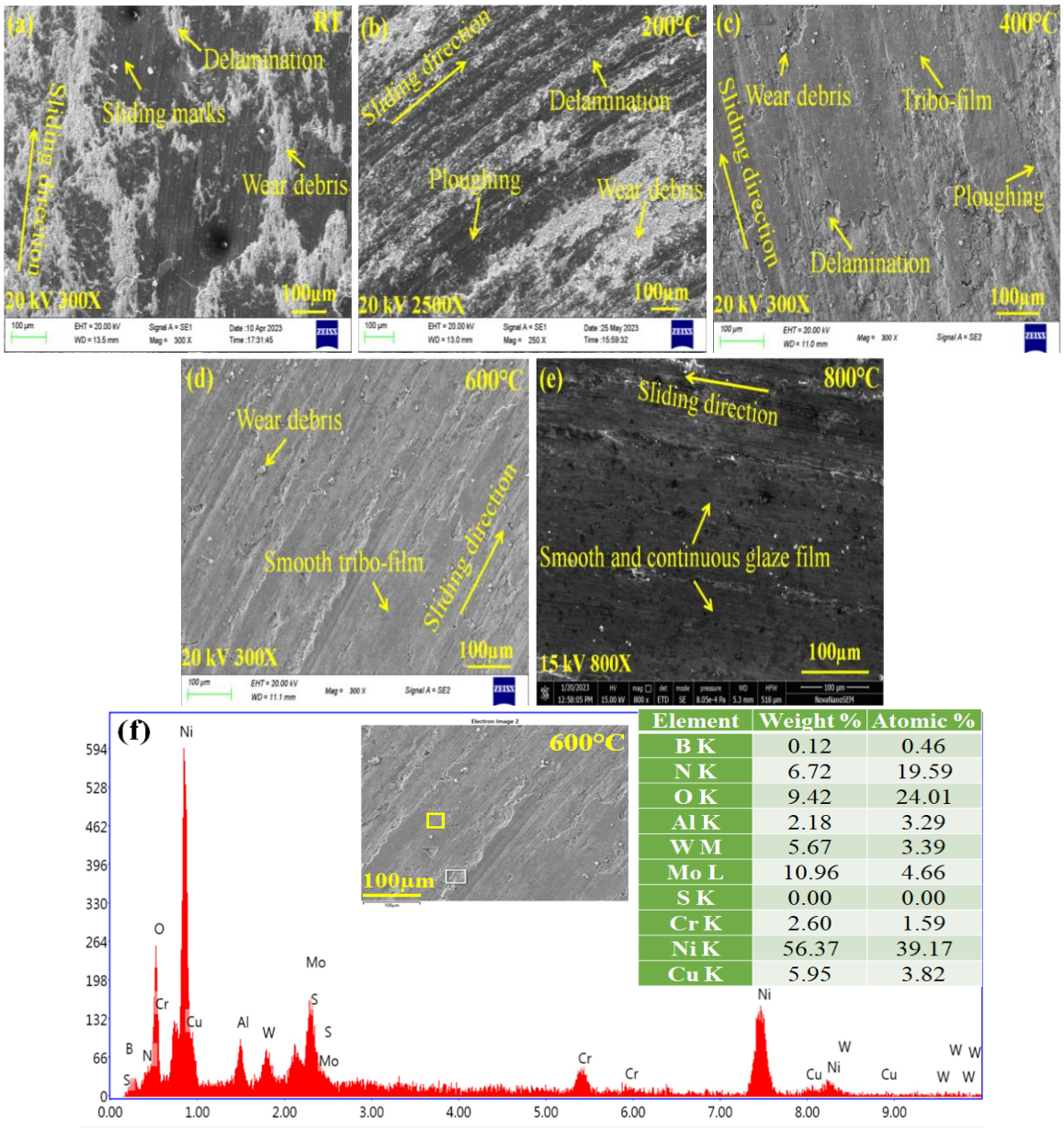

Element	Weight %	Atomic %
B K	0.12	0.46
N K	6.72	19.59
O K	9.42	24.01
Al K	2.18	3.29
W M	5.67	3.39
Mo L	10.96	4.66
S K	0.00	0.00
Cr K	2.60	1.59
Ni K	56.37	39.17
Cu K	5.95	3.82

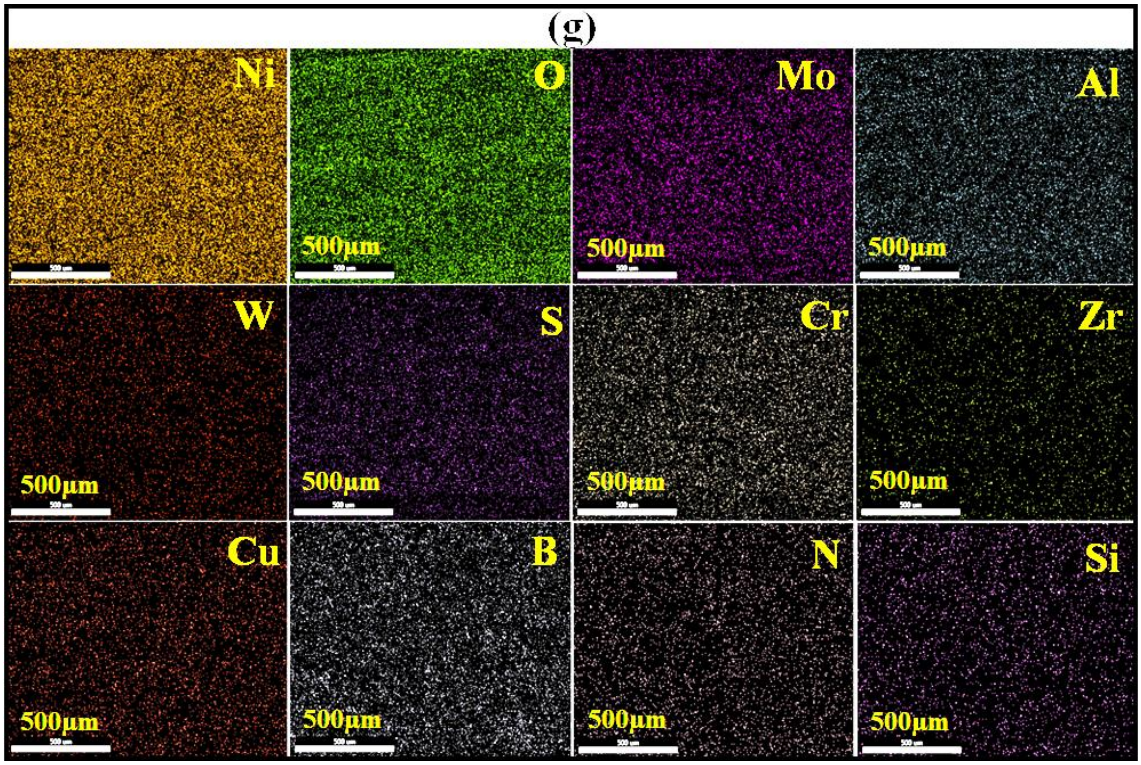

Fig. 5.36: FESEM images of the worn scar of NAWB composite at (a) room temperature, (b) 200 °C, (c) 400 °C, (d) 600 °C, (e) 800 °C, and (f and g) EDS and elemental maps of worn track at 600° C and 800 °C.

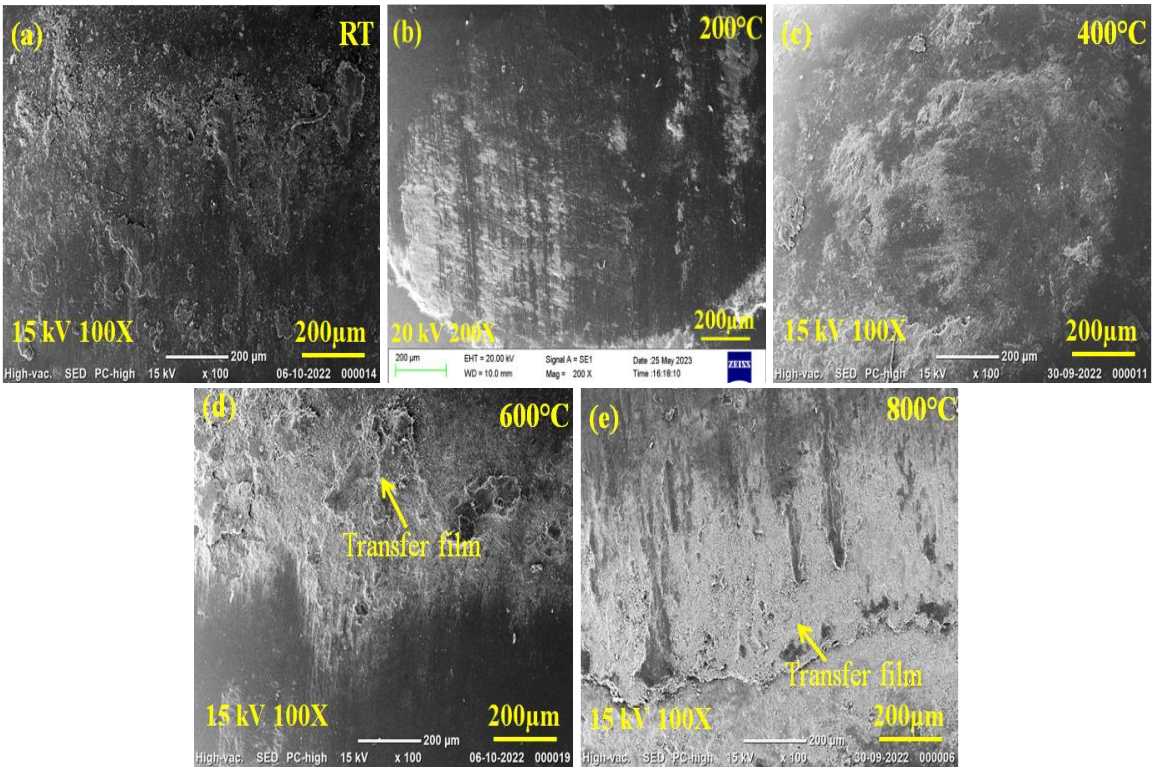

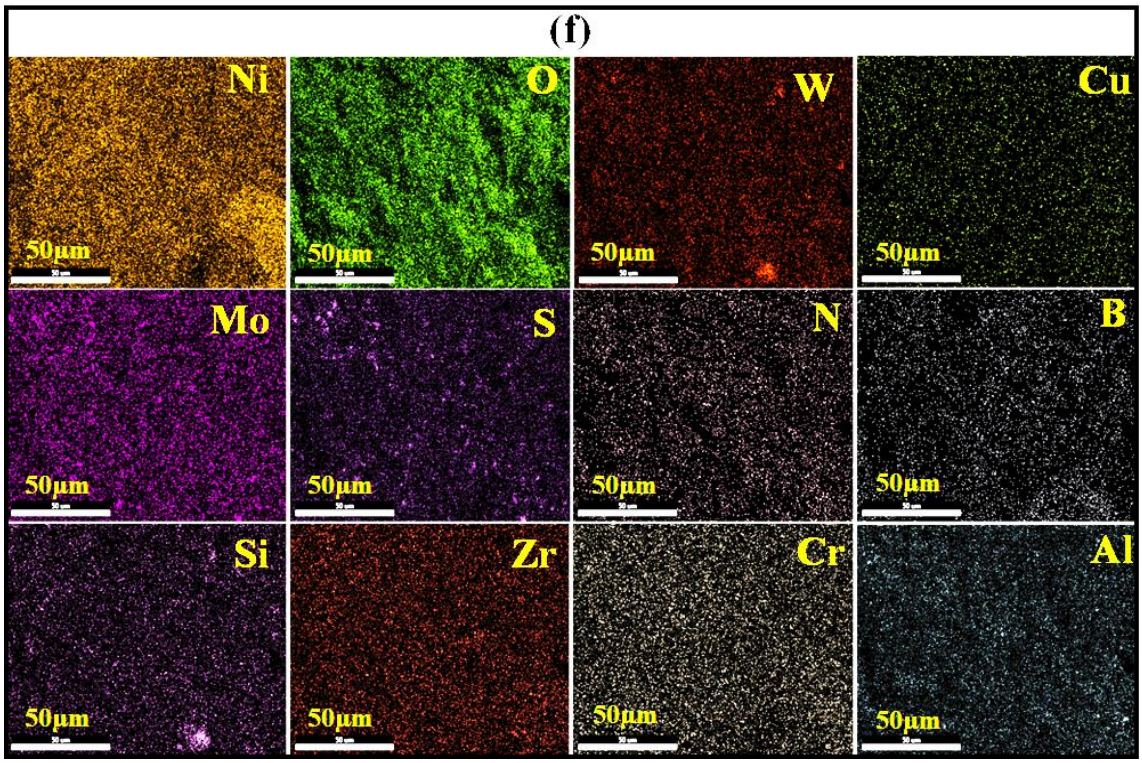

Fig. 5.37: FESEM images of the worn scar of Si3N4 ball at (a) room temperature, (b) 200 °C, (c) 400 °C, (d) 600 °C, (e) 800 °C, and (f) elemental maps of transfer film on worn Si3N4 ball (counterface) at 800 °C.

Figures 5.38(a-d) demonstrate the XRD pattern of the worn surfaces of NA, NAW, NAB, and NAWB composites at various temperatures. At RT, the XRD pattern of NA (Fig. 5.38a) indicates peaks corresponding to Ni_3Al (ICSD Ref. 03-065-0430), whereas at 200 °C, additional peaks pertaining to $NiMoO_4$ (ICSD Ref. 00-045-142) and MoO_3 (Ref. 00-021-0569) are present. Between 400 °C and 600 °C, NiO (Ref. 01-089-7130) appears along with $NiMoO_4$ and MoO_3. At 800 °C, only NiO and $NiMoO_4$ peaks are observed, and no peak corresponding to MoO_3 could be seen. The XRD spectrum depicted in Fig. 5.38(b) for the worn NAW composite indicates the existence of Ni_3Al and WS_2 (Ref. 01-084-1399) at both RT and 200 °C. Furthermore, at 200 °C, supplementary peaks of $NiMoO_4$ and MoO_3 are also detected. In addition to NiO and $NiMoO_4$, new diffraction peaks of WO_3 (Ref. 01-088-0550) were observed at 600 °C and 800 °C. Fig. 5.38(c) shows the XRD patterns of NAB, which reveal the existence of Ni_3Al and *h*BN (Ref. 01-078-0428) at RT and

additional peaks of $NiMoO_4$, CuO, and MoO_3 at 200 °C. New diffraction peaks of NiO along with MoO_3, CuO, *h*BN, and $NiMoO_4$ are observed at 400 °C and 600 °C, whereas at 800 °C, the detected peaks correspond to NiO, *h*BN, CuO, and $NiMoO_4$. The XRD pattern of the worn NAWB composite (Fig. 5.38d) has revealed peaks pertaining to Ni_3Al at RT and 200 °C, WS_2 peaks from RT to 400 °C, *h*BN, CuO, and $NiMoO_4$ peaks from RT to 800 °C, WO_3 peaks from 400 °C to 800 °C, and MoO_3 peaks from 200 °C to 600 °C. The presence of *h*BN, MoO_3, NiO, WO_3, CuO and $NiMoO_4$ over the worn surface of composites/coatings has been reported to provide effective lubrication at elevated temperatures [35,58,130,131,144,152].

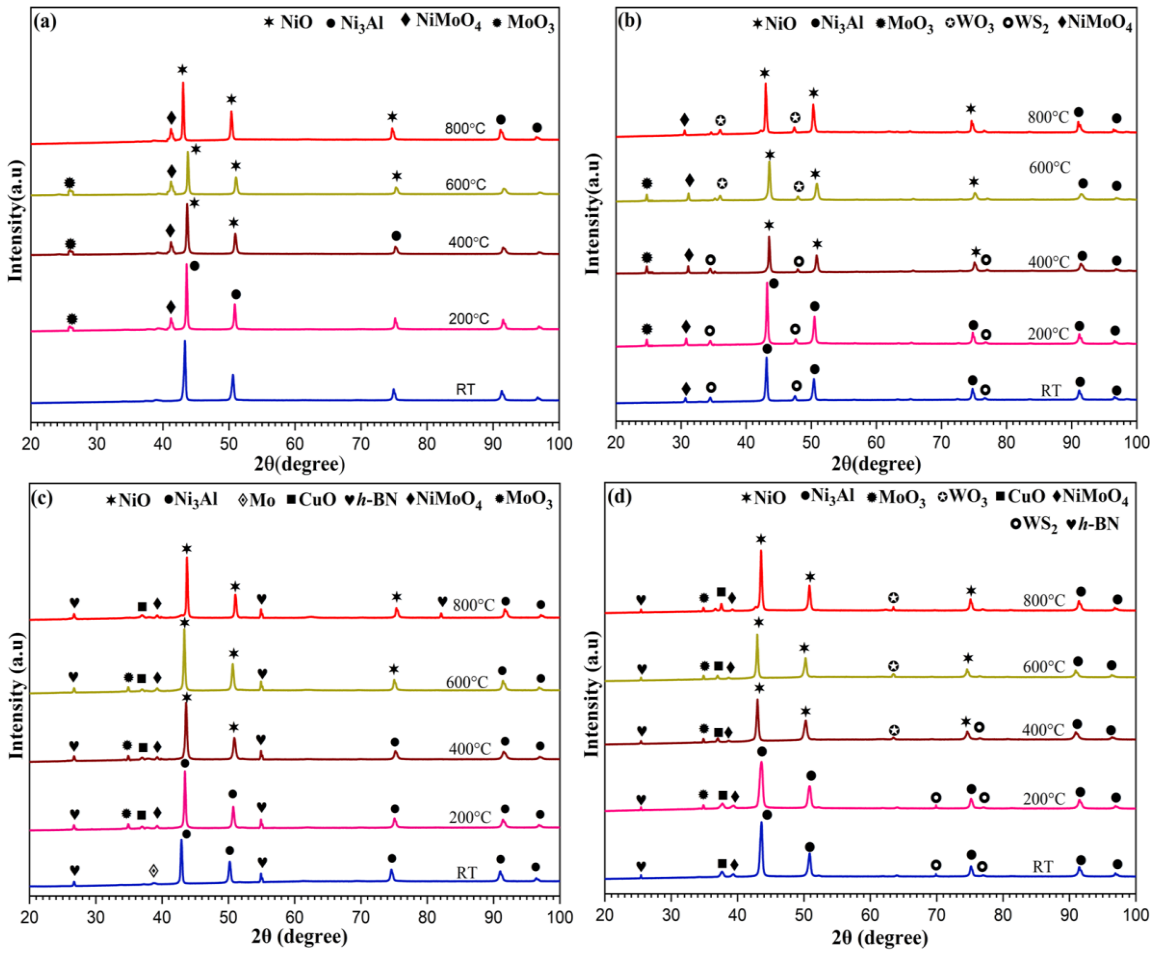

Fig. 5.38: XRD patterns of worn composite specimens (a) NA, (b) NAW, (c) NAB, and (d) NAWB at various temperatures.

Figure 5.39 shows the results of Raman spectroscopy performed on worn samples of NA, NAW, NAB, and NAWB composites to investigate the chemical composition of the worn track. The spectra of the worn track of NA (Fig. 5.39a) demonstrate the existence of $NiMoO_4$ in the temperature range of 200 °C to 800 °C, whereas additional peaks corresponding to NiO and MoO_3 could also be observed at 400 °C, 600 °C, and 800 °C. Raman spectra of the worn track of NAW composite (Fig. 5.39b) has shown the existence of peaks pertaining to WO_3, NiO, and MoO_3 from 400 °C to 800 °C, as well as $NiMoO_4$ peaks from 200 °C to 800 °C. The Raman spectra for worn NAB composite (Fig. 5.39c) has revealed the peaks associated with *h*BN from RT to 800 °C, and CuO and $NiMoO_4$ peaks from 200 °C to 800 °C, while NiO and MoO_3 peaks are observed at 400 °C, 600 °C, and 800 °C. The Raman spectra of the worn surface of NAWB composite (Fig. 5.39d) exhibit the peaks that correspond to *h*BN from RT to 800 °C, CuO and $NiMoO_4$ peaks from 200 °C to 800 °C, apart from WO_3, NiO, and MoO_3 peaks from 400 °C to 800 °C.

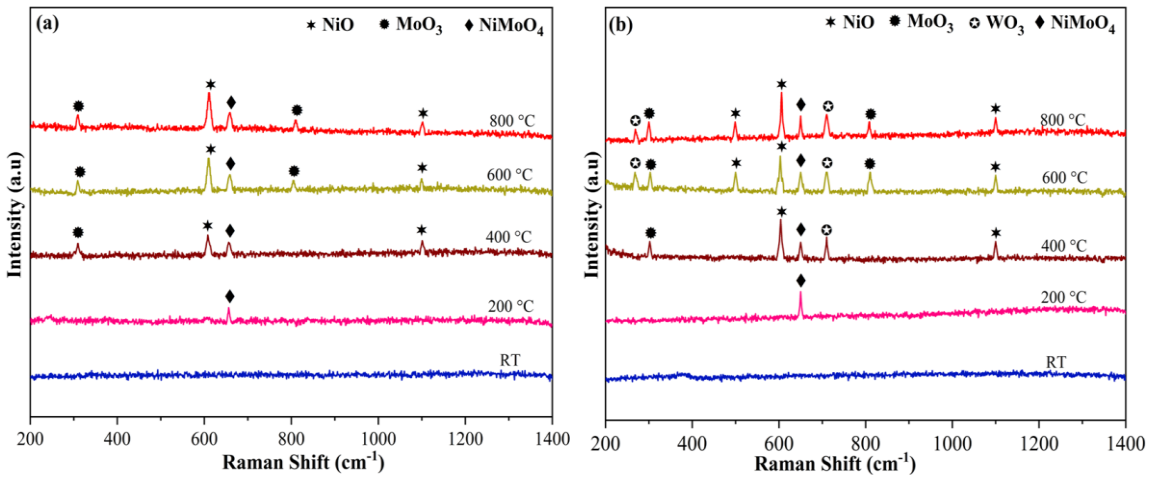

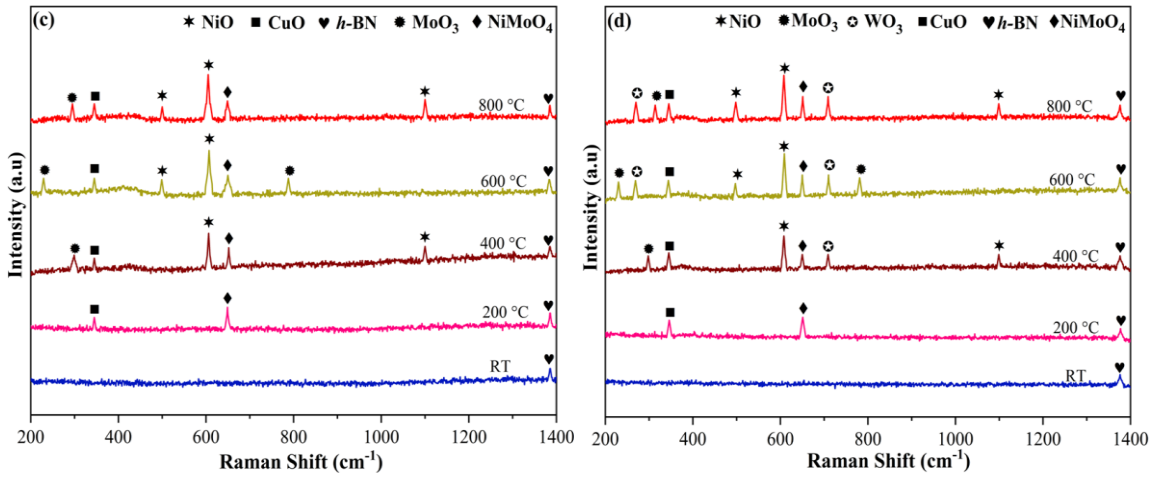

Fig. 5.39: Raman spectra of worn specimens of (a) NA, (b) NAW, (c) NAB, and (d) NAWB at various temperatures.

5.4 Discussions: Friction and Wear behaviour of Ni_3Al-WS_2/Ni_3Al-Cu-*h*BN/Ni_3Al-WS_2-Cu-*h*BN composites

The addition of Cu-*h*BN to the Ni_3Al intermetallic compound has resulted in a decrease in its hardness from 355 ± 5 HV to 335 ± 5 HV, primarily because of the inherent softness of Cu-*h*BN. Zhao et al. [58] have also reported a reduction in the Vickers micro-hardness of the Ni-based coating with the addition of *h*BN and nano-Cu encapsulated *h*BN**.** The incorporation of WS_2 and the combination of WS_2 and Cu-*h*BN into the Ni_3Al has led to an increase in the hardness from 355 ± 5 HV to 365 ± 6 HV and 358 ± 4 HV.

The initial fluctuations of the coefficient of friction (CoF) in NA, NAW, NAB and NAWB composites have been attributed to the initial surface roughness of the mating bodies. However, as the sliding progresses, the surfaces become smoother and attain better conformity with each other, leading to the stabilisation of CoF, as seen from Fig. 5.27. The NA and NAB composites exhibit more significant fluctuations than NAW and NAWB, which may be due to their relatively lower hardness, allowing the harder asperities of the Si_3N_4 ball to penetrate into the composite.

The observed friction and wear behaviour of NA, NAW, NAB and NAWB composites with temperature (Figs. 5.28 and 5.29) may be explained based on several factors: (i) the presence of wear particles, (ii) the nature of transfer layer (loosely bound or well compacted, continuous or patchy), (iii) the area coverage of transfer layer over the surface, and (iv) the presence of lubricious compounds or oxides on the worn surface of the composites as well as the counterface Si_3N_4 ball at different temperatures, apart from the hardness of the composite material. The loose wear particles are expected to cause abrasion and, consequently, a larger loss of material or formation of a transfer layer of wear debris over the worn surface of the composite as well as the counterface. The transfer layer may either be continuous, covering the larger area of the worn surface, which helps in protecting the underlying substrate from direct contact with the counterface, leading to a smaller loss of material, or patchy (discontinuous), allowing contact at some places with the counterface asperities, resulting in larger loss of material as well as friction. Simultaneously, the transfer layer may be well-compacted (debris particles are well adhered to each other), which effectively inhibits direct contact between mating bodies or loosely bound, which may cause abrasion. The hardness and wear rate have an inverse relationship, and it has been stated that the harder the material, the better its resistance to wear [25]. However, the friction and wear behaviour of the tribo-pair depends on the relative dominance of several dynamic processes: softening of the material, formation of new compounds and oxides, strain hardening (which may occur at room temperature and can cause an increase in hardness), or formation of a tribo-film during sliding. The hardness of the material decreases with increasing temperature due to softening; hence, the wear rate may increase. On the other hand, the wear rate may decrease due to the formation of a tribo-film containing the lubricous species, which offers easy shearing capability at the sliding

interface leading to a reduction in friction. However, the final outcome depends on the relative dominance of the different competitive phenomena taking place during sliding.

The worn surface of NA at RT (Fig. 5.30a), 200 °C (Fig. 5.30b) and 400 °C (Fig. 5.30c) exhibit ploughing, loose and dispersed wear debris, delamination and scattered transfer film, which may have contributed to a higher coefficient of friction (0.65 to 0.56) and wear rate (3.52 to 5.95 × 10^{-5} mm^3/Nm) as illustrated in Figs. 5.28 and 5.29, respectively. The decrease in the hardness of the composite with increasing temperature may also have contributed to the increased loss of material. It has been reported earlier that the softening of material results in an increased ductility and larger real area of contact, which increases surface adhesion and leads to an increase in wear rate [25,153]. However, the hardness of the composite specimen at elevated temperatures has not been measured in the current investigation. A decrease in coefficient of friction (0.56 to 0.42) and wear rate (5.95 to 2.46 × 10^{-4} mm^3/Nm) beyond 400 °C may be attributed to the existence of a dense, compact, and continuous tribo-film over the worn track of NA (Figs. 5.30d and f) and the opposing Si_3N_4 ball (Figs. 5.31d and e). This tribo-film contains NiO, $NiMoO_4$, and MoO_3, which are known to possess lubricating properties at extreme temperatures [55,144]. The EDS analysis (Fig. 5.30e) and elemental mapping (Fig. 5.30g) confirmed the presence of NiO, $NiMoO_4$, and MoO_3, while XRD (Fig. 5.38a) and Raman spectroscopy (Fig. 5.39a) validated their formation between 400 °C to 800 °C. The formation of tribo-film on the interface offers a barrier to the direct interaction between the mating bodies and provides a low-shearing interface, leading to a reduction in both friction and wear, as explained above. A decrease in CoF (0.42 to 0.34) observed for NAW (Fig. 5.28) from RT to 400 °C may be attributed to the presence of WS_2 over the worn surface (Fig. 5.38b), which provides a weak shearing interface at sliding contact due to its lamellar structure, as reported in another study [34]. The increase in wear rate from RT to 400 °C for NAW composite (Fig. 5.29)

may be attributed to the existence of loose wear debris and patchy transfer film at RT (Fig. 5.32a) and the delamination, wear marks and micro-cracks at 200 °C and 400 °C on the composite surface (Figs. 5.32b and c), along with a discontinuous transferred film and delamination over the worn scar of the counter Si_3N_4 ball (Figs. 5.33a to c), which might have given rise to direct contact between ball and composite resulting in larger material loss as stated earlier. However, the decrease in CoF and wear rate beyond 400 °C may be ascribed to the formation of a continuous and compact tribo-film containing the lubricous oxides, namely, MoO_3, NiO, WO_3 [34,35], and $NiMoO_4$ over the worn region of NAW composite (Figs. 5.32d and e) and counter Si_3N_4 ball (Figs. 5.33d and e), as evidenced by the EDS (Figs. 5.32(f and g) and 5.33(f)), XRD (Fig. 5.38b), and Raman spectra (Fig. 5.39b). At elevated temperatures, the oxidation of WS_2 occurs, leading to the formation of WO_3 through the chemical reaction: $WS_2 + 3/2O_2 \rightarrow WO_3 + 2S$ [154]. The presence of WO_3, NiO, MoO_3 and $NiMoO_4$ peaks from 400 °C to 800 °C detected in XRD (Fig. 5.38b) and Raman spectra (Fig. 5.39b) reflects the relative dominance of lubricating tribo-film over decreasing hardness in lowering both the CoF and wear rate. A relatively higher hardness value of NAW compared to NA and NAB may account for the relatively lower wear rate observed for NAW.

The presence of Cu-*h*BN (Figs. 5.38c and 5.39c) over the worn surface of the NAB composite may explain the decrease in CoF (from 0.48 to 0.38) observed for NAB (Fig. 5.28) from RT to 400 °C. At RT, 200 °C and 400 °C, the presence of wear particles, scattered transfer film, delamination and micro-cracks on the worn surface of NAB, along with the discontinuous transfer film on the worn scar of counter Si_3N_4 ball (Figs. 5.34a-c and 5.35a-c) points toward the occurrence of direct contact between materials, which might have led to marginal increase in the wear rate (2.285 to 3.1 x 10^{-5} mm^3/Nm) from RT to 400 °C compared to NA (Fig. 5.29). The decrease in both CoF (0.38 to 0.28) and wear rate (3.1 to

1.95 x 10^{-5} mm^3/Nm) at relatively higher temperatures (600 and 800 °C) may again be explained based on the presence of a smooth, compact, and continuous tribo-film comprising lubricious species like *h*BN, NiO, CuO, $NiMoO_4$ and MoO_3 on the worn surface of NAB composite (Figs. 5.34d and e) and counter Si_3N_4 ball (Fig. 5.35e), as revealed by the EDS-Elemental mapping (Figs. 5.34f, g and h and 5.35f), XRD (Fig. 5.38c), and Raman spectra (Fig. 5.39c). Between 400 °C to 800 °C, the XRD and Raman analysis revealed the peaks belonging to NiO, *h*BN, MoO_3, CuO, and $NiMoO_4$ on the worn surface of NAB. The relatively higher values of CoF and wear rate of NAB than NAW may be attributed to the lower hardness of NAB (335 ± 5 HV) in comparison to NAW (365 ± 6 HV), which results in a larger real area of contact, increased surface adhesion and wear rate.

A decrease in the coefficient of friction (0.48 to 0.35) of NAWB composite with an increase in temperature could potentially be ascribed to the existence of WS_2 and Cu-*h*BN over the worn track of NAWB composite at room temperature (RT) and 400 °C, as evidenced by XRD (Fig. 5.38d) and Raman spectra (Fig. 5.39d). Previous studies have reported that WS_2 can offer lubrication from RT to 450 °C [34]. The increase in wear rate (2.12 to 2.61 x 10^{-5} mm^3/Nm) from RT to 400 °C (Fig. 5.29) may be attributed to the presence of loose wear particles, delamination, ploughing, and scattered tribo-film on the worn region of NAWB composite (Figs. 5.36a-c), along with a discontinuous tribo-film on the worn scar of the counterpart Si_3N_4 ball (Figs. 5.37a-c), which may have allowed direct contact between the NAWB composite specimen and the opposing Si_3N_4 ball. However, at higher temperatures (i.e., 600 °C and 800 °C), the decrease in both CoF (0.35 to 0.18) and wear rate (2.61 to 0.87 x 10^{-5} mm^3/Nm) may be attributed to the formation of a compact and continuous glaze film along with a smooth tribo-film on the worn track of NAWB composite (Figs. 5.36d and e) and the opposing Si_3N_4 ball (Figs. 5.37d and e). These films contain peaks corresponding to *h*BN and lubricious oxides, such as NiO, MoO_3, CuO, WO_3, and $NiMoO_4$

between 400 °C to 800 °C, as evidenced by XRD and Raman spectra (Figs. 5.38d and 5.39d), which have been shown to perform exceptionally well at elevated temperatures. The presence of O, Ni, Mo, W, S, Cu, B, and N in EDS and elemental maps of the worn NAWB composite (Figs. 5.36f and g) and the Si_3N_4 counter ball (Fig. 5.37f) at 800 °C demonstrates the existence of *h*BN and the development of Ni, Mo, W, and Cu-based oxides which possess inherent lubricious properties. At elevated temperatures, the presence of *h*BN, a well-known solid lubricant with high-temperature capabilities, may have had a more substantial impact on lowering the friction coefficient than WS_2, which has been shown to be ineffective beyond 450 °C [34,35]. The formation of CuO has been reported to occur beyond 400 °C, and it has been shown to act as a high-temperature lubricant [58,73,144]. Therefore, at elevated temperatures (600 and 800 °C), CuO aids other lubricating oxides in effectively reducing the friction and improving the anti-wear properties of the NAB and NAWB composites. The presence of Cu-*h*BN and lubricious oxides of Ni, Mo, W, and Cu on the worn track of NAWB reflects the relative dominance of lubricating tribo-film over decreasing hardness in lowering both the CoF and wear rate beyond 400 °C compared to NAW. The relatively lower hardness value of NAWB compared to NAW and the inferior lubrication performance of *h*BN solid lubricant below 400 °C may account for the relatively higher wear rate and CoF observed for NAWB compared to NAW from RT to 400 °C. The present investigation reflects that combining solid lubricants (WS_2 and Cu-*h*BN) is a viable approach to achieve a reduced coefficient of friction and wear rate beyond 400 °C, as evident from Figs. 5.28 and 5.29.

Figure 5.40 illustrates the probable mechanisms of lubrication and material removal that occur through tribo-chemical reactions at the sliding interface for NA, NAW, NAB and NAWB composites. The worn surface of base Ni_3Al (NA) demonstrates the existence of wear particles, transferred patches, ploughing and delamination at RT to 400 °C, leading to

a relatively higher CoF and wear rate. However, at 600 °C and 800 °C, the presence of a tribo-film enriched with lubricious oxides of Ni and Mo on the worn tracks of NA and the counterface ball results in a decrease in friction and wear by eliminating the direct contact between the tribo-pair (Fig. 5.40a). The existence of a WS_2-rich tribo-film in NAW (Fig. 5.40b) provides adequate lubrication, which results in a decrease in CoF compared to NA from RT to 400 °C. However, wear particles, delamination, micro-cracks and scattered transfer film lead to an increased wear rate. At 600 and 800 °C, the formation of a tribo-film having lubricious oxides of W, Ni and Mo over the contacting interface of NAW composite and counter ball, as depicted in Fig. 5.40(b), results in improved tribological performance. As far as NAB is concerned, the presence of *h*BN, apart from other lubricating species on the worn surfaces of the contacting materials, leads to a continuous reduction of CoF from RT to 800 °C due to its lamellar structure (Fig. 5.40c). An increase in wear rate from RT to 400 °C is a result of the features present on the worn surface of the composite and counterface ball as explained earlier, while a reduction in wear beyond 400 °C is due to the *h*BN and formation of lubricious oxides such as NiO, $NiMoO_4$, CuO and MoO_3, which provide effective lubrication and prevent wear. The NAWB composite experiences a reduction in CoF from RT to 400 °C owing to the formation of a tribo-film enriched with WS_2-Cu-*h*BN, while the existence of loose and dispersed wear debris, delamination, ploughing and a discontinuous tribo-film contribute to an increased wear rate (Fig. 5.40d). However, at 600 and 800 °C, the formation of a compact-continuous tribo-film and smooth glaze layer enriched with lubricating agents like *h*BN, NiO, MoO_3, CuO, WO_3 and $NiMoO_4$ over the worn surface of NAWB composite and Si_3N_4 ball effectively reduces both friction and wear in NAWB composite. These findings suggest a cooperative synergy between WS_2 and Cu-*h*BN in effectively reducing friction and wear at temperatures beyond 400 °C.

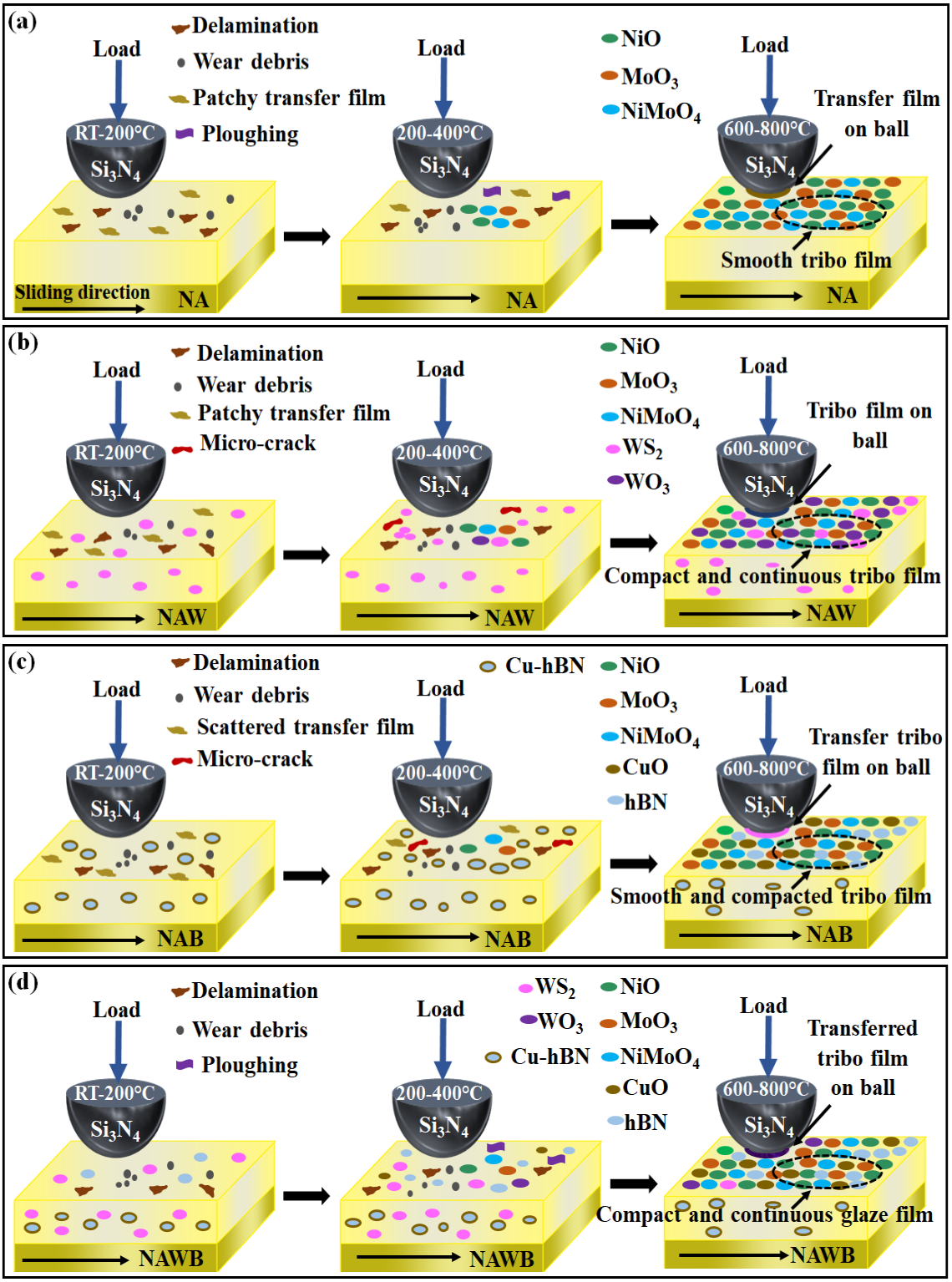

Fig. 5.40: Schematic illustration of lubrication and material removal from RT-200 °C, 200 °C-400 °C, and 600 °C -800 °C for (a) NA, (b) NAW, (c) NAB and (d) NAWB.

To summarise, the base Ni_3Al has shown the highest coefficient of friction and wear rate at all the test temperatures, followed by Ni_3Al-Cu-*h*BN, Ni_3Al-WS_2, Ni_3Al-WS_2-Cu-*h*BN and

(depending on the temperature). Ni_3Al-WS_2 has shown the lowest CoF and wear rate compared to Ni_3Al-WS_2-Cu-*h*BN from RT to 400 °C, which has been attributed to the higher hardness of Ni_3Al-WS_2 in comparison to Ni_3Al-WS_2-Cu-*h*BN as well as inferior lubrication performance of *h*BN in Ni_3Al-WS_2-Cu-*h*BN below 400 °C. However, beyond 400 °C, Ni_3Al-WS_2-Cu-*h*BN has shown the lowest CoF and wear rate compared to Ni_3Al-WS_2 due to the formation of a compact glaze film containing Cu-*h*BN and lubricious oxides of Ni, Mo, W and Cu. The observed performance reflects the importance of a synergistic effect between a combination of solid lubricants in diminishing both friction and wear, which overcomes the limitations of utilising a sole lubricant at a similar hardness level as Ni_3Al. The incorporation of WS_2 and Cu-doped *h*BN, either individually or in conjunction, is beneficial in improving the friction and wear performance of Ni_3Al. However, the effect of WS_2 appears to be more prominent than Cu-*h*BN when added individually under the conditions of the present study (load, speed and temperatures). The combination of WS_2 and Cu-*h*BN seems more advantageous in improving the tribological performance at relatively higher temperatures than at low temperatures (< 400 °C).

5.5 Summary of friction and wear behaviour of Ni_3Al/-Ag/-WS_2/-Cu-*h*BN/Ag-WS_2/Ag-Cu-*h*BN/WS_2-Cu-*h*BN composites

Figure 5.41 (a and b) depicts the comparative performance of Ni_3Al and composites in terms of the variation of average CoF and wear rate with temperature. One may observe that Ni_3Al has exhibited the highest coefficient of friction and wear rate, except for 200 °C and 400 °C, where Ni_3Al-10Ag has shown the highest wear rate, which has been attributed to the higher hardness of Ni_3Al in comparison to Ni_3Al-10Ag (Fig. 5.41). Composites containing a single solid lubricant, namely Ni_3Al-10Ag and Ni_3Al-10Cu-*h*BN, demonstrated slightly higher CoF and wear rate from RT to 800°C compared to Ni_3Al-

$10WS_2$ composite and composites containing combination of solid lubricants i.e., Ni_3Al-Ag-WS_2, Ni_3Al-Ag-Cu-*h*BN and Ni_3Al-WS_2-Cu-*h*BN.

Ni_3Al-$10WS_2$ composite exhibited the lowest CoF and wear rate compared to Ni_3Al-$5WS_2$-5Cu-*h*BN from RT to 400 °C, which has been attributed to the higher hardness of Ni_3Al-$10WS_2$ in comparison to Ni_3Al-$5WS_2$-5Cu-*h*BN. Beyond 400 °C, Ni_3Al-$5WS_2$-5Cu-*h*BN has shown the lowest CoF and wear rate compared to Ni_3Al-$10WS_2$ due to the dominance of compact and continuous glaze film containing Cu-*h*BN and lubricious oxides of Ni, Mo, W and Cu over decreasing hardness.

All the composites containing a combination of solid lubricants, namely Ni_3Al-5Ag-$5WS_2$, Ni_3Al-5Ag-5Cu-*h*BN and Ni_3Al-$5WS_2$-5Cu-*h*BN, have demonstrated a better friction and wear performance compared to the composites containing a single solid lubricant (Ag, WS_2 and Cu-*h*BN) and Ni_3Al at elevated temperatures. The occurrence of a synergistic action between the combination of solid lubricants, namely, Ag-WS_2, Ag-Cu-*h*BN and WS_2-Cu-*h*BN from RT to 800 °C and the formation of lubricious oxides (NiO, MoO_3, $NiMoO_4$, WO_3, Ag_2MoO_4 and $Ag_2Mo_2O_7$ in Ni_3Al-Ag-WS_2; NiO, MoO_3, $NiMoO_4$, CuO, Ag_2MoO_4 and $Ag_2Mo_2O_7$ in N_3Al-Ag-Cu-*h*BN; NiO, MoO_3, $NiMoO_4$, WO_3 and CuO in N_3Al-WS_2-Cu-*h*BN) due to tribo-chemical reactions, over the worn surfaces of composite and counterface at elevated temperatures (beyond 400 °C) have been found to play an instrumental role in reducing both the friction and wear from RT to 800 °C by overcoming the handicaps of employing a single solid lubricant at a comparable level of hardness of the base intermetallic compound. The tribological performance of these composites, in terms of the average coefficient of friction and the wear rate, has been observed to fall within the same range under the conditions of load, speed, and temperatures used in the presented study. However, Ni_3Al-5Ag-$5WS_2$ composite has been found to

perform slightly better than Ni_3Al-5WS_2-5Cu-*h*BN, followed by Ni_3Al-5Ag-5Cu-*h*BN composite.

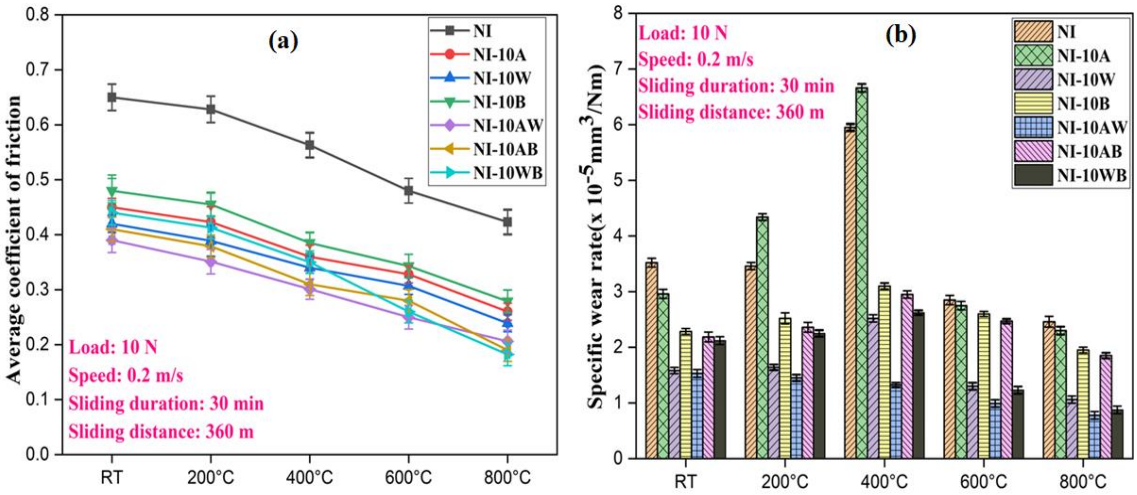

Fig. 5.41: Variation of (a) average coefficient of friction and (b) specific wear rate with temperature for Ni_3Al and its composites, i.e., Ni_3Al-10Ag (NI-10A), Ni_3Al-10WS_2 (NI-10W), Ni_3Al-10Cu-*h*BN (NI-10B), Ni_3Al-5Ag-5WS_2 (NI-10AW), Ni_3Al-5Ag-5Cu-*h*BN (NI-10AB) and Ni_3Al-5WS_2-5Cu-*h*BN (NI-10WB).